University of Veterinary Medicine
Doctoral School of Veterinary Science

Multimodal visualisation of the canine brain based on structural imaging, cryosectioning and 3-dimensional modelling

PhD thesis

Dr. Kálmán Czeibert

2020

Supervisors:

……..

Dr. Bence Rácz, Ph.D.
associate professor
University of Veterinary Medicine,
Department of Anatomy and Histology
supervisor

……..

Dr. Örs Petneházy, Ph.D.
honorary associate professor
University of Kaposvár
supervisor

Copy … of 8

……..

Dr. Kálmán Czeibert

Table of contents

Abbreviations

2D	two-dimensional
3D	three-dimensional
3R	replacement, reduction, refinement
3T	three Tesla
AF-S VR	auto focus with silent wave motor, vibration reduction
CBTB	Canine Brain and Tissue Bank
CCD	canine cognitive dysfunction
CNC	computer numerical control
CORE	computer-reconstructed
CR2	Canon raw version 2 image file
CT	computed tomography
DICOM	digital imaging and communications in medicine
DPI	dots per inch
DSLR	digital single lens reflex
DTI	diffusion tensor imaging
DWI	diffusion weighted imaging
EF	electro-focus
EOS	electro-optical system
FDP	Family Dog Project
fMRI	functional magnetic resonance imaging
FOV	field of view
IF-ED	internal focus extra-low dispersion
IT	information technology
JPEG	joint photographic experts group format
LSFM	light sheet fluorescence microscopy
LUT	lookup table
MATLAB	matrix laboratory

MNI	Montreal Neurological Institute
MPR	millimetres per revolution
MR	magnetic resonance
MRI	magnetic resonance imaging
NAV	Nomina Anatomica Veterinaria
NIfTI	neuroimaging informatics technology initiative
OCT	optical coherence tomography
PDF	portable document format
PET	positron emission tomography
RGB	red, green, blue
RNA	ribonucleic acid
ROI	region of interest
RPM	revolutions per minute
SFDP	Senior Family Dog Project
SLS	selective laser sintering
SNR	signal-to-noise ratio
SPECT	single-photon emission computed tomography
SPM	statistical parametric mapping
STL	stereolithography
TE	echo time
TIFF	tag image file format
TIM	total imaging matrix
TR	repetition time
USM	ultrasonic motor

1. Summary

„Like Argus of the Ancient Times...”
/Jack London/

The central nervous system can be studied with different methods and in various ways. In an initiative to demonstrate the cross-section anatomy of the body, researchers have developed a method in which tissue is not sliced but is milled stepwise from a block. This technique is referred to as cryosectioning or cryomacrotomisation. The advantage of this procedure is that depending on the milling and photographic equipment, one can record cross-sectional macro-anatomical images with especially high-resolution and colour fidelity, regardless of the tissue hardness (which should have been controlled with a prior decalcination procedure in a histological study). The data provided by this technique can be used with special software to interactively visualise the cryosectioned tissue block. To date, there is no detailed cross-sectional anatomical map for the canine brain showing the macroscopically visible structures *in situ* (i.e., surrounded by the neurocranium and the neighbouring soft tissues), together with a comparable structural imaging dataset with a small slice thickness and possibility for interactive multimodal visualisation. Our aim was to create high-quality macro-anatomical cross-sectional images and 3-dimensional (3D) models of a canine brain that could be paired with the results of magnetic resonance imaging (MRI) and computed tomography (CT) techniques from the same specimen.

Here, we performed various studies to investigate how to achieve the best possible results for both the cryomacrotomisation procedure and the 3D visualisation. We undertook several pilot studies to identify the optimal cryosectioning system and settings that provided images which could then be post-processed with various visualisation software packages. These trial sectioning and milling studies comprised: (a) different specimens (dogs, cats, pig); (b) various cutting and milling machines (conventional and computer numerical controlled ones); (c) individually designed embedding boxes; (d) improved cooling and thermoregulation methods; and (e) improved surface care and photographic capturing methods. In parallel with the cryomacrotomisation studies, we also tested various software packages to find the best for handling large datasets (from both medical imaging techniques and from digital photography). We also performed segmentations, 3D modelling and multimodal visualisation and investigated how to create printable models from our digital objects. As part of these visualisation studies, we created digital and 3D-printed models of the major osseous and arterial structures of a canine head, made a comparable virtual model of an equine petrosal bone to show the complex architecture of the middle and inner ear, produced multimodal images and a flip-book of a cat head, and designed a canine MRI brain label map comprising 86 cortical and subcortical structures to serve as an aid in the medical imaging analysis.

The final study was carried out on a beagle dog (considering the previous studies, the scientific literature, and the ethical and research recommendations). The specimen was first scanned with MRI and CT both antemortem and postmortem to provide a comparable structural imaging background for the anatomical study. Subsequently, a head block was made that was embedded into a custom-made thermoregulated plexiglass box and was frozen and maintained at -80°C. The cryosectioning was performed with a computer numerical controlled (CNC) milling system. We recorded 1112 images from the head block with high-resolution photography, with a layer thickness of only 100 µm. Despite the fact that we did not use any tissue staining to preserve the original colour of the brain, the images proved to be so detailed that the major subcortical nuclei could be distinguished in the photographs. In the next phase, all the data volumes from the structural images and from the cryomacrotomisation were imported into Thermo Scientific Amira for Life Sciences 6.0 and the 3D Slicer software. Using these programs, the image volumes were co-registered (so they could be aligned in the same global coordinate system), and 3D models were made of the different structures (e.g., brain, arteries, veins, endocranial cast, skull).

As a result, we were able to visualise the different two-dimensional (2D) and 3D images and models together, reconstructed the coloured anatomical image volume in the other orthogonal planes without loss of detail, and created an interactive portable 3D document and a 3D-printed model of the endocranial cast. The beagle dataset was also co-registered to the MRI label map that we created for neuroimaging analysis in the framework of our visualisation studies. Comparing the results of our final study with the scientific literature and similar works related to dogs, we could conclude that, to date, this macro-anatomical study of the *in situ* canine brain has the highest level of detail and imaging quality. This work is therefore useful by providing a neuroanatomical guide for future educational, medical and research purposes. The neuroanatomical studies conducted during this thesis also provided additional practical benefits, such as supporting awake, functional MRI experiments on dogs, identifying the main canine resting-state network systems, providing an anatomical base for MR analysis with a brain label map, and creating a canine brain and tissue bank. Neuroanatomical comprehension and 3D visualisation had been also advantageous in the area of veterinary medicine for planning and performing small animal intracranial neurosurgical interventions.

2. Introduction and aims of the study

There are several ways to visualise macro-anatomical structures, such as conventional preparations and sections can be made shortly postmortem on a fresh cadaver, or they can be previously fixed with a fixative agent (Brenner, 2014), macerated bones can be created (King & Birch, 2015; Offele et al., 2007; Simonsen et al., 2011); alternatively, objects can be made by corrosion casting (Hirschberg et al., 1999; Krucker et al., 2006; Verli et al., 2007). The result of the tissue preparation can be captured in photographs or videos, or these procedures can be combined with the different imaging methods so that the selected region or specimen can be digitised for 2D and 3D analysis. These techniques are all suitable methods to visualise the different systems of the body, and they can be grouped as direct or indirect methods and as tissue maintaining or tissue destroying methods. Direct imaging means that the original tissue can be seen either in its true colour (e.g., with endoscopy) or stained histologically (Dettmeyer, 2011). Indirect imaging techniques, such as computed tomography (CT), magnetic resonance imaging (MRI), positron emission tomography (PET) and single-photon emission computed tomography (SPECT) provide a computer-generated picture (most commonly a greyscale image), and during post-processing an artificial colour is added for the easier differentiation based on tissue properties. Examples include X-ray attenuation (CT) or using the natural magnetic properties of the body (MRI) (Sandhu et al., 2010). Indirect imaging methods are tissue maintainers, but they have some limitations in showing the structures (mostly due to limited spatial resolution or similarities in signal intensity from the adjacent anatomical structures). The central nervous system is enclosed in a bony capsule, and in the case of larger animals and humans the brain cannot be routinely sectioned together with the skull due to the hardness of the bone, although the present methods make it possible to produce histological sections that are as large as a human brain (Amunts et al., 2013; Ratiu & Talos, 2006). Plastination of the slices is a good method for tissue preservation, and selective staining is possible (Riederer, 2014; Vibulchan & Cheunsuang, 2014), but the specimen's colour is partly altered during the procedure. Furthermore, tissue loss is expected due to the cutting and shrinkage (Elnady, 2016; von Hagens et al., 1987; Sora et al., 2019; Weiglein, 1997). Although there are works that have focused on imaging the canine central nervous system (e.g., Adrianov & Mering, 2010; Palazzi, 2011; Schmidt & Kramer, 2015; Singer, 1962), at this time there is no atlas for dogs that fulfils all of these criteria: (a) presenting the brain in a macro-anatomical aspect without removing it from the skull; (b) a slice interval small enough to see all the important macroscopic structures; and (c) all the orthogonal planes can be reconstructed using the data from the same animal. The last criterion is important, as most of the previous studies had to use several specimens to produce the differently oriented sections to compare them with the result obtained from the structural imaging techniques.

The primary aim of this research was to produce:

- high resolution,
- thin-layered,
- true-coloured,
- macro-anatomical image series from a canine brain,
- with cryosectioning the brain *in situ* in the skull,
- without the need for any previous fixation or decalcination procedure, which would interact with the colour or the composition of the different tissues,
- with the shortest postmortem time possible until freezing and embedding,
- performing both MRI and CT examinations with different imaging sequences,
- generating a software-based volume from the cryosectioned images, to be able to create multiplanar orthogonal view reconstructions,
- where the cryosectioned image volume can be registered in a common coordinate space with the scanning results from the structural imaging techniques,
- using 3D computer graphics software packages to create digital models,
- where based on the co-registered image volumes and the surface models annotated comparative illustrations from the brain can be made.

To achieve these objectives, we had to conduct several pilot experiments before the final study could took place, to clarify these crucial elements:

- What is the optimal **machine** system for the cryosectioning?
  - As this procedure is not commonly used, and to date only a few researchers have worked with it, we had to create our own cryomacrotomisation system.

- How can a consistent **temperature** for the tissue block be maintained?
  - Cryosectioning must be performed at relatively low temperatures to effectively harden all the various tissues and prevent lytic processes.

- What are the proper **photographic** parameters and settings?
  - The images must be recorded with their original colour and in high detail, while avoiding surface gleaming and reflections due to the humid environment.

- What **software** should be used for volume generation, co-registration of the different imaging modalities and creating 3D models?
  - We also expected to have a large amount (multi-gigabytes) of data, and the software had to be capable of performing various image processing actions.

3. Review of the related literature

If one wants to study the brain *in situ*, then different imaging methods or sectioning techniques of the entire head are available. Diagnostic imaging techniques create post-processed indirect greyscale images, and the quality of CT and magnetic resonance (MR) imaging depends on the applied imaging sequence, spatial resolution, signal-to-noise ratio (SNR) and various artefacts (Erdogmus et al., 2004; Goerner & Clarke, 2011; Roe, 2010; Thrall, 2012). There are two main possibilities to create true-colour macro-anatomical sections of the entire head: slicing the object into layers with a saw/macrotome blade, or mill the adjusted volume stepwise and photograph the resulting surfaces with a camera. In the first case, the slices could be handled individually, and their average thickness could vary from centimetres to millimetres. These slices can be preserved through fixation, staining and/or plastination. In contrast, milling removes a layer from the volume's surface (being tissue destructive method), and consecutive photographs record the revealed polished surface. In this procedure, the layer thickness depends only on the applied milling technique and its precision, ranging from millimetres to micrometres. This method is called cryosectioning, or cryomacrotomisation (Park et al., 2014, 2005; Spitzer et al., 1996). Although the layers are milled and not sliced, we used the existing terms to refer to this technique. There have been human studies in the cryosectioning field (Bergström et al., 1983; Lufkin et al., 1987; Rauschning, 1983), and an initiative by the National Library of Medicine in 1996, the Visible Human Project (carried out in association with the University of Colorado Center for Human Simulation), used cryomacrotomisation to visualise an entire male human body (Spitzer et al., 1996). In recent decades, similar projects have been carried out in China (Chinese Visible Human, Virtual Chinese Human Project) (Tang et al., 2010; Zhang et al., 2003), in South Korea (Visible Korean Human) (Park, 2017; Park et al., 2005), and by others who also used this technique (Ratiu & Talos, 2006).

Cryosectioning demonstrates the macro-anatomical composition of the body, but it can only be used efficiently if the micro-anatomical background is connected to it (e.g., with histological atlases). Techniques at the microscopic and ultrastructural level are far more outnumber the ones with macro-anatomical approach. An overview is given below regarding integrative projects that have developed detailed brain maps at the cellular level, and thus complete the macro-anatomical atlases, because with time possibly these methods could also be used to study the canine brain. Several projects have studied the central nervous system through detailed micro-anatomical reconstructions and computer simulations. The main projects are: (a) the Blue Brain Project, which aimed to build biologically detailed reconstructions and simulations of rodent and human brain circuits at the molecular level using supercomputers (https://bluebrain.epfl.ch); (b) the Human Brain Project, aiming to build a European research

infrastructure to help advance knowledge in neuroscience, medicine and computing in partnership with the Blue Brain Project (https://www.humanbrainproject.eu); (c) the Human Connectome Project, whose main goal is to construct a network map (a connectome) of the complete structural and functional neural connections *in vivo* within and across individuals (http://www.humanconnectomeproject.org); (d) the Spiking Neural Network Architecture (SpiNNaker), a supercomputer-based tool for the effective simulation of the brain (http://apt.cs.manchester.ac.uk/projects/SpiNNaker); (e) the BRAIN Initiative, which was launched in order to broaden the understanding of the human mind and the function of the brain, with an emphasis on preventing and treating disorders of the brain (http://www.braininitiative.org); (f) the Brain/MINDS project, to create maps for human and non-primate brains (https://brainminds.jp/en); and (g) the China Brain Project, which conducts research to improve diagnoses and promote successful disease treatments (Poo et al., 2016). Some of these initiatives have created structural brain maps with extremely high resolution, e.g., the BigBrain project produced a 3D reconstruction of the human brain from 7404 histological sections that had a 20 µm slice thickness, thus enabling the visibility of cells (Amunts et al., 2013). This atlas also comprised the MRI dataset of the same brain. A project from the Allen Institute for Brain Science created a publicly available multimodal gene expression atlas (Ding et al., 2016; Shen et al., 2012). The authors presented images from MRI and diffusion weighted imaging (DWI) together with 1356 high-resolution (1 µm per pixel) histological sections, marking 862 individual structures. Recent technologies, such as optical coherence tomography (OCT) or light sheet fluorescence microscopy (LSFM), are capable of showing biological tissues without destroying them. Tissue maps produced by these technologies serve as good diagnostic tools; for example, OCT is used in ophthalmology (Adhi & Duker, 2013), cardiology (Kaivosoja et al., 2018) and brain research (Damestani et al., 2013), whilst LSFM visualises tissues with subcellular resolution (Santi, 2011).

Cryomacrotomisation of smaller animals, such as mice and rats, has also been performed (Dogdas et al., 2007; Roy et al., 2009; Toga et al., 1995). To date, there are only a few studies that have used the cryomacrotomisation technique on larger animals. The cryosectioning of an entire dog was first performed in 1999 (Böttcher et al., 1999; Böttcher & Maierl, 1999). A study of the whole body of a one-year-old female beagle was conducted in 2014 (Park et al., 2014), a one-year-old domestic shorthair cat was investigated in 2018 (Chung et al., 2018), and a study of a Rhesus monkey (Chung et al., 2019) was recently published. The main results derived from these studies are compared with our achievements in detail later in the discussion chapter (6.1. Assessment and comparison). While in these researches whole cadavers were cryosectioned, we prioritised the proper visualisation of the *in situ* canine brain. To attain this objective, we developed our own workflow to create and post-process images.

4. Materials and methods

4.1. Conducting pilot studies in cryosectioning

To find the optimal settings which are suitable to perform the final dog brain study, we carried out five pilot cryosectioning experiments. In the course of these pilot tests we identified the main challenges that arose during the procedure. To accomplish, we had to further specify our initial questions, and we had to define the key features of the cryomacrotomisation procedure:

- Is there a need for postmortem perfusion?
- What is the proper embedding agent?
- What kind of tissue embedding box should be constructed?
- Which type of milling machine is ideal for the cryosectioning?
- How to provide correct thermoregulation during the procedure?
- What are the appropriate settings for the image recording?

Based on these, we continuously upgraded the experimental settings from study to study. Cadavers for the pilot experiments were obtained from owners who donated the body of their deceased animals to us in accordance with the Hungarian law (thus no special institutional ethical permission was required). As we wanted to optimize the technical parameters in the beginning, the species did not matter, and this was also the reason why we sectioned only a part of the neurocranial blocks in certain pilot studies. The anatomical terms used in this thesis comply with those in recent anatomy textbooks (Constantinescu & Schaller, 2011; Evans & de Lahunta, 2012; Nickel et al., 2003) and the latest (6th, released in 2017) version of the official Nomina Anatomica Veterinaria (NAV, http://www.wava-amav.org/wava-documents.html).

4.1.1. Study I: Cryosectioning a complete pig cadaver

We started our cryosectioning experiments with a full-body sectioning performed with an electric band saw (Biodur Products, Heidelberg, Germany), to observe the major differences and limitations that distinguish the layer-sectioning from the milling method, and to test the embedding and the photographic settings. A cadaver of a domestic pig (*Sus scrofa domestica*) was placed in a self-constructed wooden box container, and polyurethane foam (Foam-It 5; Smooth-On Inc., Macungie, Pennsylvania, USA) was used to fill the space around the body. After the embedding, the block was frozen to -80°C and stored for one week before sectioning.

During the sectioning procedure, the block was placed on a table where the cut surface was in contact with a continuously dry-ice-cooled (-78.5°C) plate. The thickness was set to be 7 mm by adjusting the distance of the cooling plate behind the saw. Rotational speed of the band saw was 40 m/sec, band width was 25 mm, and teeth density was one per every 15 millimetres. Following each section, the surrounding polyurethane foam was removed from the body, the surface was cleaned with acetone, and finally it was put on a glass plate for photographing (**Figure 1**). We used a Nikon D800 digital single lens reflex (DSLR) camera and an auto focus with silent wave motor, vibration reduction (AF-S VR) Micro-Nikkor 105 mm f/2.8G internal focus extra-low dispersion (IF-ED) lens with polarised filters (ISO-100, focus distance 60 mm, exposure time 1/200 sec, max aperture 3.4, F-stop f/8). The photos were recorded in 24-bit colour depth and 300 dots per inch (DPI) raw images; the dimension of each picture was 7360×4912 pixels. A total of 166 images were recorded from the full body.

Figure 1. Sectioning a pig with a band saw. A) The block during the sectioning procedure. B) Cleaning the surface with acetone. C) Mounting the section for photography.

4.1.2. Study II: Cryosectioning the head block of a dog

The second cryosectioning was performed with a JAFO FWD-32U universal milling machine (JAFO Jarocin Machine Tool Factory, Jarocin, Poland) (**Figure 2**). The system was tested with a neurocranial block obtained from an adult mongrel dog (*Canis familiaris*) cadaver. Red flexible polyurethane rubber (VytaFlex-10, Smooth-On Inc., Macungie, Pennsylvania, USA) was injected postmortem into the head through the bilateral common carotid arteries, and then the body was frozen at -30°C. One week later, a block was made from the head using an electric band saw by defining the boundaries of the block rostrally at the level of the infraorbital foramen and caudally at the level of the first cervical vertebra. The block was cooled to -80°C in a deep freezer, and after 7 days it was placed into a wooden box, which was filled with polyurethane foam (Foam-It 10; Smooth-On Inc., Macungie, Pennsylvania, USA) around the block. After the foam had hardened, the box was kept at -80°C.

Figure 2. Cryomacrotomisation of a dog head block. A) The JAFO universal milling machine with the fixed wooden box. B) The rolling mill and the side-cooled embedding box.

During the milling procedure the box was kept cool by placing dry ice against the block-holder on one side and also by drilling holes into the polyurethane foam around the head block where water and liquid nitrogen were poured regularly. The cut surface was frozen with dry ice pellets following the removal of a layer and capturing the subsequent surface. The plain milling cutter was rotated around the y-axis, and after each milling step the block had to be moved along the x-axis to the end of the table in order to photograph the surface (rotational speed = 400 revolutions per minute (RPM), cutter diameter = 120 mm, feed rate = 320 millimetres per revolution (MPR)). Debris was continuously removed during the milling with a vacuum cleaner. For the image recording we used a Canon electro-optical system (EOS) 7D DSLR camera and a Canon electro-focus (EF) 100 mm f/2.8 macro ultrasonic motor (USM) lens with polarised filters (ISO-100, focus distance 100 mm, exposure time 1/125 sec, max aperture 3.0, F-stop f/13, with X-Rite ColorChecker passport and polarising filters). Photos were recorded in 24-bit colour depth and 240 DPI raw images. The dimension of each picture was 5184×3456 pixels, and we confirmed the quality of each image on a computer right after they were captured (**Figure 3**). We recorded 238 images, from the level of the infraorbital foramen to the protuberantia occipitalis externa, with a slice thickness of 500 μm.

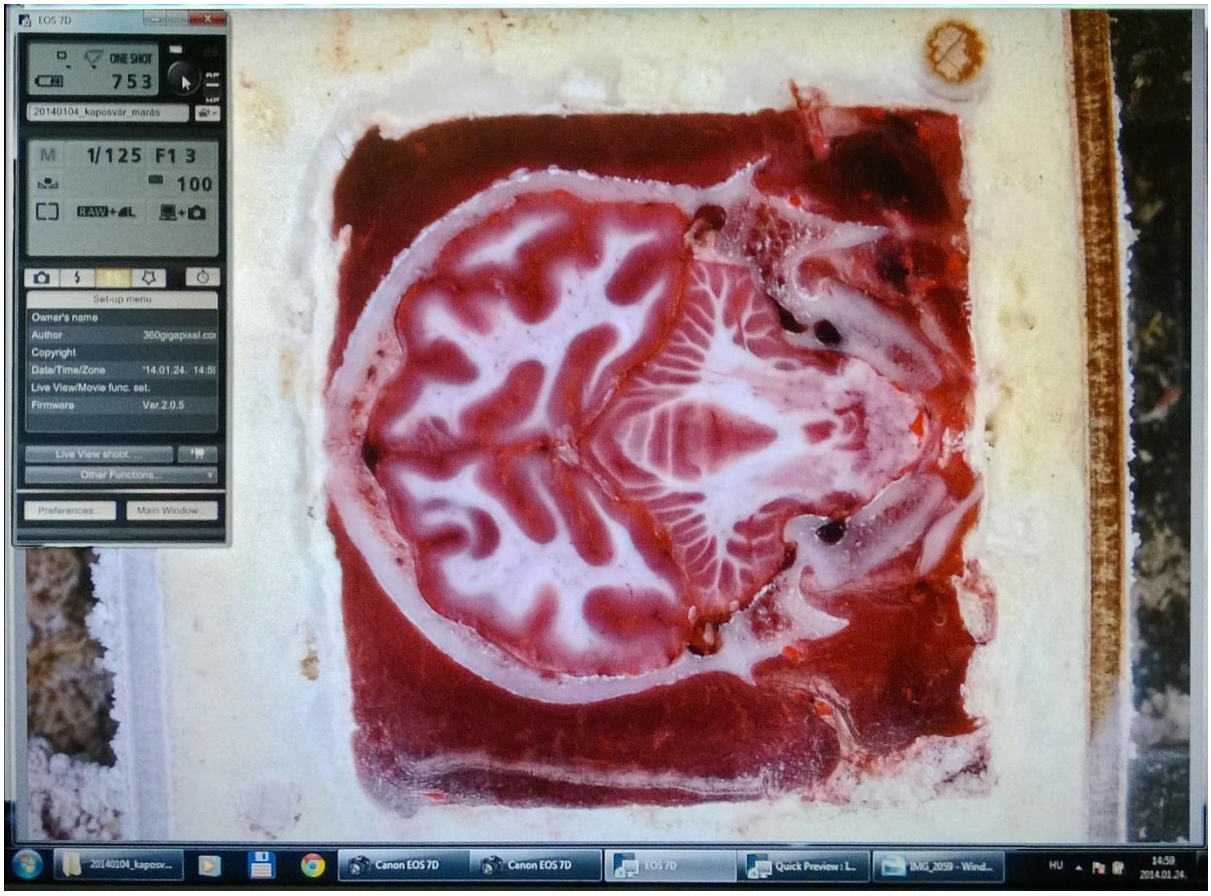

Figure 3. Checking an image on a notebook to assess its quality after taking a photograph from the polished surface. Transverse section at the level of the cerebellum of a dog.

4.1.3. Study III: Cryosectioning the complete head of cat

For the third cryomacrotomisation test we used the cadaver of an adult domestic shorthair cat (*Felis catus*). During this study, we also wanted to perform a structural imaging examination prior to the cryosectioning, as our final goal was to create an effective workflow that included both the structural imaging and the cryomacrotomisation of a dog head. In the first step, we designed a double-walled plexiglass box, which was intended to hold the head during the MRI and CT studies, and which we used during the embedding procedure (**Figure 4**).

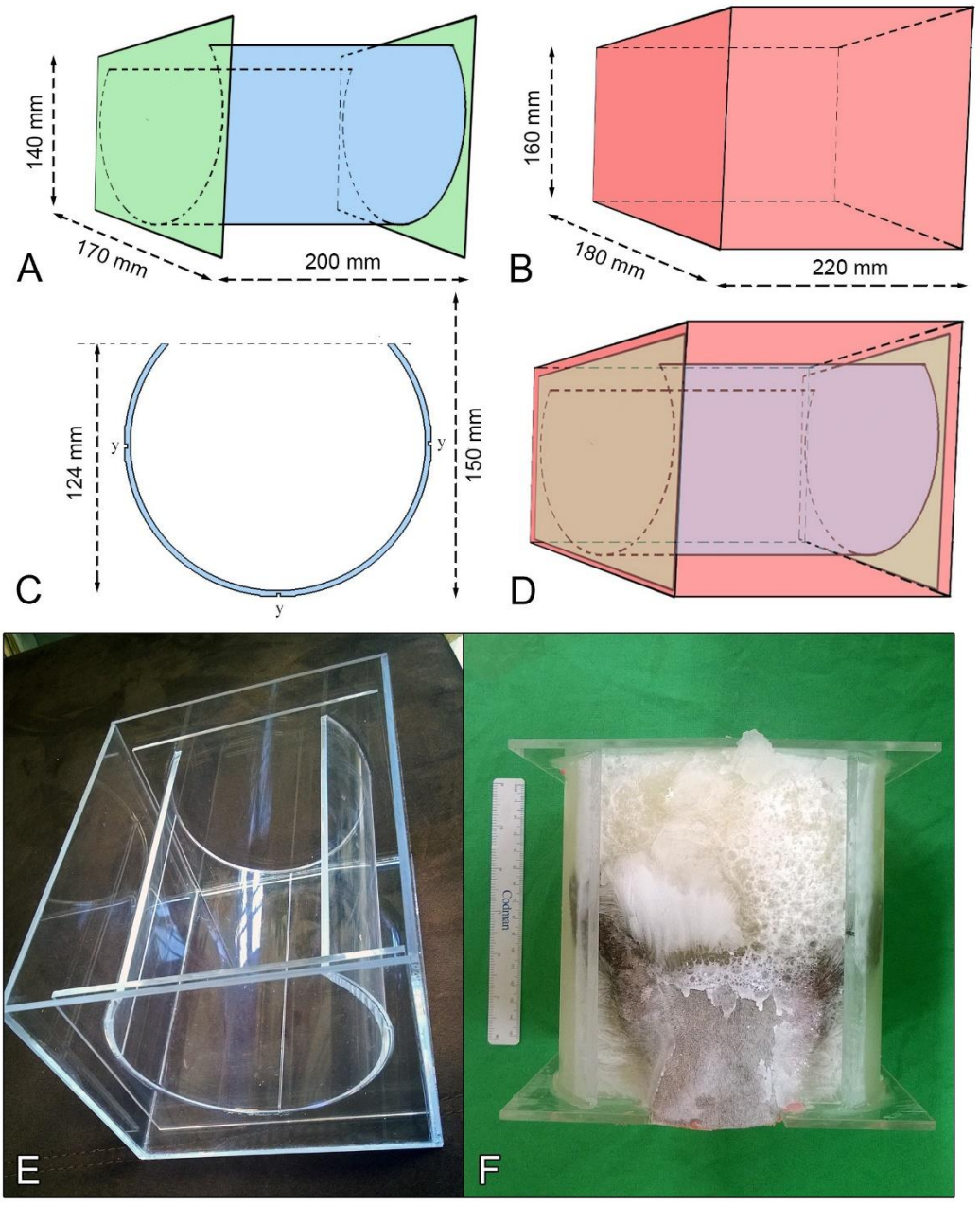

Figure 4. Designing the plexiglass embedding box. A) Inner container. B) Outer container. C) Cross-section of the inner container. D) Inner container placed into the outer container. E) Before the embedding procedure. F) A cat head embedded into the inner box.

The arteries of the head were filled with red polyurethane rubber (VytaFlex-10, Smooth-On Inc., Macungie, Pennsylvania, USA) through the left and right common carotid arteries, and the cadaver was stored at 4°C for 2 days before the structural imaging was performed. The MR scanning was accomplished using a 3 Tesla (3T) Magnetom total imaging matrix (TIM) trio whole-body MRI scanner (Siemens AG, Erlangen, Germany) with a 12-channel phased array head coil, during which the following sequences were obtained: T2-weighted sequence in the sagittal plane (repetition time (TR) = 1000 ms, echo time (TE) = 137 ms, slice thickness = 0.68 mm, field of view (FOV) = 96×175 mm^2 and a 256×256 matrix with voxel size of 0.68×0.68×0.68 mm). Following the MR imaging, the animal was transferred in the same position to the CT unit, where CT scans were obtained using a Siemens Somatom Perspective 128 slice CT (Siemens AG, Berlin and München 2013) (140 kV, 350 mAs, slice thickness = 0.75 mm, pixel size = 1.797×1.797, pitch = 0.75, spiral scanning mode with a B30s bone kernel). The cranio–cervical region was scanned up to the sixth cervical vertebra (**Figure 5**).

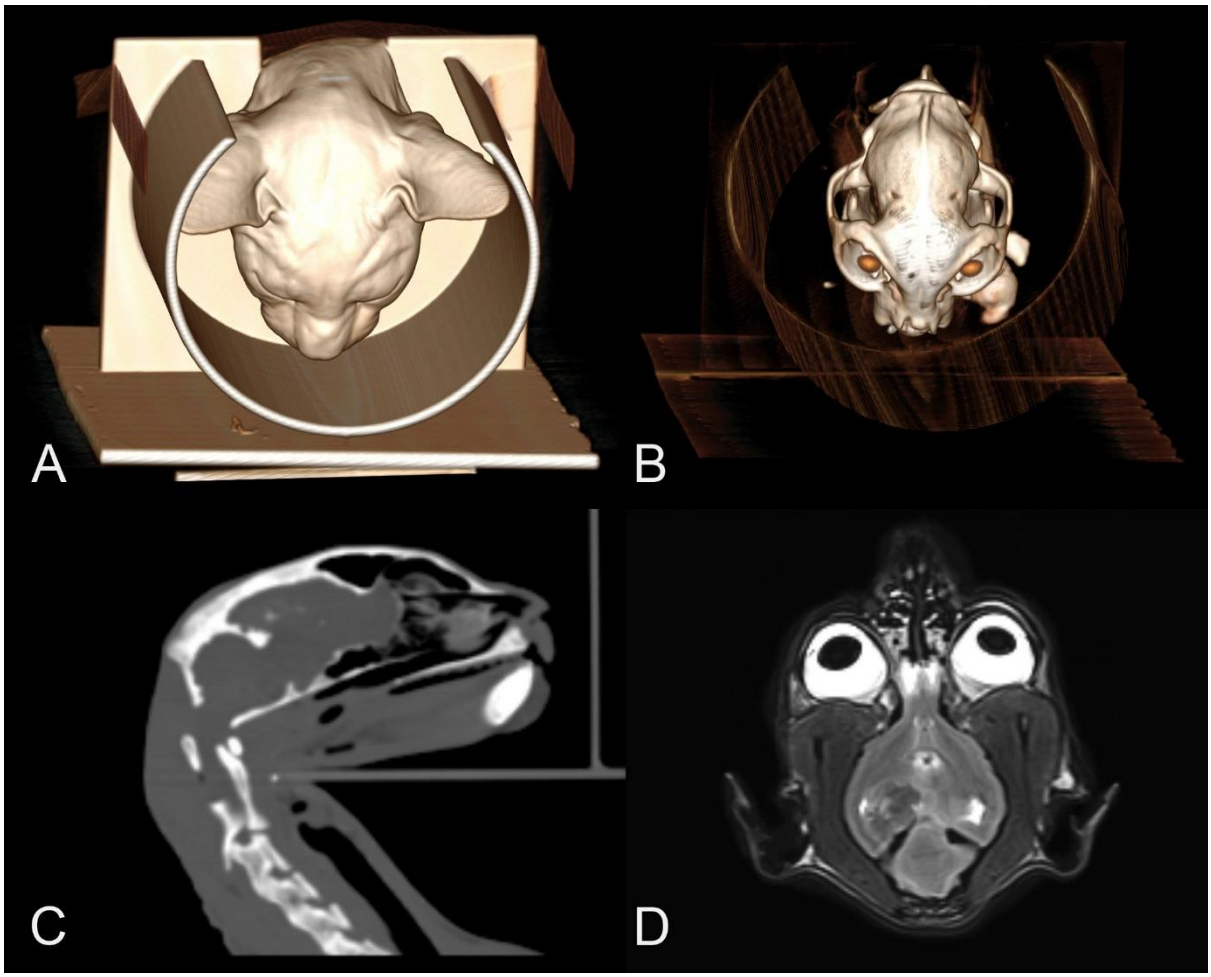

Figure 5. The position of the cat head in the box during the structural imaging.
A, B) CT-based 3D volume-rendered images with different tissue kernels.
C) CT image in the sagittal plane. D) T2-weighted MR image in the dorsal plane.

Afterwards, the inner box (**Figure 4/A)** was filled around the head with a gelatin solution (30 grams of household gelatin dissolved in 1 litre of distilled water during continuous heating, similar to Park et al. (2005), but we did not use any dye to colorize the embedding material), and the body together with the embedding box was frozen at -30°C (**Figure 4/F**). After 24 hours, the head was separated from the body, and the block was placed into the outer embedding box. The same embedding material was poured around, and the entire block was frozen at -80°C. The cryomacrotomisation took place 2 weeks later, using a Dufour G230 universal milling machine (Gaston Dufour, Montreuil, France; rotational speed = 500 RPM, cutter diameter = 200 mm, feed rate = 688 MPR) (**Figure 6)**. During the cryomacrotomisation we used 10% isopropyl alcohol to clean the surface of each section, which not only provided a cleaner image but also slowed the surface refreezing to allow a few seconds while taking the photo. To photograph the surface, we used a Canon EOS 5D Mark II DSLR camera and a Canon EF 100 mm f/2.8 macro USM lens with polarised filters (ISO-100, focus distance 100 mm, exposure time 1/200 sec, max aperture 3.0, F-stop f/13, with X-Rite ColorChecker passport and polarising filters) (**Figure 7**). Photos were recorded in 24-bit colour depth and 240 DPI raw images; the dimension of each picture was 3632×4350 pixels. Proceeding from a caudo–rostral direction, we recorded 260 images of the entire head from the level of the second cervical vertebra to the tip of the nose, with a milling interval of 400 μm.

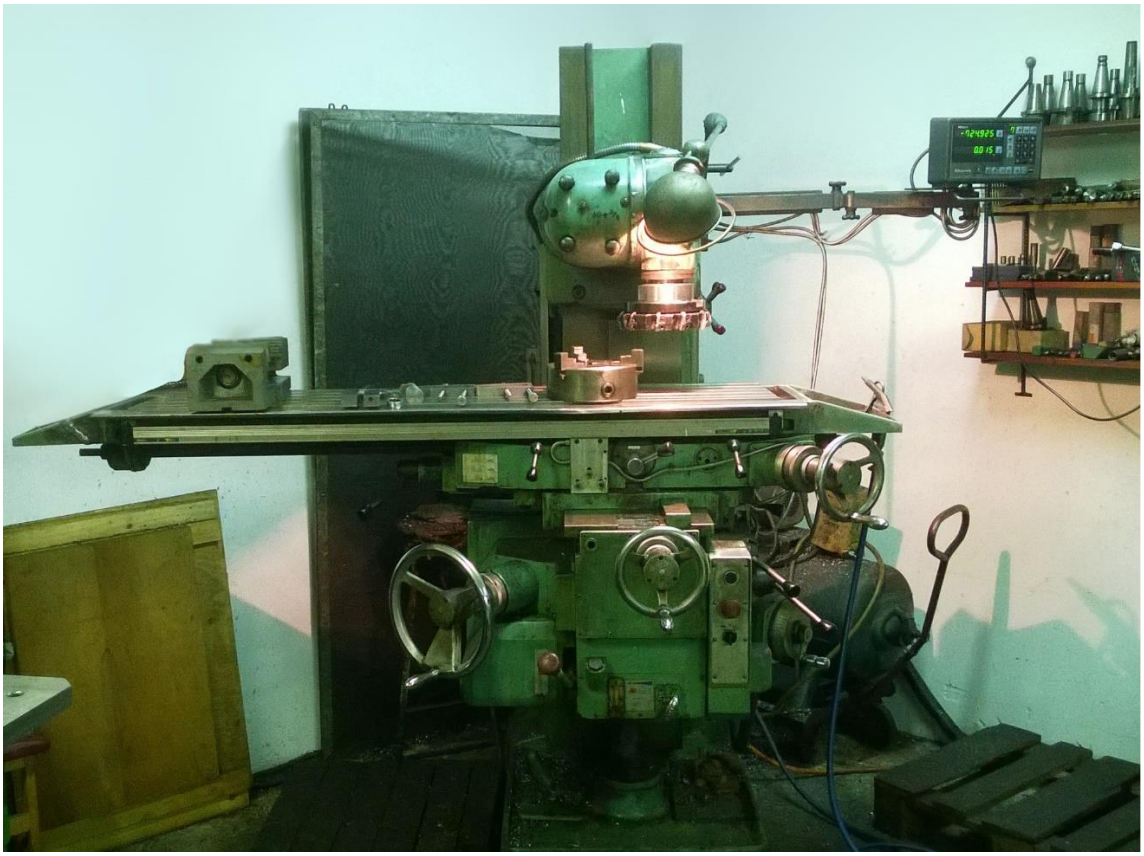

Figure 6. The Dufour universal milling machine which was used in the third pilot study.

Figure 7. During the cryomacrotomisation process. A, B) Recording the white balance and colour values with a ColorChecker passport. C) The cat head in the frozen gelatin. D) The plexiglass box, surrounded with dry ice pellets during the milling.

4.1.4. Study IV: Cryosectioning the head block of a cat

To test another milling system and to gain more information about the technicalities of the cryosectioning process, in our next trial study we used a custom-made (ICI Interactive Ltd., Budapest, Hungary) 3-axis high-speed computer numerical control (CNC) milling machine with a 2-flute end mill (**Figure 8**). The subject of the study was the head from an adult domestic shorthair cat (*Felis catus*) cadaver that we embedded into the same gelatin solution described in Study III. After the freezing process, the plexiglass box containing the head was cut in half with an electric saw to expose the neurocranium and the brain inside. We used just one half of the block as now we wanted to test the milling procedure only on a few subsequent images to assess the quality, with different rotational speeds and feed rates (rotational speed ranged between 1000 and 18000 RPM, cutter diameter = 6 mm, feed rate = 600 MPR). The part of the embedding box that contained the head block from the level of the optic chiasm to the medulla oblongata was stored at -80°C for 10 days until the cryomacrotomisation.

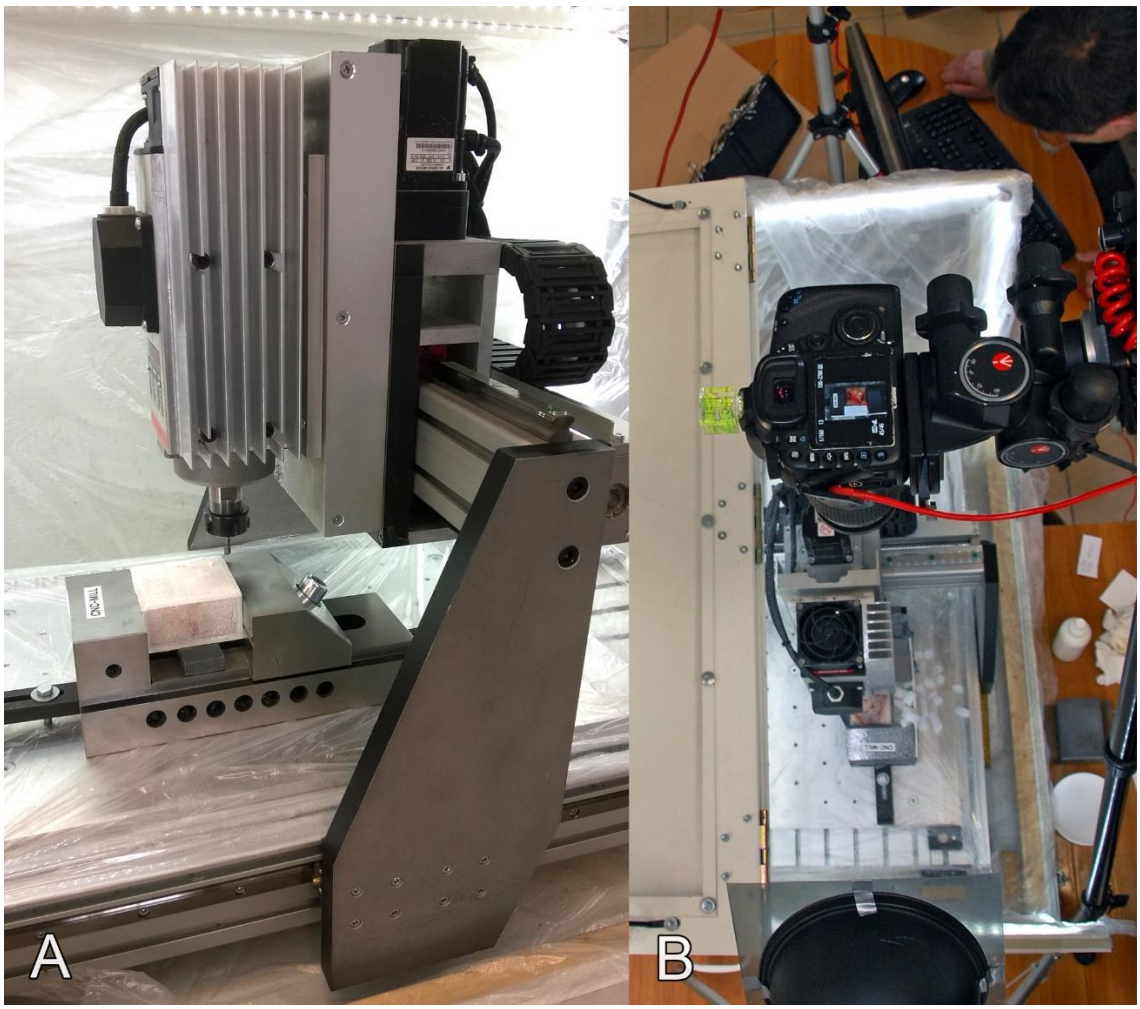

Figure 8. Cryosectioning a neurocranium block of a cat with a high-speed CNC machine. A) The device and the head block from the side. B) The camera above the milling area.

To capture the images, we used a Canon EOS 7D camera and a Canon EF 100 mm f/2.8 macro USM lens with polarised filters (ISO-100, focus distance 100 mm, exposure time 1/160 sec, max aperture 3.0, F-stop f/13, with X-Rite ColorChecker passport and polarising filters). Photos were recorded in 24-bit colour depth and 72 DPI raw images, and the dimension of each picture was 3441×5161 pixels. The box was fixed to the table, and dry ice was used to cool the side of the block. The dry ice pellets were in direct contact with one side of the box and froze the metal holders (vise) on the two other sides (**Figure 9**). Surface cooling before each milling step was achieved by pouring dry ice slivers onto the top of the block, and cleaning was performed with 10% isopropyl alcohol afterwards. Layer interval of the milling was 200 µm. Overall, we recorded 17 images from the middle of the skull.

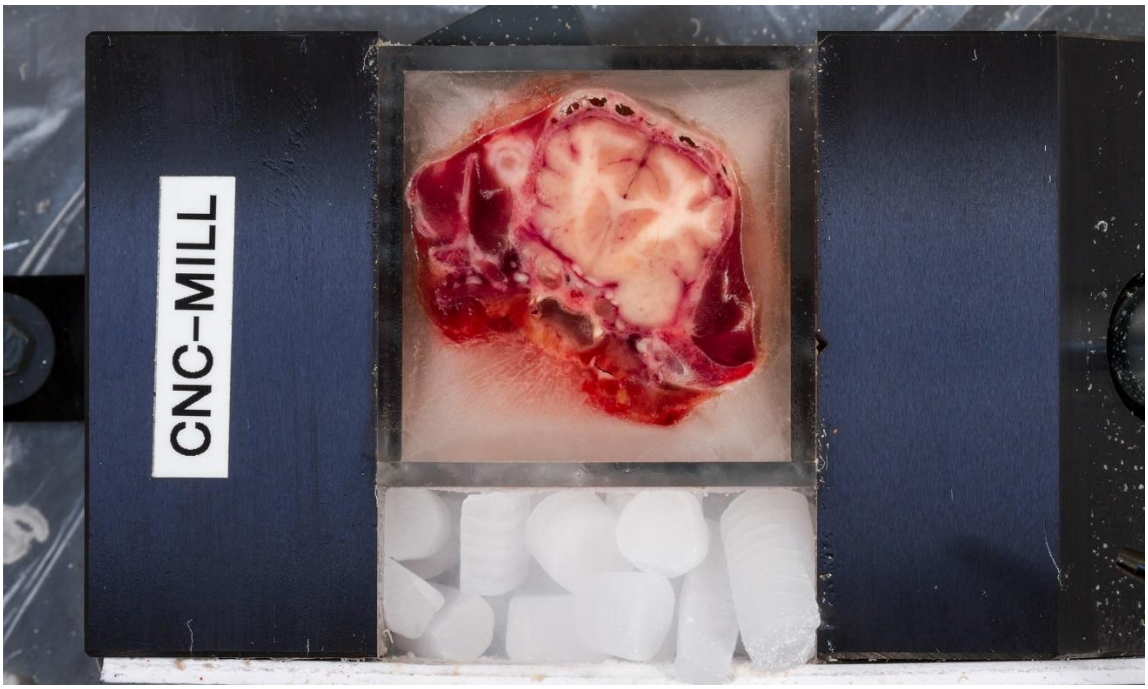

Figure 9. Camera view of the head block of a cat with the vise and the dry ice pellets.

4.1.5. Study V: Cryosectioning the head block of a dog

The fifth experiment was carried out using a Kondia NCT B-640 precision CNC milling machine (NCT Industrial Electronics Ltd., Budapest, Hungary) (**Figure 10**). The head of an adult American Staffordshire terrier (*Canis familiaris*) cadaver was frozen at -30°C and was then cut based on external landmarks at the level of the external occipital protuberance to create a symmetrical transverse plane (ensuring that during the cryomacrotomisation the symmetry would be maintained). The head was then embedded into a plexiglass box filled with gelatin solution and was frozen at -80°C. After hardening, we cut the block at the mid of the neurocranium to create a smaller segment because we intended to test whether the system could provide a sufficient milling quality of the bones, muscles and brain tissue.

For the digitalization process, we used a Canon EOS 7D camera and a Canon EF 100 mm f/2.8 macro USM lens with polarised filters (ISO-100, focus distance 100 mm, exposure time 1/125 sec, max aperture 3.0, F-stop f/10, with X-Rite ColorChecker passport and polarising filters). Photos were recorded in 24-bit colour depth, with 240 DPI raw images; the dimension of each picture was 5021×2942 pixels. The surface of the block was cooled with dry ice pellets and liquid nitrogen, and was cleaned after each milling step with isopropyl alcohol. We used different settings to test the properties of the machine (rotational speed = 3000 – 4000 RPM, cutter diameter = 200 mm, feed rate = 300 – 400 MPR, with a layer thickness of 50, 100 and 400 μm). Overall, we recorded 16 images from the mid of the skull until we could clearly evaluate the efficiency of the system (**Figure 11**).

Figure 10. The Kondia CNC milling machine which was used during the fifth pilot study.

Figure 11. The cryosectioning process. A) Mounting the camera system and isolating the milling area. B) The neurocranial block of the dog in the vise and the flywheel.

4.2. Inferences based on the pilot cryosectioning studies

4.2.1. Evaluation of Study I

By using a band saw and DSLR photography, we obtained high-resolution images from the whole body of a pig, where the structure of the individual muscles and muscle groups were well recognisable (**Figure 12**). When considering that our final aim was to make cryosections from a dog neurocranium to provide detailed images of the brain, the photographic settings were found to be appropriate, but the band saw sectioning was not suitable for the fine cryomacrotomisation procedure because: (a) this slicing method is not applicable to larger objects, as a slice thicknesses less than 1-2 mm can result in unintentional side-movements of the blade due to its relatively long route inside the block, resulting in uneven slice widths; (b) the abrupt change in the tissue hardness (e.g., brain-bone transition) makes the cutting unpredictable and rugged; (c) possible damage to the band saw teeth can result in artefacts on subsequent images; and (d) the handling of thin slices requires more time and precision, which results in an overall extension in the sectioning time. These were the main reasons, why we decided to test the milling procedure in our subsequent pilot experiments.

Figure 12. Transverse section of a pig at the level of the first thoracic vertebra. 1) Vertebra thoracis I. 2) M. serratus ventralis, pars cervicis. 3) M. infraspinatus. 4) M. triceps brachii. 5) Humerus. 6) M. pectoralis profundus. 7) M. subclavius. 8) M. pectoralis superficialis. 9) M. extensor carpi radialis. 10) M. longus capitis. 11) Oesophagus. 12) Trachea. 13) M. biventer cervicis. 14) M. spinalis cervicis et thoracis. 15) M. complexus.

4.2.2. Evaluation of Study II

The study with the JAFO FWD-32U universal milling machine proved that we could obtain images from a tissue block with a regular milling interval which can be decreased below 1 mm, but it also highlighted some issues that had to be improved during the subsequent studies. The main conclusions of this study were as follows:

- The proper cooling is one of the most important factors during cryosectioning. If the surface is not maintained at a relatively low temperature, then smearing of the tissue can be present (e.g., seen on the upper eyelids in **Figure 13**); conversely, if the surface is not warm enough after milling, it causes details to be lost in the image due to surface refreezing (**Figure 14**).
- Treating the block with dry ice and liquid nitrogen to keep the block solid during the milling procedure caused the polyurethane foam to separate from the block and also created clefts inside the foam, thus the embedding agent had to be changed in the upcoming pilot studies.
- Although warming up the milled surface before photography resulted in good contrast and a sufficient level of detail in the tissues, we still observed small freeze lines inside the brain that probably formed during the initial block making and freezing processes (**Figure 15**).
- The colour of the grey matter in the images was darker and more reddish compared to a fresh brain, which was most likely due to the postmortem autolytic processes in the tissues. Thus, the later imaging and embedding procedures were recommended to be completed in the shortest possible amount of time (ideally less than 24-48 hours).
- The milling roll contaminated the material not only in the area immediately surrounding the machine (which we thus continuously cleared with a vacuum), but a small amount of the debris also had to be removed from the milled surface before photography (**Figure 16**). This is one of the reasons why vertical milling is usually preferred over horizontal milling.
- The surface had to be cooled equally (and to a sufficiently low temperature, preferably with dry ice; liquid nitrogen should only be used when smearing or fibre formation is present). The larger dry ice granulates tended to cause regionally deeper freezing, which was subsequently visible by the unequal shading of the surface.
- The width of the milling wheel would be a limiting factor when using this type of machine to mill larger objects, as with the applied settings the block could only move along one axis.
- The table with the fixed embedding box had to be moved to the end-position manually where the camera located, thus this back and forth movement increased the working time.

Overall, we collected a lot of experiments during this cryosectioning procedure, and identified those main challenges that could be expected during the embedding and the milling process.

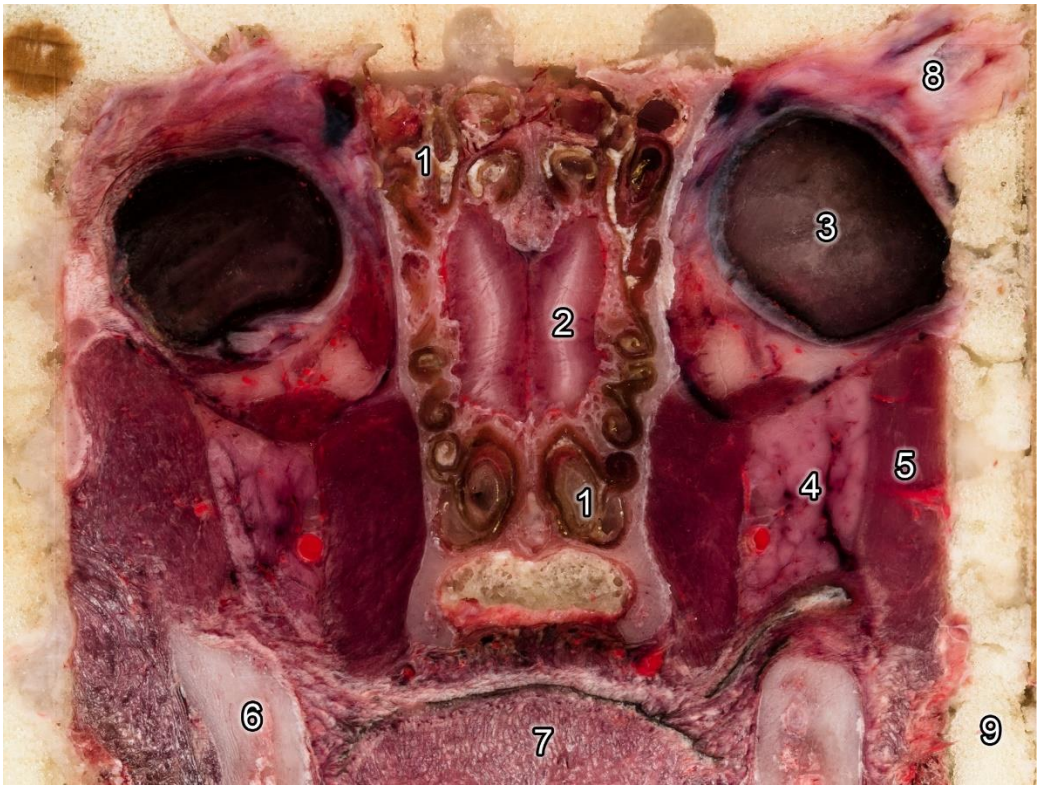

Figure 13. Transverse section of a dog head block at the level of the orbit.
1) Ethmoturbinalia. 2) Bulbus olfactorius. 3) Bulbus oculi. 4) Glandula zygomatica.
5) M. masseter. 6) Mandibula. 7) Lingua. 8) Tissue smearing. 9) Embedding foam.

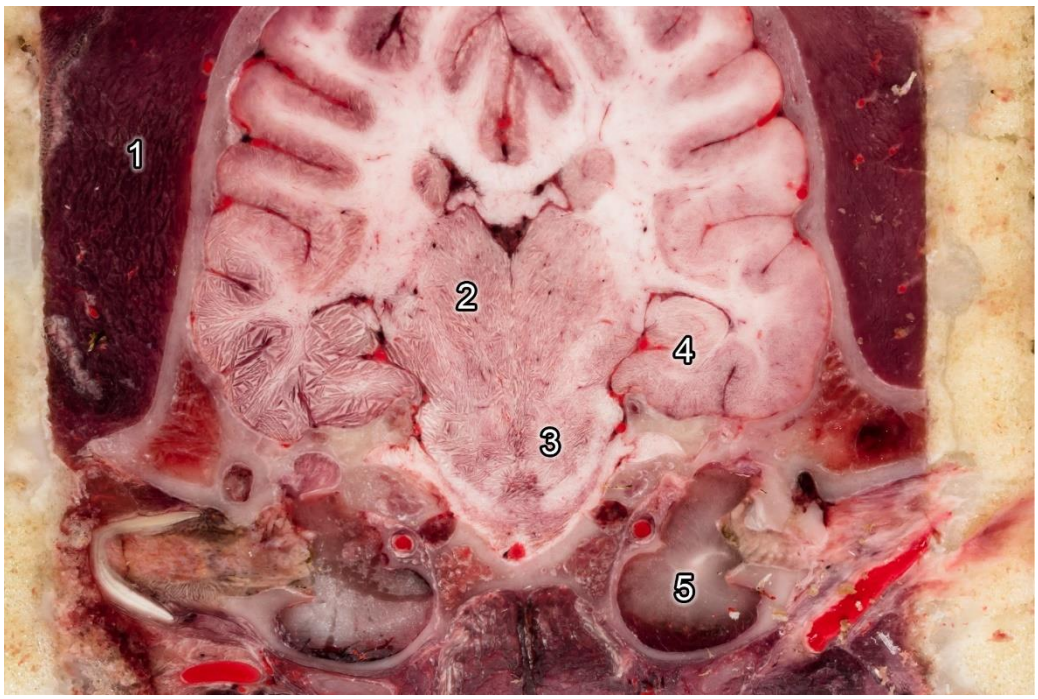

Figure 14. Transverse section of a dog head at the level of the bulla tympanica.
Photo was taken immediately after milling and surface is faded due to the refreezing.
1) M. temporalis. 2) Thalamus. 3) Area pontina. 4) Hippocampus. 5) Bulla tympanica.

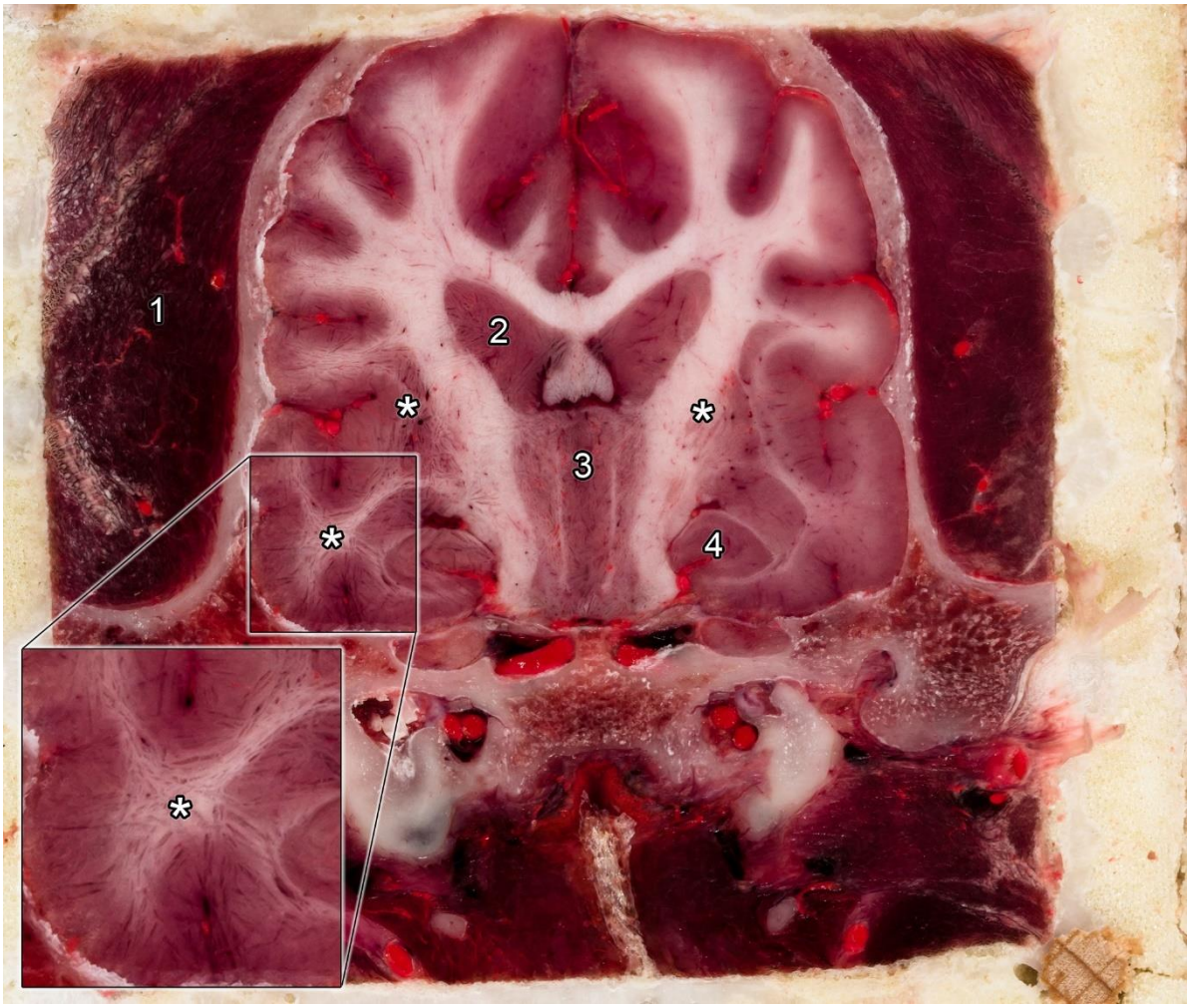

Figure 15. Transverse section of a dog head block at the level of the dorsum sellae. 1) M. temporalis. 2) Nucleus caudatus. 3) Thalamus. 4) Hippocampus. *) Freeze lines.

Figure 16. Image showing the tissue debris (*) around the head block of a dog. These fragments contaminated the surrounding regions and the surface of the embedding box.

4.2.3. Evaluation of Study III

We had some improvements during the third pilot with the Dufour universal milling machine. Surface contamination was decreased, a plexiglass box with a better embedding matrix was used, the postmortem time was around 72 hours, and cooling was more equal from the side and from the top by using dry ice pellets. However, we could see circular stripes on the milled surface (**Figure 17**), because compared to the previous trial's system this machine had a face milling cutter, which was rotating around the z-axis. The embedding box was secured to the machine's milling table, and to provide sufficient continuous cooling we placed a cardboard box around the block and filled it with dry ice (**Figure 7/D**), which was replaced regularly during the cryosectioning process. The gelatin solution was proved to be a good embedding agent that could be maintained at a low (around -70°C) temperature, but the loss of dry ice that had to be replaced during the cryosectioning procedure was extensive, as a consequence of its direct contact with the warm air above and the poor thermoregulation at the cardboard's sides. Additional findings were that the embedding agent penetrated into the cavity of the right middle ear, presumably due to *a priori* damage or weakening of the eardrum. We could also see a large intracranial extra-axial tumour, which dislocated the brain from the midline (**Figure 18**).

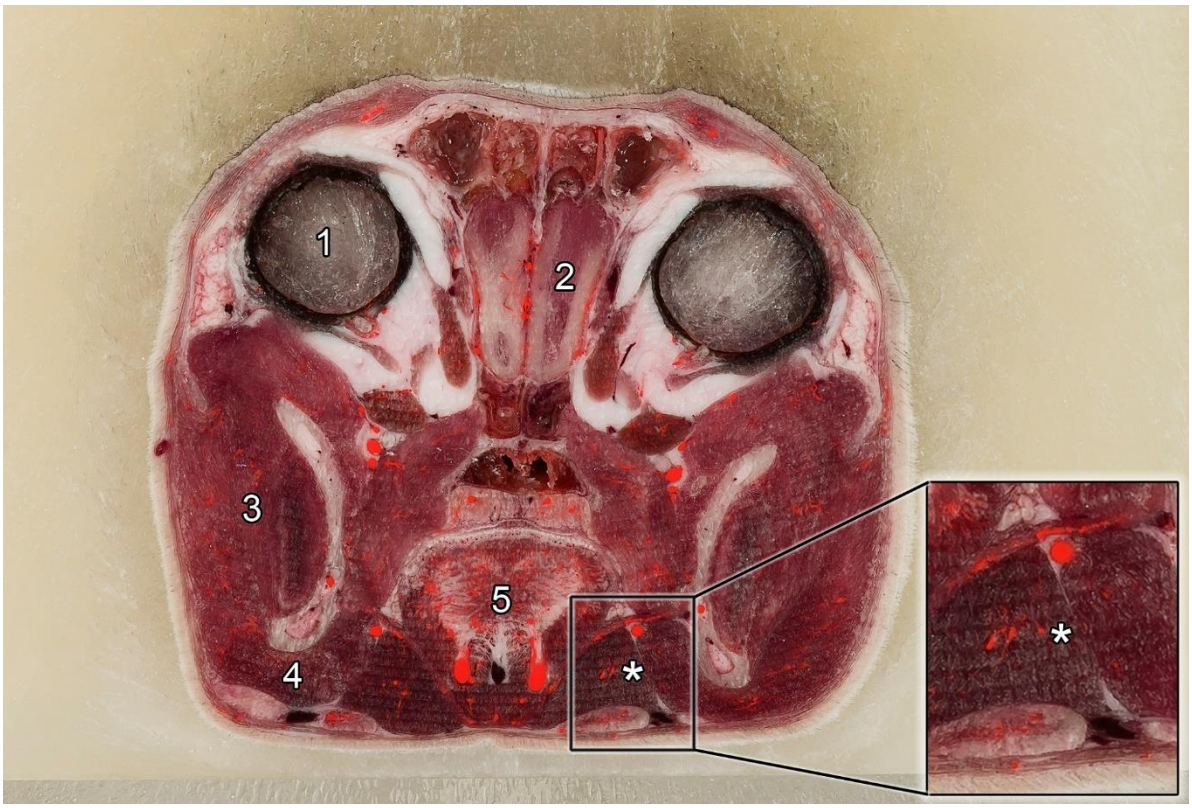

Figure 17. Transverse section of a cat head at the level of the orbit. Circular stripes (*) can be seen on the surface (especially on the muscles) as a consequence of the milling. 1) Bulbus oculi. 2) Bulbus olfactorius. 3) M. masseter. 4) M. digastricus. 5) Lingua.

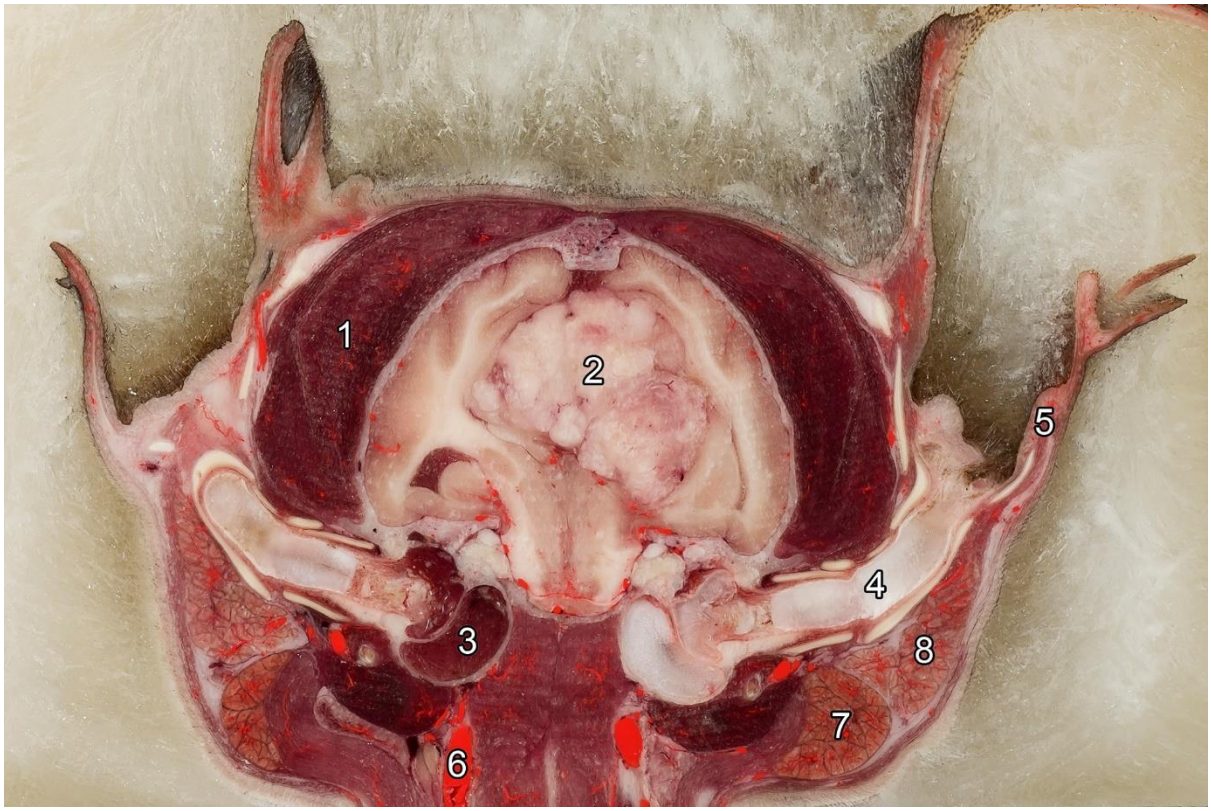

Figure 18. Transverse section of a cat head at the level of the external auditory canal. 1) M. temporalis. 2) Intracranial tumour. 3) Bulla tympanica. 4) Meatus acusticus externus. 5) Auricula. 6) A. carotis externa. 7) Glandula mandibularis. 8) Glandula parotis.

4.2.4. Evaluation of Study IV

Compared to the previous trials, it was a great advantage with the custom-made CNC machine that the block could remain constantly in the same position after the milling, while the camera recorded the images. In this way, the cleaning and photography could be performed earlier, thus the required processing time per surface could be decreased. On the other hand, we concluded that: (a) it is essential to precisely define the transverse plane of the block, as it later impacts how symmetrical the milling plane will be (e.g., the size of the caudate nucleus and the piriform lobe show a mild asymmetry compared to their counterparts in **Figure 19**); (b) it is better to fill the arterial system with a resin (as we did in the previous cryosectioning studies), because the vessels (arteries and veins) can be more easily identified; (c) the smaller 2-flute end mill scattered more milled particles onto the surface compared to the milling wheel; (d) a consequence of the point-like milling head is that stripes were present on the surface, as seen in **Figure 20**; (e) the milling route could be individually planned and guided with this CNC system (which was advantageous), but as the contact milling area was relatively small, it took a longer time to proceed with the milling which resulted in the uneven refreezing of the surface.

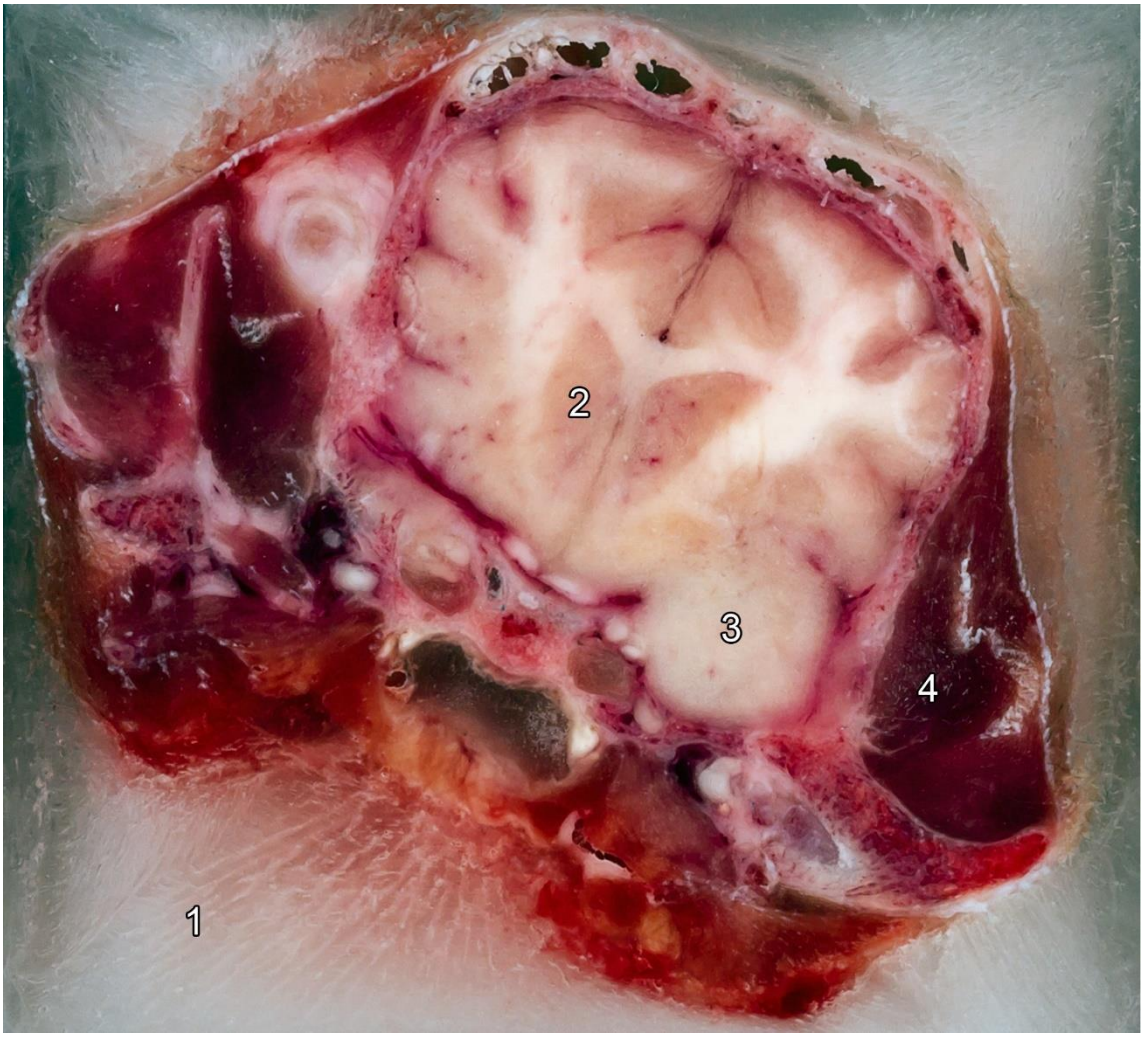

Figure 19. Transverse section of the cat head at the level of the caudate nucleus.
1) Frozen gelatin solution. 2) Nucleus caudatus. 3) Lobus piriformis. 4) M. temporalis.

Figure 20. During the cryomacrotomisation of a cat head block with a 2-flute end mill.

4.2.5. Evaluation of Study V

The Kondia CNC milling systems fulfilled all of those main requirements we set, as follows: (a) it provided a continuous high precision milling without the need of manual intervention; (b) due to the large milling diameter, the wheel could cover the entire surface of an average neurocranium block, performing the milling in one turn; (c) the embedding box could be moved automatically to arrive under the camera in the same position after each milling step; (d) this system provided an excellent surface quality, and no stripes or surface contamination were present. Regarding the cooling, we observed that initially when the entire block was solid and frozen the surrounding embedding mixture provided a sufficient cooling effect, which resulted in a quick surface fading. This fading was addressed by applying isopropyl alcohol to retain the original colours and sharp contours (**Figure 21**). However, the warm atmosphere and the heat derived from the milling process caused the embedding agent to melt, even though we cooled it continuously from one side with dry ice. Thus, providing proper thermoregulation is a crucial element, ideally surrounding the entire tissue block with dry ice to achieve maximal thermal exchange. On an average, one milling step (between two consecutive layers) was carried out in approximately one minute. Furthermore, due to the high speed and the large flywheel, the milled fragments were rolled out from surface to the side of the milling space; thus, they did not contaminate the block's surface, and it made easier to collect the waste.

4.2.6. Conclusion of the pilot cryosectioning studies

Based on the cryomacrotomisation studies, we could answer our initial questions:

- Is there a need for postmortem **perfusion**?
  - If the cadaver is fresh (within 24 hours postmortem), then no special tissue fixative is required (like formalin), but it is advised to fill the arterial system with a colorized agent.
- What is the proper **embedding agent**?
  - The gelatin solution was proved to be a good material during the pilot experiments.
- What kind of tissue **embedding box** should be constructed?
  - A double-walled plexiglass container, which also has an outer thermoregulation layer.
- Which type of **milling machine** is ideal for the cryosectioning?
  - The Kondia CNC milling system provided the best quality among the pilot studies.
- How to provide correct **thermoregulation** during the procedure?
  - Continuous cooling can be achieved with dry ice, occasionally applying liquid nitrogen, and by limiting the size of the non-thermoregulated contact area with the environment.
- What are the appropriate settings for the **image recording**?
  - High-resolution DSLR camera with macro lens and polarising filters are recommended, a colour checker should be used, and a simultaneous computer control is advised.

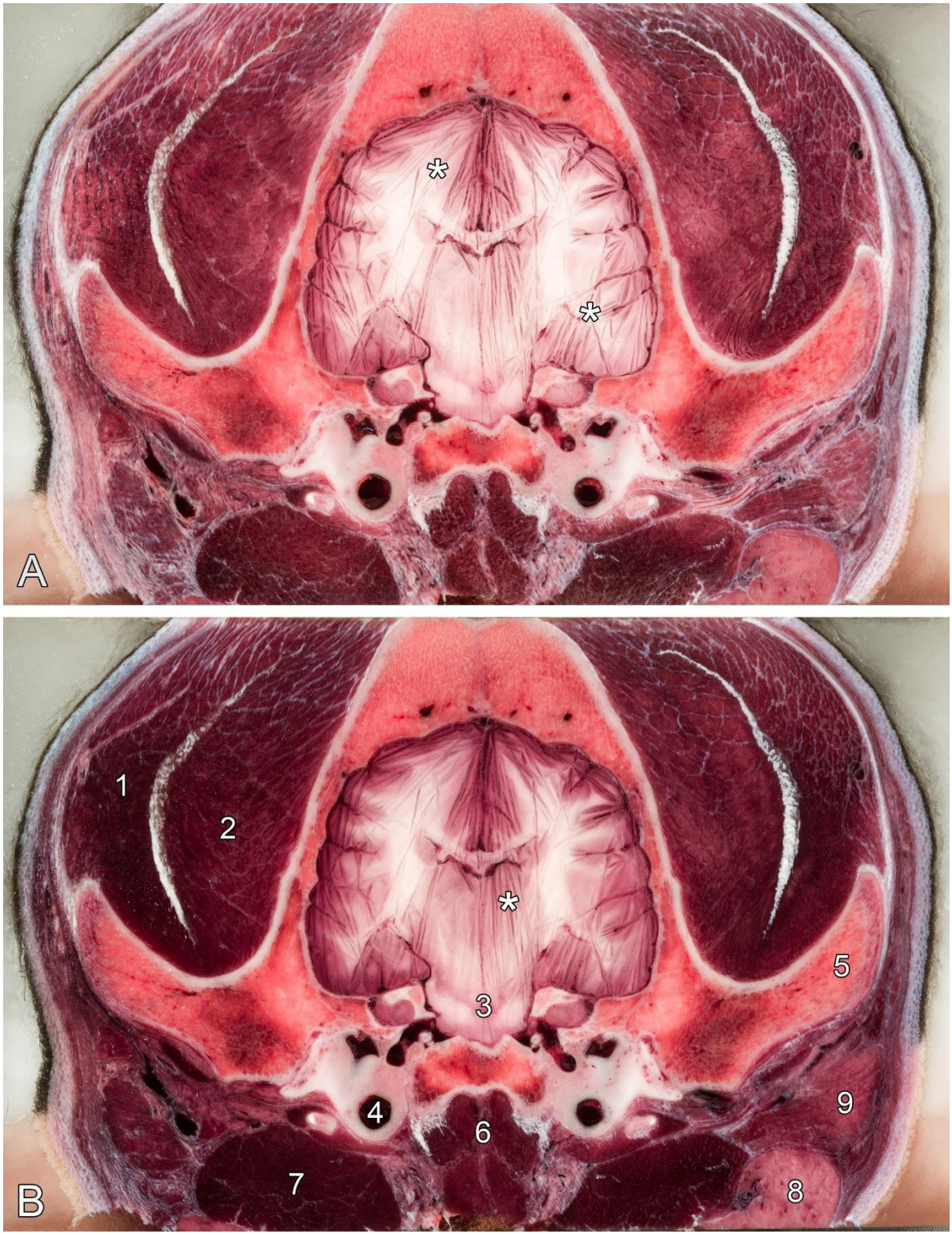

Figure 21. Transverse section of a dog head block at the level of the tympanic bulla. A) Showing the surface fading due to rapid refreezing. B) The same layer as in part “A”, after cleaning up with isopropyl alcohol. 1) M. temporalis, pars superficialis. 2) M. temporalis, pars profunda. 3) Regio pontina. 4) Bulla tympanica. 5) Arcus zygomaticus. 6) M. longus capitis. 7) M. digastricus. 8) Glandula mandibularis. 9) Glandula parotis. *) Freeze line artefacts.

4.3. Conducting pilot studies in visualisation

In parallel with the pilot cryomacrotomisation experiments, various software packages were assessed to optimise the visualisation, to practice their use and gain in-depth knowledge of them. The ideal software for processing the cryosectioned images is required to handle large amounts of data (i.e., tens of gigabytes), and it must be able to make one scalar volume and multiplanar reconstructions from the coloured images. Additionally, the CT and MRI datasets must be able to be merged within the same project view, and the software must have tools for segmentation and 3D modelling. Within this framework we made four visualisation studies.

4.3.1. Study VI: Making the osseo-vascular 3D model of a canine head

An adult French bulldog (*Canis familiaris*) cadaver was used for the first 3D visualisation study. The arteries of the head and neck were filled with colorized polymethyl-methacrylate resin (Acrifix 2R 1900; Evonik Industries, Essen, Germany) through the brachiocephalic artery and the left subclavian artery postmortem, both of which were ligated rostral to the costocervical arteries to ensure that the red resin flowed only towards the head and neck arteries and did not leak into the forelimbs. Subsequently, the head and neck were separated from the body at the level of the third thoracic vertebra and immersed into a container filled with water and a biological activator (Septifos Vigor powder; Henkel, Düsseldorf, Germany). The specimen was placed in a thermostat at 39°C for 3 weeks (changing the fluid on a weekly basis in the container). At the end of the maceration procedure, only the bones and the corrosion cast of the arteries were left, revealing all the major vessels around the cephalic region (**Figure 22**).

Afterwards, we digitised this composite corrosion cast with an YXLON Precision microfocus CT (YXLON, Hamburg, Germany; 200 kV, 2 mAs, number of projections = 1440, FOV = 1024×1024, voxel size = 0.24×0.24×0.24 mm). The digital imaging and communications in medicine (DICOM) images were first reviewed with the RadiAnt DICOM Viewer (freeware software, https://www.radiantviewer.com) (**Figure 23**), and then the dataset was imported into the Thermo Scientific Amira for Life Sciences 6.0 software (FEI Visualization Sciences Group, http://www.fei.com). A new segmentation project was created with the "*Edit New Label Field*" module, where arteries and the osseous structures were separately labelled. Using the "*Generate Surface*" module, two surface mesh models were created and exported in stereolithography (STL) format. The STL models were refined using the Autodesk MeshMixer (freeware software, http://www.meshmixer.com) and then we 3D-printed it to actual size (1:1) using selective laser sintering (SLS) technology, where arteries were colorized with red acrylic dye (**Figure 24**). The main advantage of the 3D printed model that it can be easily replicated in the required number, and compared to the original corrosion cast it is far more durable.

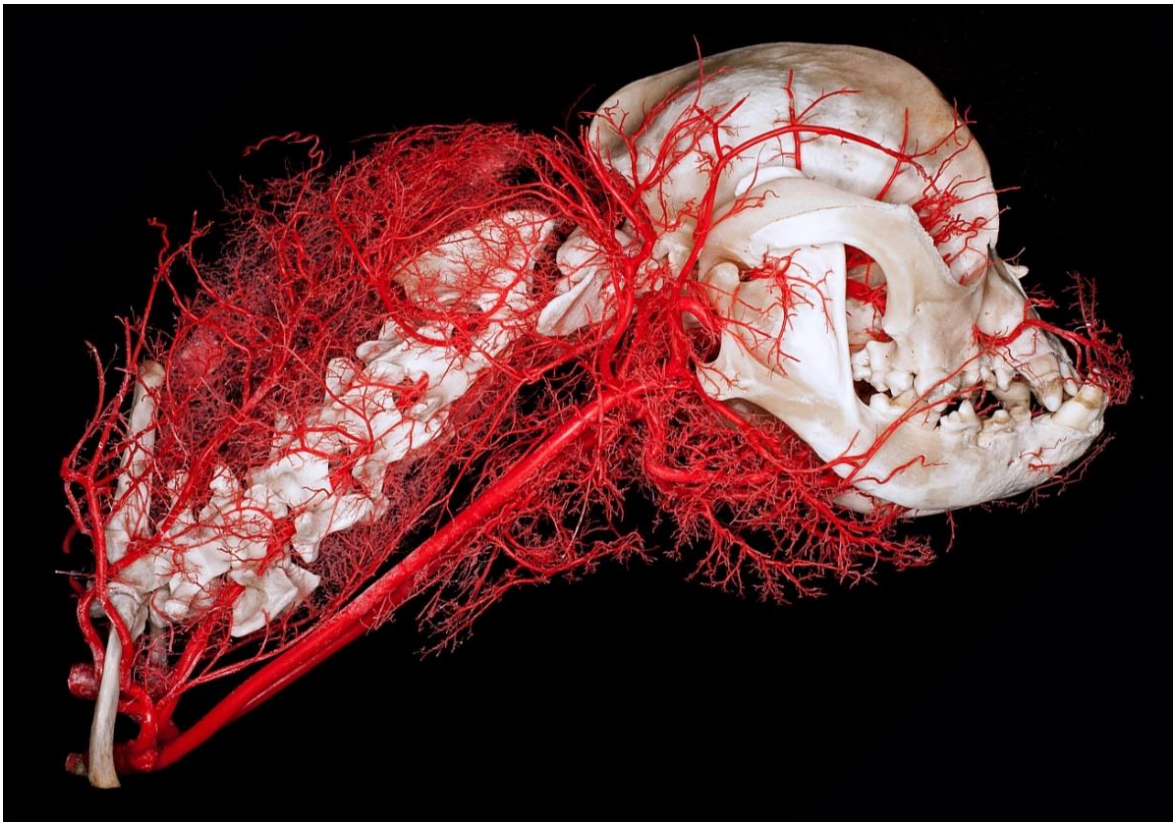

Figure 22. Composite osseo-vascular corrosion cast of a French bulldog head and neck.

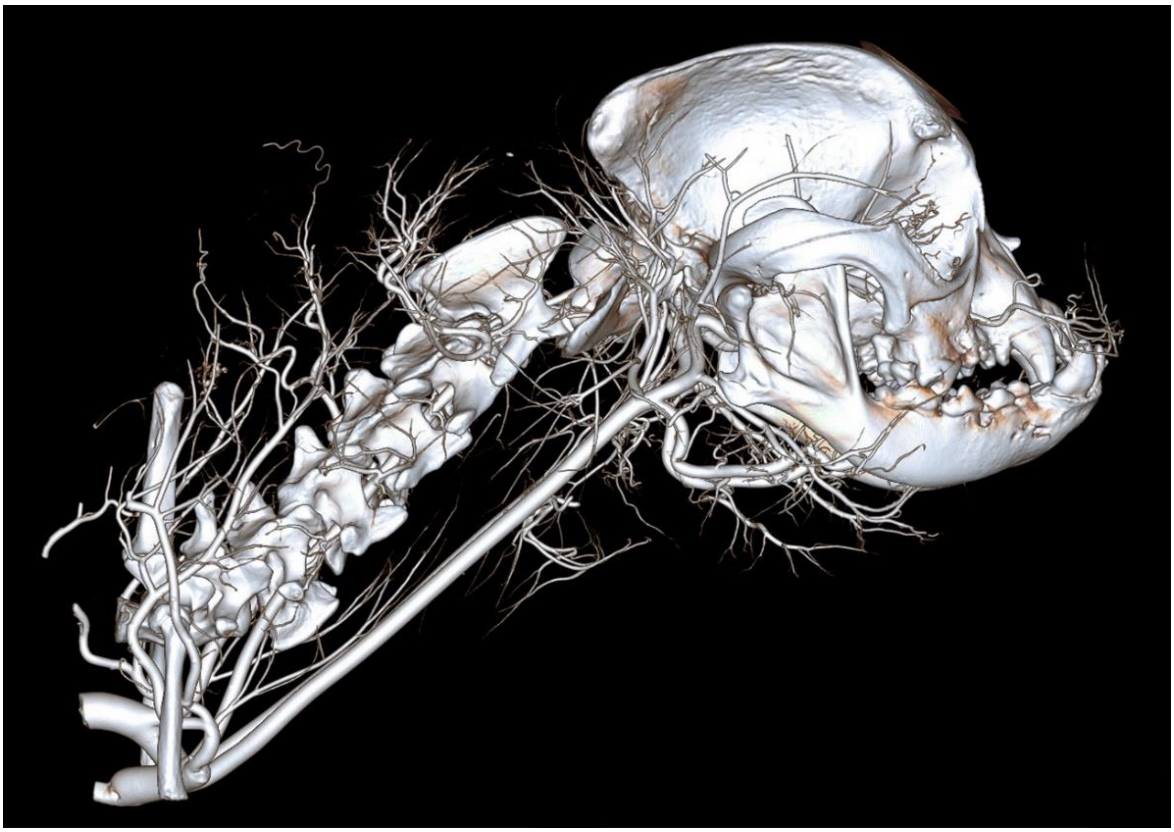

Figure 23. Volume-rendered 3D model of the same French bulldog osseo-vascular cast which is presented in **Figure 22,** based on the CT imaging's DICOM data. Right lateral view.

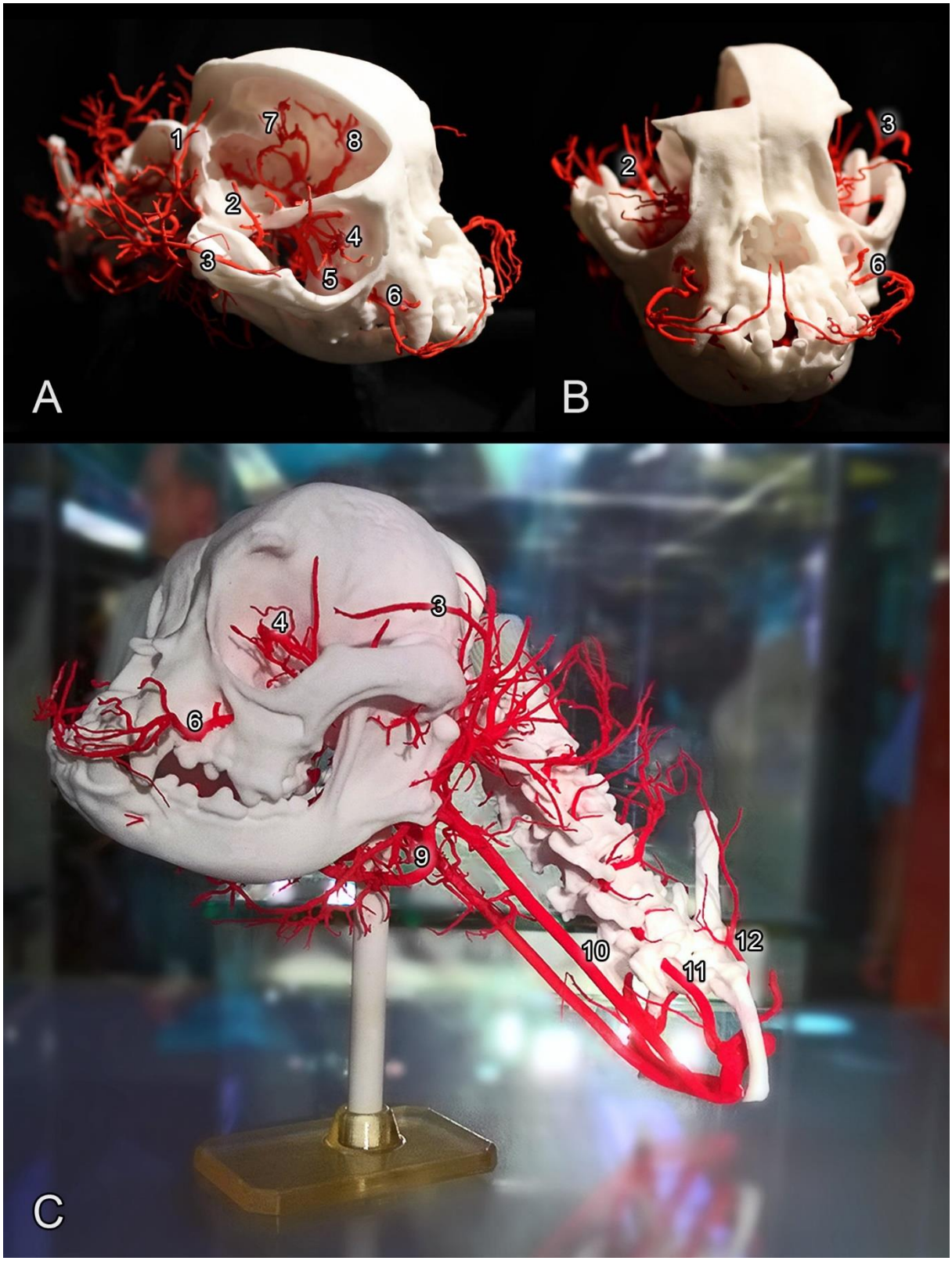

Figure 24. 3D-printed and colorized model of a French bulldog osseo-vascular cast. A) Right dorso-lateral view. B) Rostral view. C) Left lateral view. 1) A. auricularis caudalis. 2) A. temporalis profunda caudalis. 3) A. temporalis superficialis. 4) Rami a. ophthalmicae externae. 5) A. maxillaris. 6) A. infraorbitalis. 7) A. cerebri caudalis. 8) A. cerebri media. 9) A. lingualis. 10) A. carotis communis. 11) A. vertebralis. 12) A. cervicalis profunda.

4.3.2. Study VII: Producing the 3D model of an equine petrosal bone

The petrosal bone is one of the most complex osseous structures in the body, comprising several structures (e.g., auditory ossicles, inner ear) within a small volume. Because these inner structures are not visible from the outside and they have a complex spatial arrangement that makes the understanding of the petrosal bone exceptionally challenging, it seemed an ideal target for a comparative visualisation and 3D modelling experiment. We used an intact left petrosal bone of an adult horse's (*Equus caballus*) skull for the digitalisation procedure. Afterwards, we scanned it with an YXLON Precision microfocus CT (200 kV, 2 mAs, number of projections = 1440, FOV = 1024×1024, voxel size = 0.059×0.059×0.059 mm). The main orthogonal views were assessed with RadiAnt before further processing the images (**Figure 25**). Using the Amira software, segments were created for the petrosal bone, the auditory ossicles (malleus, incus, os lenticulare, stapes), the inner ear and for the facial canal. From each of the segments separate STL models were created and a specific colour was assigned to each structure. We took photographs from the real petrosal bone, and by setting the same viewpoint in the software and giving a low transparency value to the petrosal bone, the real and the virtual bones became comparable with each other, showing the hidden structures from any arbitrary point of view (**Figures 26** and **27**). Three video animations were also created with Blender (freeware, https://www.blender.org), demonstrating the main parts of the petrosal bone (https://youtu.be/0fI4oNCPTyI), the middle ear cavity (https://youtu.be/o26Ek-cHyLM) and the facial canal throughout the bone (https://youtu.be/EzfTzmeXsGc). Finally, the 3D model of the osseous inner ear together with the connected auditory ossicles were 3D-printed using the SLS technology, and the different structures were colorized with acrylic dye according to the virtual models (**Figure 28**) (Czeibert et al., 2018).

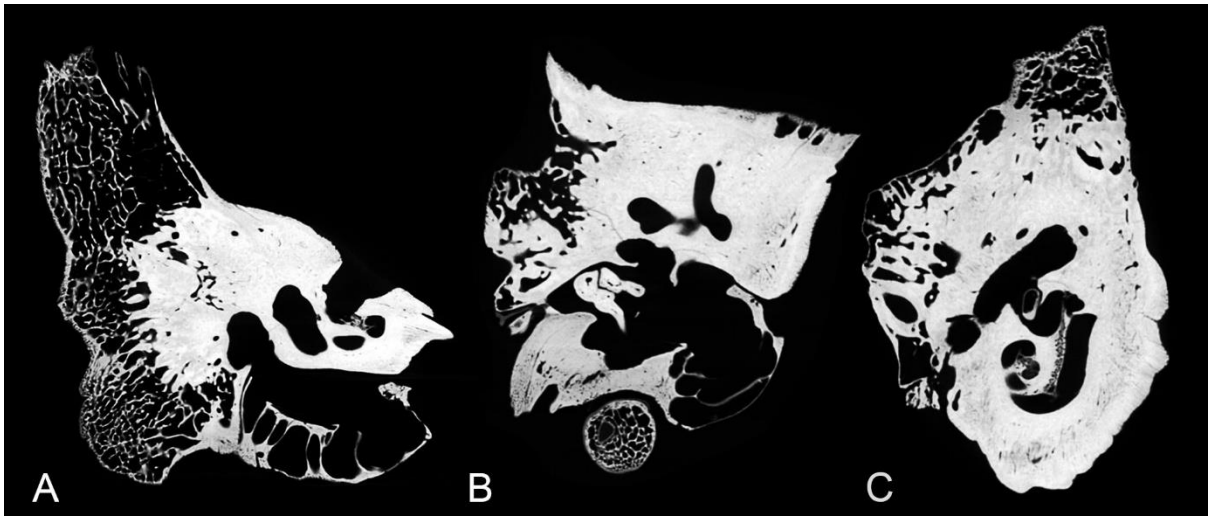

Figure 25. CT of an equine petrosal bone. Sagittal (A), transverse (B), and dorsal (C) planes.

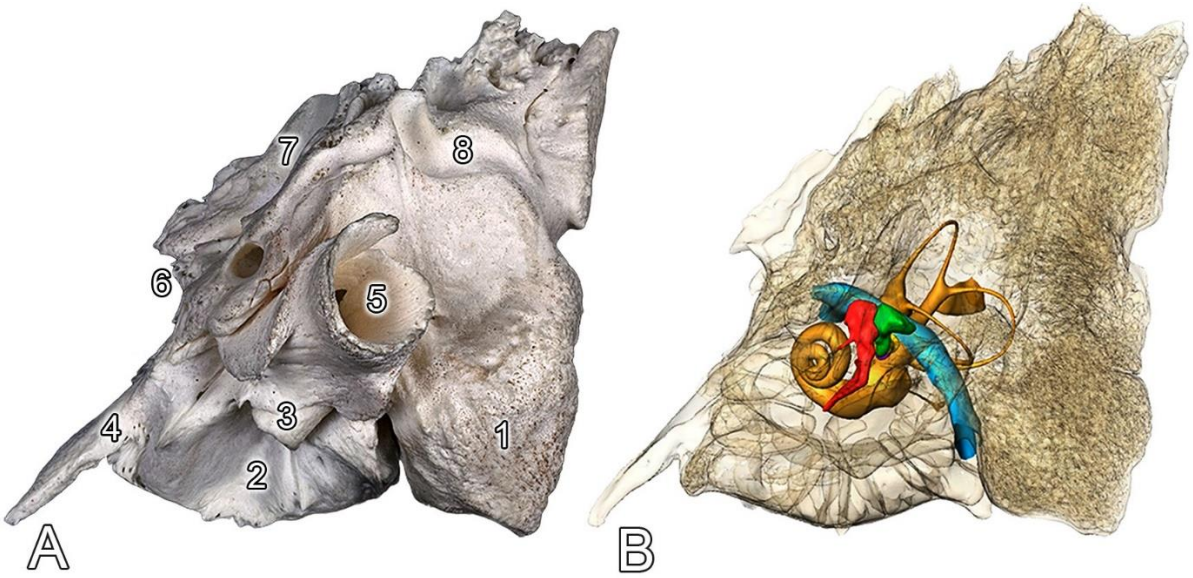

Figure 26. Equine petrosal bone, lateral view. A) Photograph. B) Semi-opaque 3D model. Coloured structures: malleus (in red), incus (in green), auris interna (in orange), canalis facialis (in blue). 1) Processus mastoideus. 2) Bulla tympanica. 3) Processus styloideus. 4) Processus muscularis. 5) Meatus acusticus externus. 6) Impressio nervi trigemini. 7) Crista partis petrosae. 8) Sulcus arteriae meningeae caudalis.

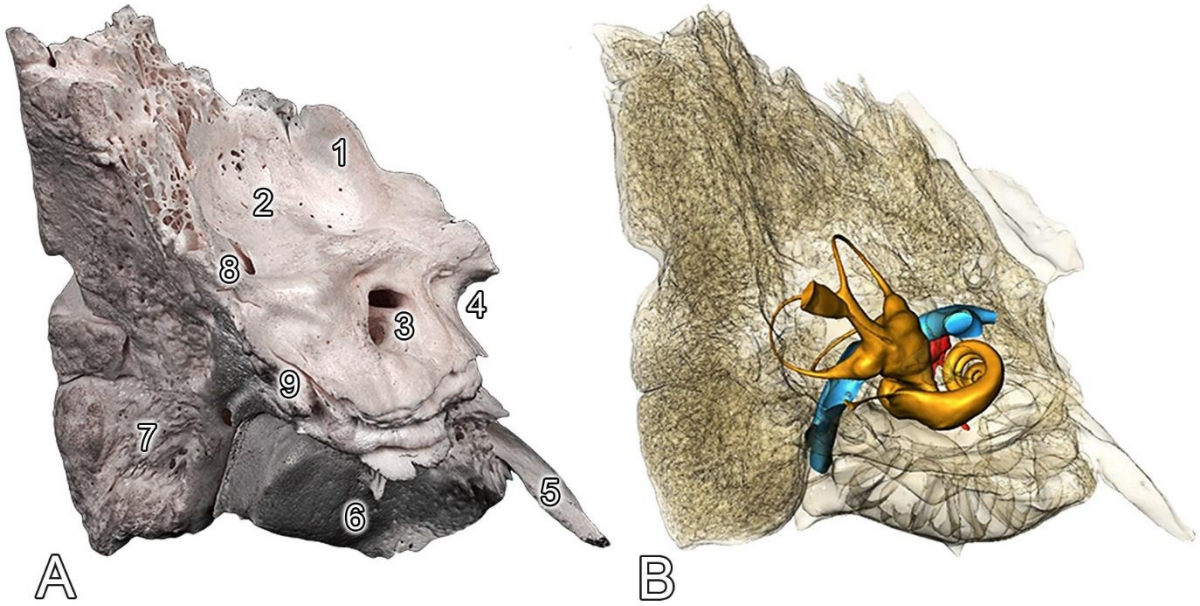

Figure 27. Equine petrosal bone, medial view. A) Photograph. B) Semi-opaque 3D model. Coloured structures: malleus (in red), auris interna (in orange), canalis facialis (in blue). 1) Crista partis petrosae. 2) Fossa cerebellaris. 3) Meatus acusticus internus. 4) Impressio nervi trigemini. 5) Processus muscularis. 6) Bulla tympanica. 7) Processus mastoideus. 8) Apertura externa aqueductus vestibuli. 9) Apertura externa canaliculi cochleae.

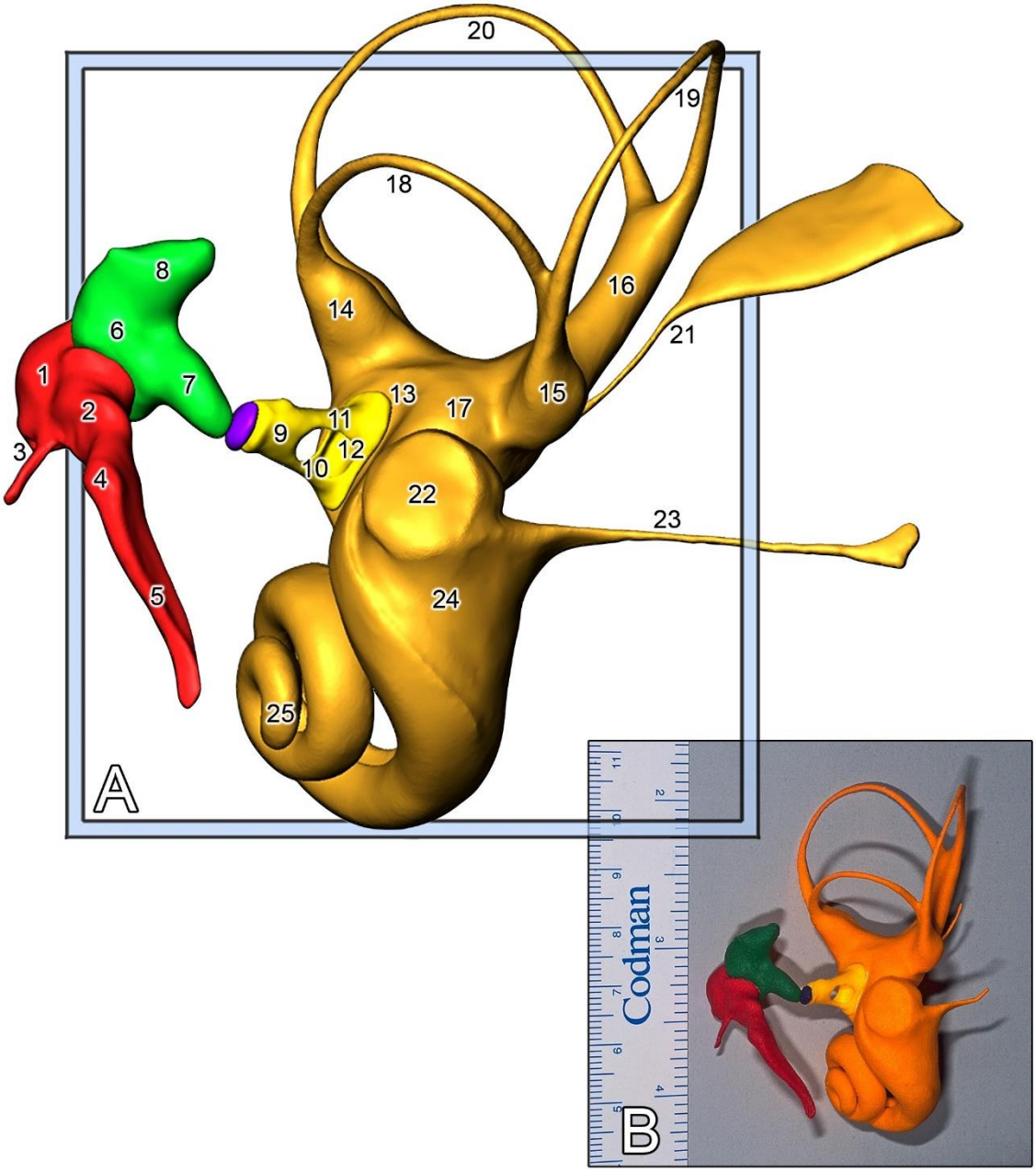

Figure 28. The auditory ossicles and the osseous inner ear of a horse, caudo-lateral view. A) Digital model. B) 3D-printed and enlarged model. Coloured structures: auris interna (in orange), malleus (in red), incus (in green), os lenticulare (in purple), stapes (in yellow). 1) Caput mallei. 2) Collum mallei. 3) Processus rostralis. 4) Processus muscularis. 5) Manubrium mallei. 6) Corpus incudis. 7) Crus longum. 8) Crus breve. 9) Caput stapedis. 10) Crus rostrale. 11) Crus caudale. 12) Basis stapedis. 13) Fenestra vestibuli (*seu:* ovalis). 14) Ampulla ossea lateralis. 15) Ampulla ossea posterior. 16) Crus osseum commune. 17) Vestibulum. 18) Canalis semicircularis lateralis. 19) Canalis semicircularis posterior. 20) Canalis semicircularis anterior. 21) Aqueductus vestibuli. 22) Fenestra cochleae (*seu:* rotunda). 23) Canaliculus cochleae. 24) Basis cochleae. 25) Cupula cochleae.

4.3.3. Study VIII: Multimodal visualisation of a feline head

We used the imaging data from our third cryosectioning study, where we obtained images from a cat head using the Dufour milling machine and data from the CT and MR scanning. First, the Canon Raw Version 2 image file (CR2) raw red, green, blue (RGB) images derived from the cryosectioning were saved in a tag image file format (TIFF), by applying the required colour corrections based on the values of the X-Rite ColorChecker passport (**Figure 7/A, B**). Thereafter, the images were imported into the Amira software, and converted into one image volume. Using the "*Align Slices*" module, the minor shifts between the individual slices were corrected. The MRI and CT image volumes were also imported into the same Amira project, and by using the "*Register Images*" module, all the three image volumes were registered to each other in the same position. Working with the "*Edit New Label Field*" module, different label fields were created: the outer contour of the head was made from the CT volume, and based on the cryosectioned image volume the blood vessels, the brain and the tumour were extracted. This enabled all the different imaging modalities to be shown in the same coordinate system based on the original transverse slices. New slices were reconstructed in the dorsal plane to demonstrate that by having a small sectioning interval (in this case it was 400 µm), a good quality multiplanar reconstruction can be created from the original volume (**Figure 29**).

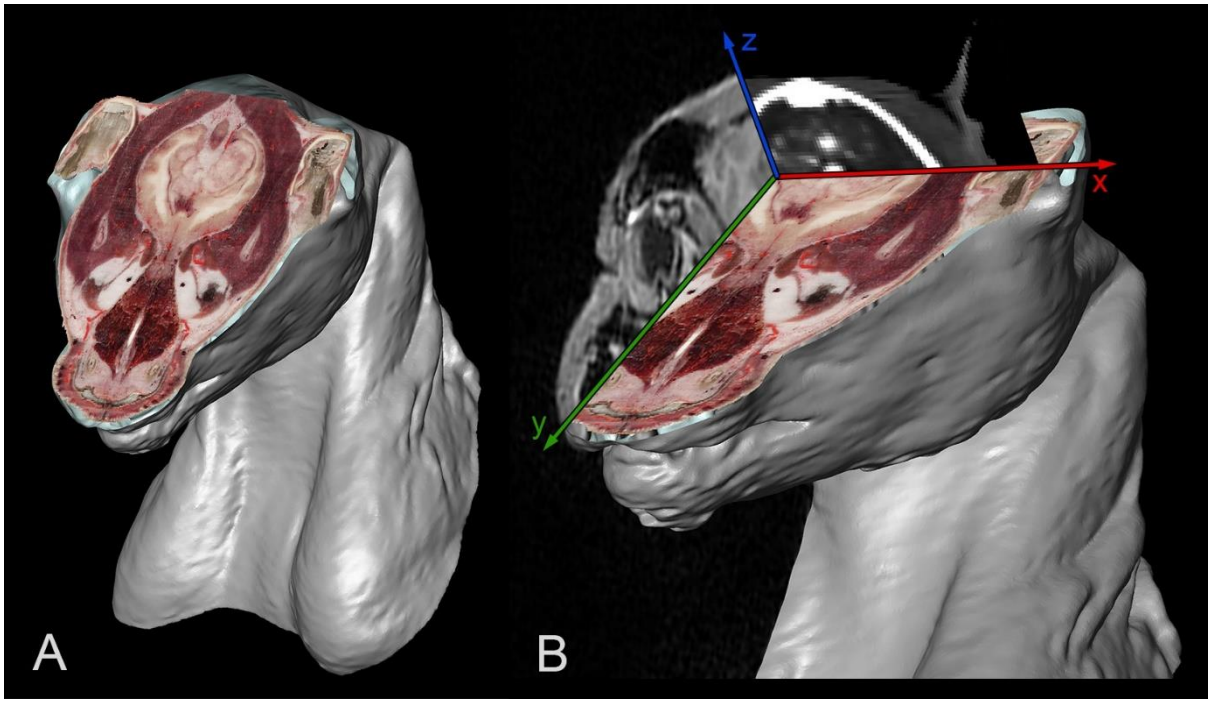

Figure 29. Multimodal reconstruction of a cat head. A) The surface model of the animal (in grey) with the cryosectioned RGB image that was reconstructed in the dorsal plane. B) Surface model of the head (in grey), cryosectioned RGB-image (in the dorsal plane), T1-weighted MR image (in the sagittal plane) and CT image (in the transverse plane).

Having the different segments from the imaging volumes also made it possible to visualise the major blood vessels of the head, as well as the intracranially located tumour (**Figures 30**). The images were also published in a flip-book, where one could turn through the pages to see the cryosections and the MR images in the neighbouring pages (Czeibert et al., 2015).

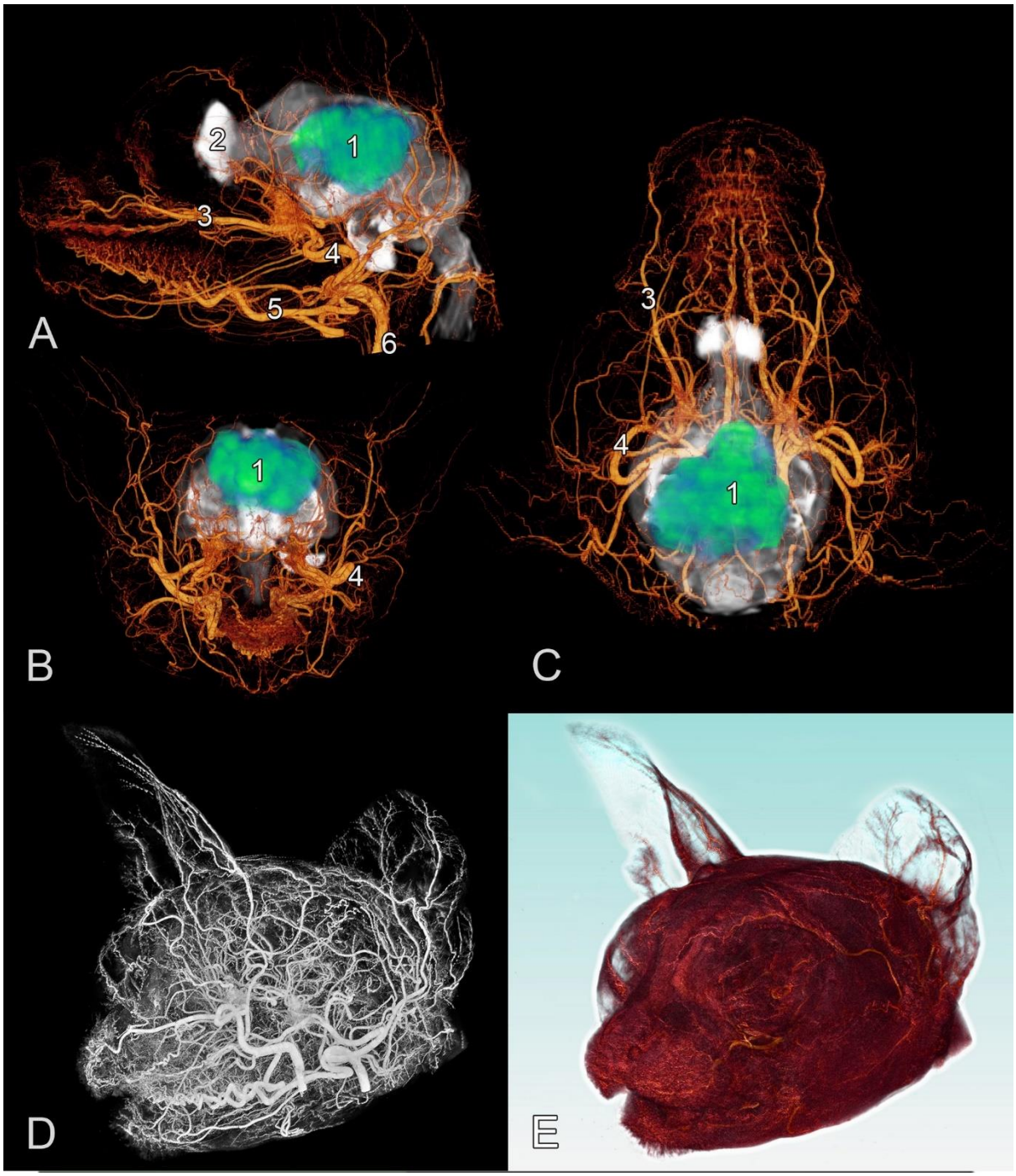

Figure 30. 3D reconstructions of a cat head. A, B, C) Showing the arteries (in orange), the tumour (in green) and the brain (in grey). A) Left lateral view. B) Rostral view. C) Dorsal view. D, E) Arteries of the head with different details, left rostro-lateral view. 1) Tumour. 2) Bulbus olfactorius. 3) A. infraorbitalis. 4) A. maxillaris. 5) A. lingualis. 6) A. carotis communis.

4.3.4. Study IX: Creating the MRI label map of a canine brain

The next imaging study was in line with that endeavour to work with various visualisation programs, and to deepen the knowledge in the field of the canine neuroanatomy (which could be used in the framework of the final cryosectioning study). This project was connected to the work of a research group at the Eötvös Loránd University (ELTE, Institute of Biology, Department of Ethology, Budapest). Since 2009, at the Department of Ethology, and as a part of the Family Dog Project of the (FDP; https://familydogproject.elte.hu), privately owned dogs have been trained to lay motionless within an MRI machine during awake functional MRI (fMRI) scanning (Andics et al., 2016, 2014; Tóth et al., 2009). To aid this fMRI analysis, a detailed and easy-to-use anatomical MRI label map of a template dog brain was created.

The reason why a brain template is essential is that the awake dog fMRI has clearly become an emerging field of comparative brain imaging, and it is currently performed in several laboratories worldwide (Andics & Miklósi, 2018; Berns et al., 2012; Bunford et al., 2017; Cook et al., 2015; Cuaya et al., 2016; Thompkins et al., 2016). The fMRI has become the primary means of non-invasively identifying the location of specific neuronal activities, e.g., in response to certain sensory stimuli or in connection with some task-driven motor activity (Cox & Savoy, 2003; Logothetis & Pfeuffer, 2004; Ulmer & Jansen, 2013). Similarities between humans and dogs regarding development, aging, and certain disorders affecting the central nervous system led researchers to focus on a deeper understanding of the canine brain (Adams et al., 2000; Cotman & Head, 2008; Head, 2013; Su et al., 1998). Various MRI-based canine brain templates have been developed, but the corresponding label maps either lack the level of detail required for an efficient fMRI analysis (Datta et al., 2012; Nitzsche et al., 2018) or they are not yet publicly available (Milne et al., 2016). There are online dog MRI brain atlases (e.g., http://vanat.cvm.umn.edu/mMRIBrain, https://www.imaios.com/en/vet-Anatomy) showing brain structures with different levels of detail are also available, but it is usually not possible to co-register them to other brain image files derived from other research groups. In recent decades, MRI templates and label maps for different animals have been created to aid the analysis of spatially normalised neuroimaging datasets for various species, e.g., rodents (Nie et al., 2013; Schwarz et al., 2006), rabbits (Muñoz-Moreno et al., 2013), sheep (Ella & Keller, 2015; Nitzsche et al., 2015), the common marmoset (Hikishima et al., 2011), dogs (Datta et al., 2012; Nitzsche et al., 2018; Tapp et al., 2006), and macaques (Adluru et al., 2012; Reveley et al., 2017; Rohlfing et al., 2012; Seidlitz et al., 2018). These animal researches and template developments gave firm scientific background and showed guidelines what kind of technical and anatomical support is necessary for the effective MRI analysis.

First, we had to select a template dog brain to our study. Imaging of the head was performed on a Philips Ingenia 3T MR machine (Philips Medical Systems, Best, The Netherlands), with a Philips SENSE Flex Medium coil using a 3D Turbo Field Echo sequence (TR = 9.85 ms, TE = 4.6 ms, with an isotropic resolution of 1 mm). T1-weighted images were obtained from 22 dogs who were trained to lay motionless during scanning (Andics et al., 2014) (**Figure 31**). Among the 22 dogs, there were 8 golden retrievers, 7 border collies, 1 Labrador retriever, 1 German shepherd dog, 1 Hungarian vizsla, 1 Cairn terrier, 1 cocker spaniel, 1 labradoodle and 1 Chinese crested dog (aged between 1 and 12 years). None of the dogs showed behavioural problems or neurological symptoms. All husbandry and experimental procedures were approved by the institutional animal care and ethics committee and by the Government Office of Pest County Directorate of Food Chain Safety and Animal Health (XIV-I-001/520-4/2012), and were conducted in accordance with relevant guidelines and regulations. Images were exported in Neuroimaging Informatics Technology Initiative (NIfTI) format and were evaluated with MRIcron (freeware, http://people.cas.sc.edu/rorden/mricron/index.html) and Amira. A detailed qualitative evaluation of the shape, size, gyral patterns (Carreira & Ferreira, 2015a, 2015b; Evans & de Lahunta, 2012; Kawamura & Naito, 1978) and ventricular anatomy was performed, and the 2D NIfTI-image series and 3D surface reconstructions generated from the brain MRIs were assessed to select that individual within this sample that showed the most typical mesaticephalic brain conformation (Hussein et al., 2012; Milne et al., 2016), with no apparent structural disorders or unusual anatomical variations. After this analysis, the brain of a 7.5-year-old male golden retriever was chosen as a template for labelling.

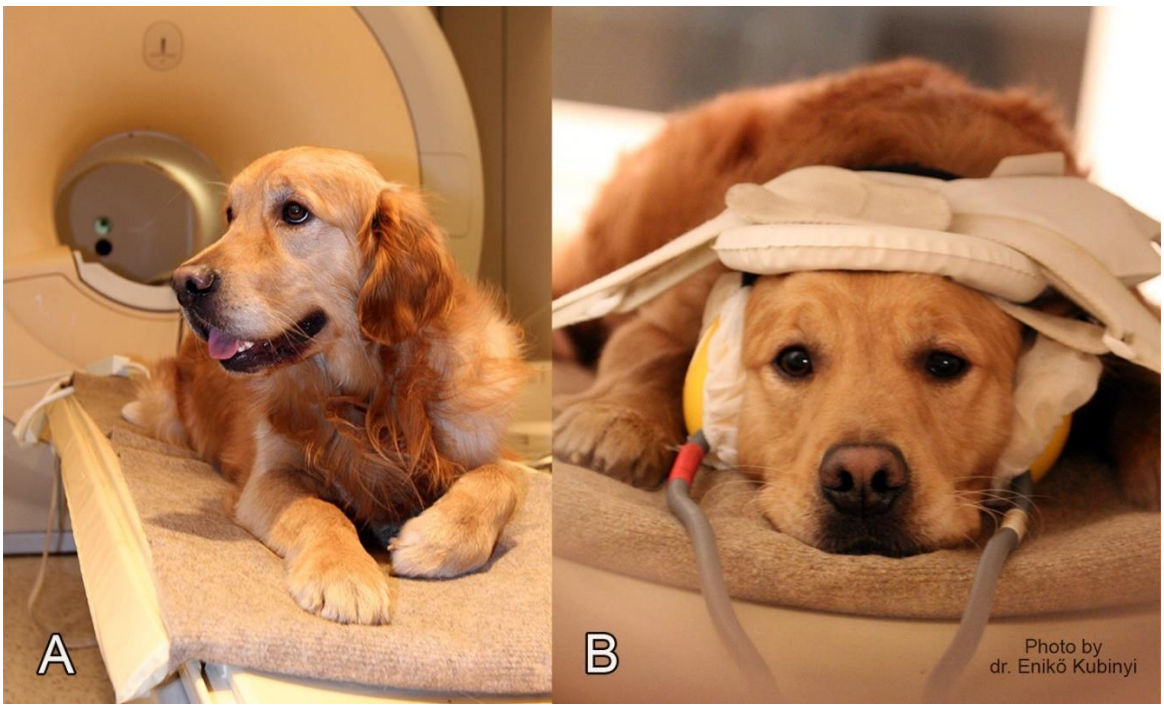

Figure 31. A dog participating in an awake fMRI. A) Before scanning. B) During scanning.

To obtain a higher resolution scan from this individual brain, another MRI examination was performed on the selected dog in an awake state (using the same Philips Ingenia 3T MR machine, with T1-weighted structural imaging, 0.45×0.45×0.5 mm voxel size and having 352 transverse slices). The image volume was imported to Amira. First, the main axes were set. The horizontal (longitudinal) axis was defined as the line connecting the rostral and caudal commissures, where the zero coordinate was aligned with the rostral commissure (similar to the Montreal Neurological Institute's (MNI) coordinate system). The vertical axis was identified with the midsagittal plane. Based on these axes, the transverse, sagittal and dorsal planes were set. Next, the volume was resampled and the field of view was specified so that it would contain the neurocranium and the adjacent tissues. Finally, the origin was set to the rostral commissure with the "*Reorient images/Set origin to Xhairs*" module of the 12th version of the Matrix Laboratory's (MATLAB) Statistical Parametric Mapping (SPM) image processing and analysis software (SPM12, https://www.fil.ion.ucl.ac.uk/spm/software/spm12). A 3D surface model of the template dog brain was also generated with Amira (**Figure 32**).

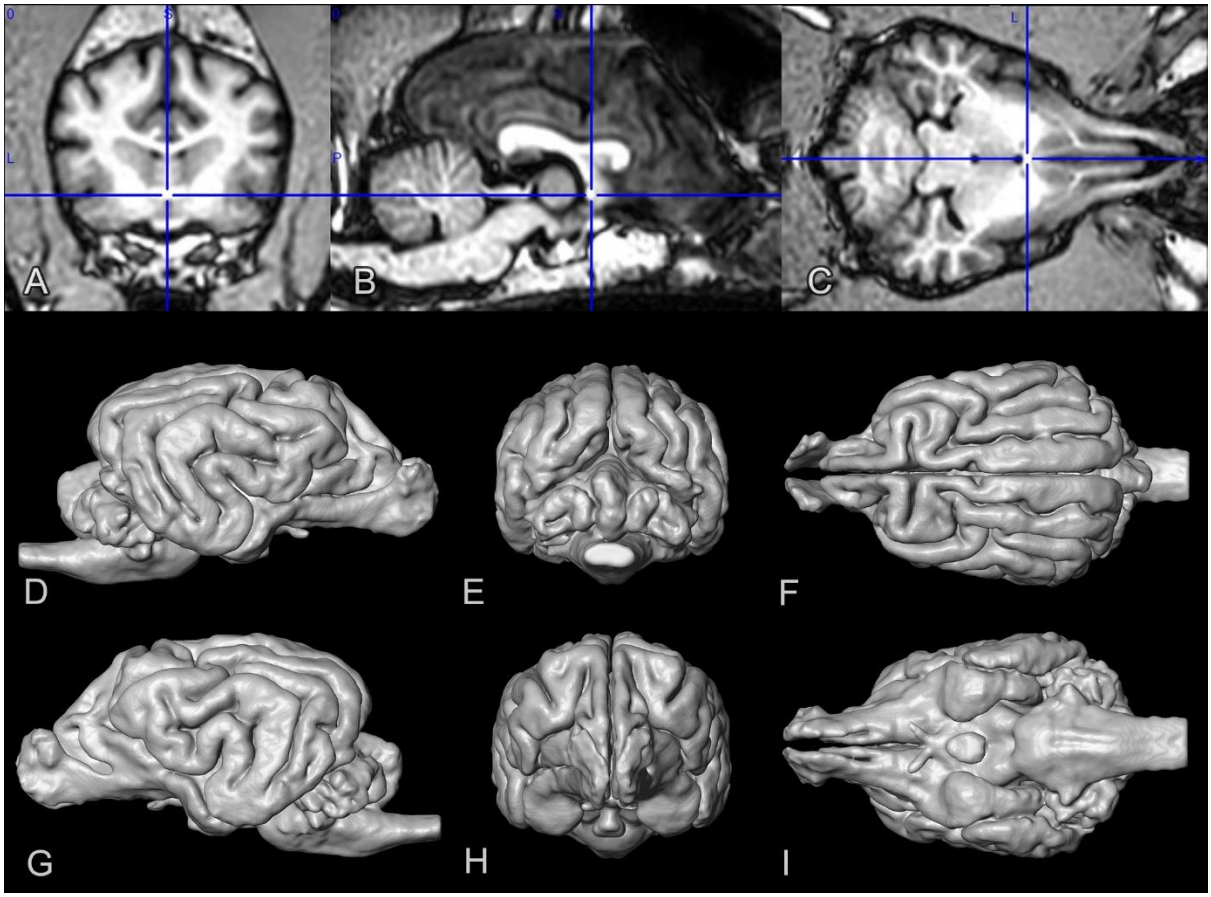

Figure 32. The template dog brain. A) Transverse plane. B) Midsagittal plane. C) Dorsal plane. D) Right lateral view. E) Caudal view. F) Dorsal view. G) Left lateral view. H) Rostral view. I) Ventral view. A, B, C) The blue crosshair positioned at the origin of the coordinate system (at the rostral commissure) in the MR images. D, E, F, G, H, I) 3D reconstructions.

Individual labels were created to highlight the main gyri and the area of the individual brain template. Labels were made with ITK Snap (freeware, http://www.itksnap.org), defining 86 different masks with "*Label Editor*," distinguishing between the left and right sides in the case of symmetrical structures (**Table 1**). Segmentation was performed manually by checking and refining the result in the three main orthogonal planes. The final label file was exported in NIfTI format, and to use the same RGB colours, two lookup table (LUT) files were created as a support to the MRIcron visualisation.

Table 1. Labelled structures on the individual template file, indicating the number (Nº) and colour (C) according to the LUT file and region. L/R indicates that separate left (L) and right (R) label files were created for a given structure.

Nº	C	region
1		encephalon
2		gyrus frontalis L
3		gyrus frontalis R
4		gyrus proreus L
5		gyrus proreus R
6		gyrus compositus rostralis L
7		gyrus compositus rostralis R
8		gyrus precruciatus L
9		gyrus precruciatus R
10		gyrus postcruciatus L
11		gyrus postcruciatus R
12		gyrus marginalis L
13		gyrus marginalis R
14		gyrus ectomarginalis L
15		gyrus ectomarginalis R
16		gyrus occipitalis L
17		gyrus occipitalis R
18		gyrus suprasylvius rostralis L
19		gyrus suprasylvius rostralis R
20		gyrus suprasylvius medius L

Nº	C	region
21		gyrus suprasylvius medius R
22		gyrus suprasylvius caudalis L
23		gyrus suprasylvius caudalis R
24		gyrus ectosylvius rostralis L
25		gyrus ectosylvius rostralis R
26		gyrus ectosylvius medius L
27		gyrus ectosylvius medius R
28		gyrus ectosylvius caudalis L
29		gyrus ectosylvius caudalis R
30		gyrus sylvius rostralis L
31		gyrus sylvius rostralis R
32		gyrus sylvius caudalis L
33		gyrus sylvius caudalis R
34		gyrus compositus caudalis L
35		gyrus compositus caudalis R
36		gyrus rectus L
37		gyrus rectus R
38		gyrus genualis L
39		gyrus genualis R
40		area subcallosa L

Table 1. (*continued*) Labelled structures on the individual template file, indicating the number (Nº) and colour (C) according to the LUT file and region. L/R indicates that separate left (L) and right (R) label files were created for a given structure.

Nº	C	region
41		area subcallosa R
42		gyrus cinguli L
43		gyrus cinguli R
44		gyrus presplenialis L
45		gyrus presplenialis R
46		gyrus splenialis L
47		gyrus splenialis R
48		gyrus parahippocampalis L
49		gyrus parahippocampalis R
50		hippocampus L
51		hippocampus R
52		lobus piriformis L
53		lobus piriformis R
54		tuberculum olfactorium L
55		tuberculum olfactorium R
56		gyrus diagonalis L
57		gyrus diagonalis R
58		gyrus paraterminalis L
59		gyrus paraterminalis R
60		gyrus olfactorius lateralis L
61		gyrus olfactorius lateralis R
62		thalamus L
63		thalamus R

Nº	C	region
64		bulbus olfactorius L
65		bulbus olfactorius R
66		nucleus caudatus L
67		nucleus caudatus R
68		insular cortex L
69		insular cortex R
70		hypophysis
71		vermis cerebelli
72		pons
73		medulla oblongata
74		medulla spinalis
75		mesencephalon
76		diencephalon
77		nervus opticus
78		hemispherium cerebelli L
79		hemispherium cerebelli R
80		commissura rostralis
81		pedunculus olfactorius L
82		pedunculus olfactorius R
83		area septalis L
84		area septalis R
85		amygdala L
86		amygdala R

Our individual dog brain template was also compared to an average-based template that was recently published (Nitzsche et al., 2018), in order to check the correspondence of the individually selected brain template to the averaged template. The latter template was created by averaging 16 dog brains and using T2-weighted imaging. Our individual template was obtained from one dog using T1-weighted imaging; therefore, the contrast (smoothed versus

sharp) and the imaging modalities (T2-weighted versus T1-weighted) were different. Thus, a computer-paired visual matching procedure was used to decide whether the main gyri and sulci of the individual-based and the average-based templates had the same location. The first phase of the assessment was to use the average-based template as the primary dataset in Amira and set the individual template as the overlay data in the software's multiplanar viewer. Next, the overlay volume was registered to the primary dataset. Registration steps included rigid and non-rigid transformations. The rigid transformations were rotation and translation, and the non-rigid transformations were isoscaling, anisoscaling and shearing. These transformations are integrated check box options in the Amira software (without further settings or the possibility to check the degree of freedom or their parameters); thus, all of the check boxes were left as marked by default. The cost function used for the registration was "*Correlation*". Additionally, as a control, a "*Normalized Mutual Information*" registration was also performed on the same dataset to see whether it made any difference, but overlaying the two result files showed no disparity. Fitting was initially evaluated with merging the images and checking the position of the ventricular systems based on its signal intensity (**Figure 33**).

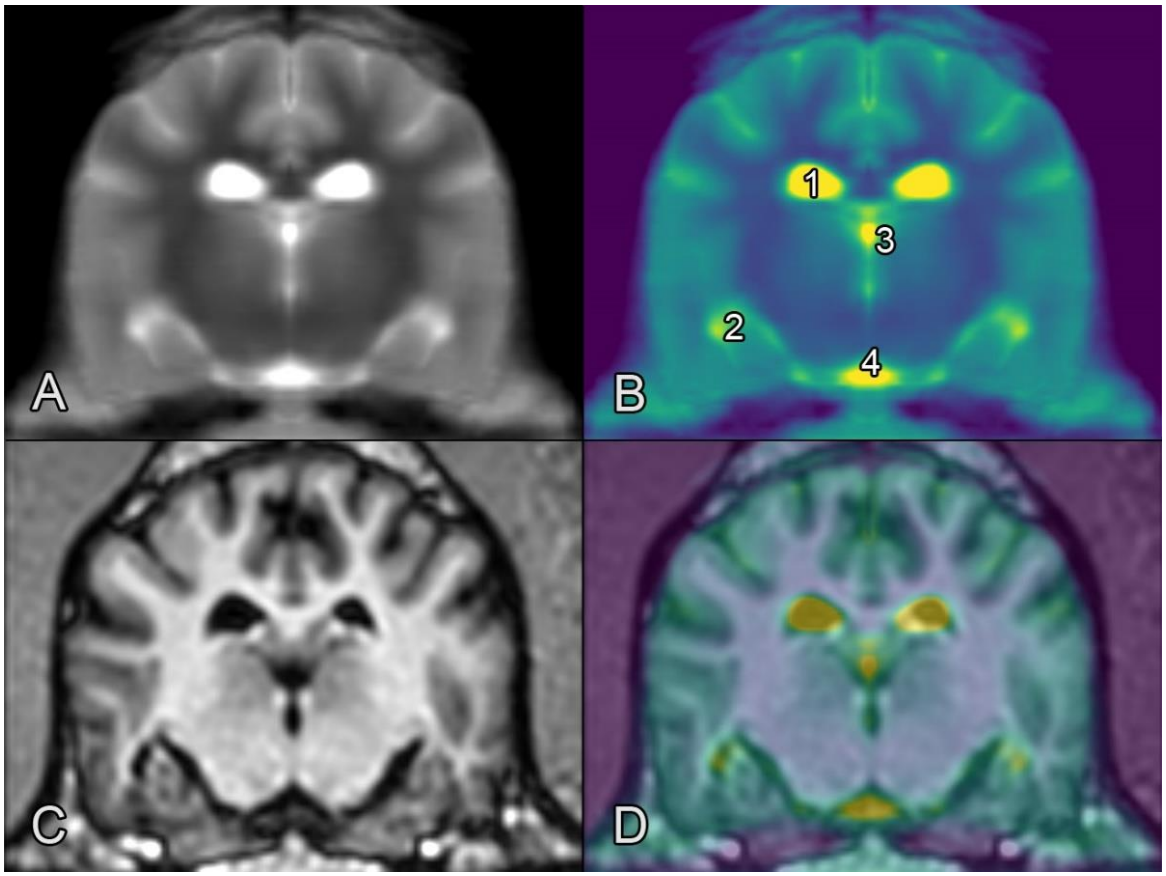

Figure 33. Transverse MR scan at the level of the dorsum sellae. A) Average-based dog brain template (in grey). B) The colorized version of image "A". C) Individual dog template (in grey). D) Co-registered brains, with 50% opacity. 1) Ventriculus lateralis, pars centralis. 2) Ventriculus lateralis, cornu temporale. 3) Ventriculus tertius. 4) Cisterna interpeduncularis.

In the second phase of the assessment, an "*Edit New Label Field*" module was added to both of the volumes in the Amira, and cerebrospinal fluid-filled spaces of the average-based brain template (extending also into the sulci) were selected in the segmentation editor. The outer (cortical) contour was followed during the segmentation of the golden retriever brain. Using the "*Generate Surface*" module, surface reconstructions from both of the selected template label fields were created. A non-quantitative assessment of the two co-registered models was also made to verify their post-normalisation alignment.

The boundaries between the rostral, middle, and caudal parts of a gyrus (as in the case of the suprasylvian and ectosylvian gyri) were drawn based on a subjective decision, regarding the inclination of the gyral arch and the surface impression of the major blood vessels originating from the middle cerebral artery and extending from the pseudosylvian fissure in the caudo-dorsal and rostro-dorsal directions. The diencephalo-mesencephalic border was marked behind the line connecting the mammillary bodies to the caudal commissure. Mesencephalo-pontine and ponto-medullary transitions were marked before and behind the location of the visible ventral pontine elevation (at the site of the transverse pontine fibres). Cerebral gyri were selected to comprise both the grey and the white matter of a gyrus, extending to the deepest point of the adjacent sulci. Since there were no clearly established borders on the medial frontal area by grooves, and sulci on the medio-frontal area tend to be inconsistent in their appearance, the gyrus precruciatus, gyrus frontalis, gyrus rectus, rostral part of the gyrus cinguli, and the gyrus genualis were highlighted based on subjective assessment.

As a result of this work, an individual-based dog brain template was selected, and 86 labels were created to highlight the major cortical and subcortical structures (listed in **Table 1** and sample images shown in **Figures 34** and **35**). The template and label files are publicly available on Figshare (https://figshare.com/s/628cbf7d4210271ffe70). The labels included all the cerebral gyri both on the lateral and medial sides, the major subcortical structures (e.g., thalamus, caudate nucleus, amygdala, and hippocampus), and the main parts of the brainstem (diencephalon, mesencephalon, pons, and medulla oblongata). The label "encephalon" was used to cover most of the parts of the white matter (e.g., centrum semiovale and capsula interna) and those regions where the subcortical nuclei could not be reliably distinguished in the image (e.g., claustrum, putamen, pallidum); this was also the reason why a separate white matter mask was not created. In the case of the cerebellum, the vermis and the two hemispheres were labelled separately. The term 'gyrus' was applied purposely to refer to on an entire neocortical convolution, as it makes easier to describe the location of an fMRI activity signal. This is the reason why in the label masks both the grey and the white matters of an individual convolution are colorized and named together.

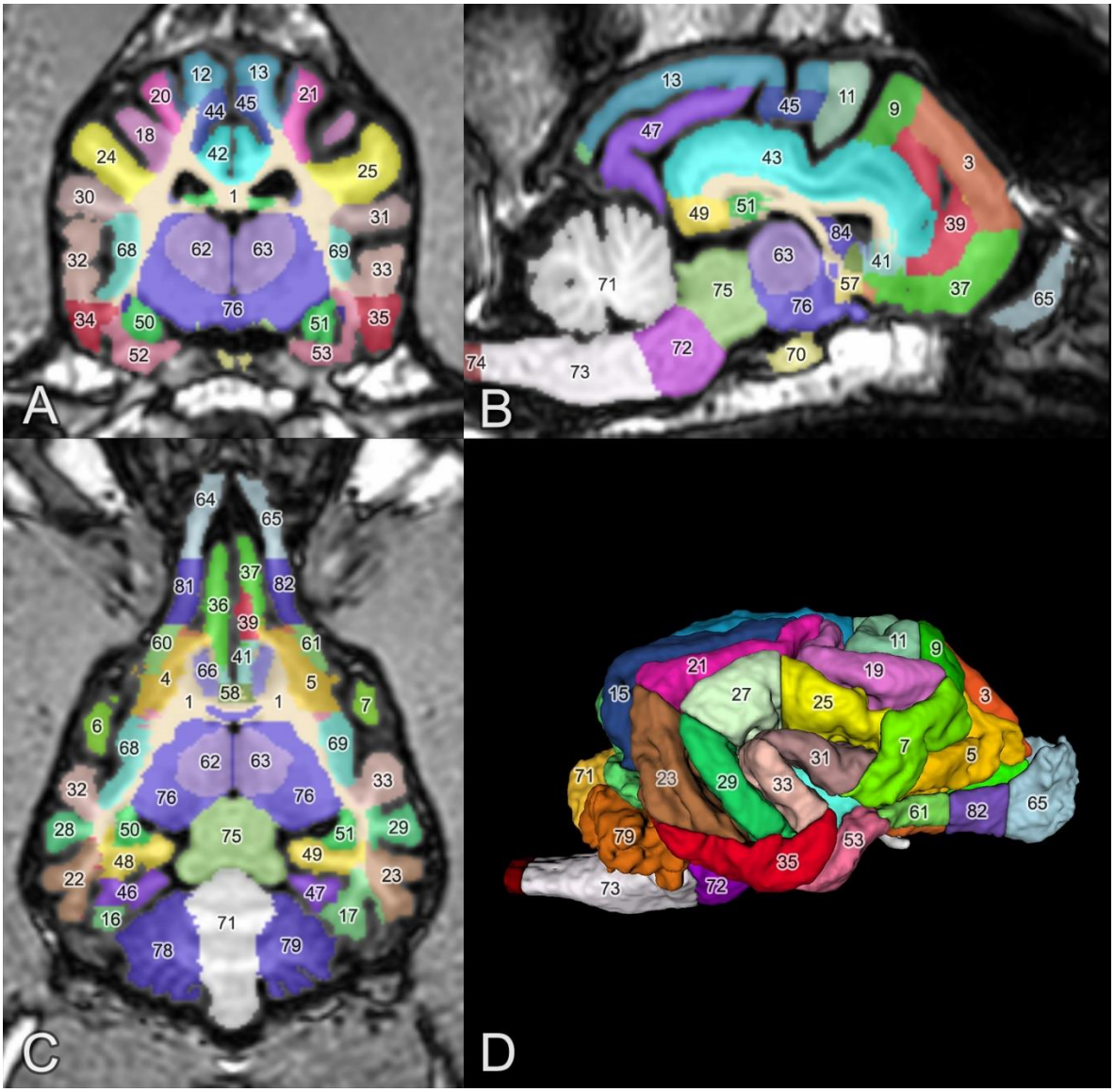

Figure 34. Overlay of labels on an individual dog brain template with 50% opacity (for reference of the numbers, see **Table 1**). A) Transverse plane. B) Sagittal plane. C) Dorsal plane. D) 3D surface view of the labels from the right lateral aspect.

The surface reconstructions of the average-based template (Nitzsche et al., 2018) and this individual-based template (Czeibert et al., 2019a) show the sulci and the gyri of the two brains. When the two 3D models were co-registered, different sulci (or subarachnoid spaces) of the average-based template were visible in the corresponding locations on the T2-weighted MR images, where the sulci of the individual-based template were located on the T1-weighted scans (certainly, individual differences in the length of sulci were present). We focused on verifying the location of the specific sulci that define the main gyri of the brain, namely, the fissura pseudosylvia, fissura longitudinalis cerebri, sulcus ectosylvius (rostral, middle, and caudal parts), sulcus suprasylvius (rostral, middle, and caudal parts), sulcus cruciatus, sulcus coronalis, sulcus marginalis, sulcus ectomarginalis and sulcus presylvius (**Figure 36**).

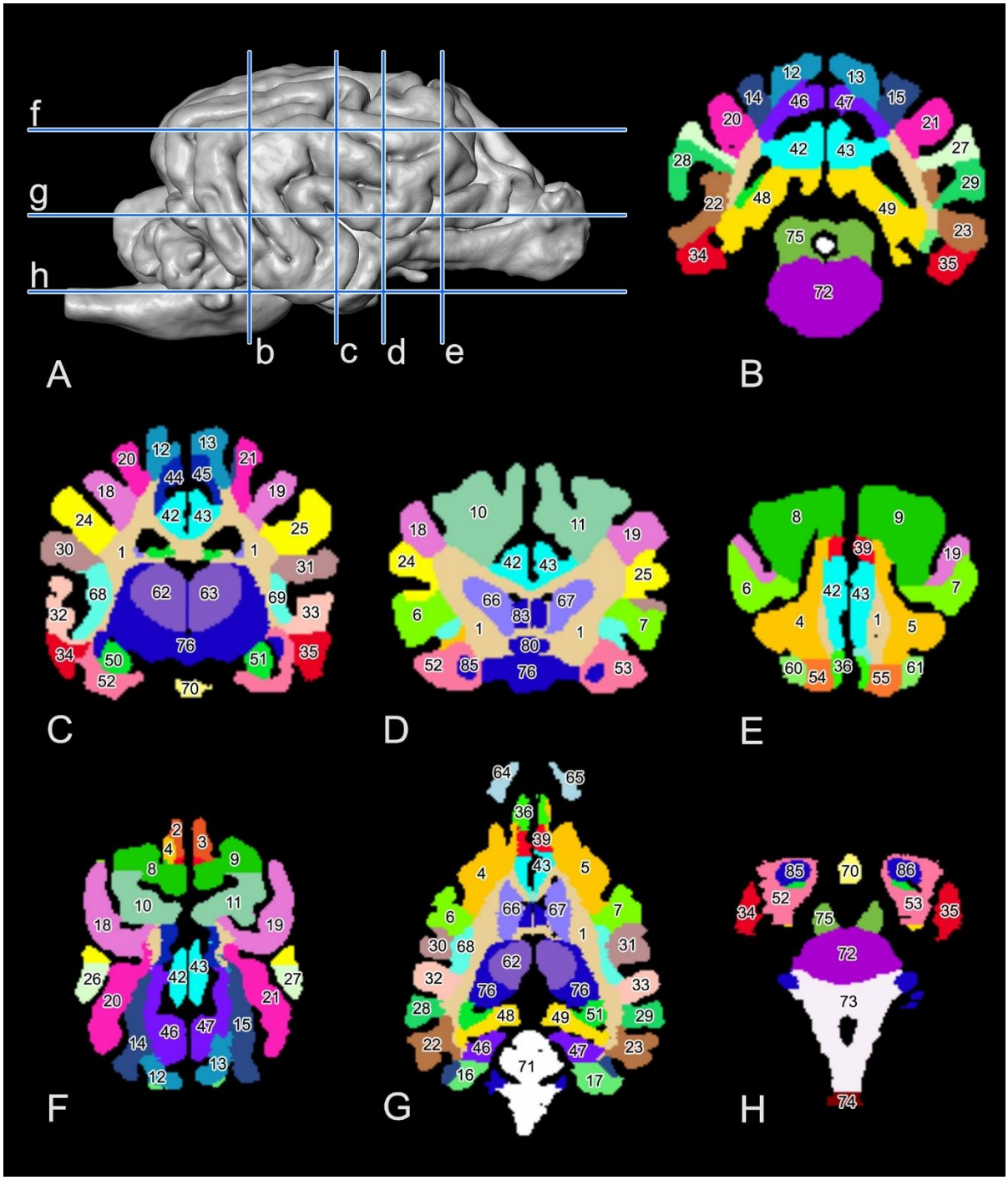

Figure 35. The individual canine brain label map on different levels of the sample images (for reference of the numbers, see **Table 1**). The same letters (with upper and lower case) in the image indicate the same level of section. A) 3D model of the brain, right lateral view. B, C, D, E) Sections in the transverse plane. F, G, H) Sections in the dorsal plane.

A comparison of the co-registered 3D models clearly indicated that our individual template brain sufficiently matched the average-based template created by Nitzsche et al. (2018), that is, we could not identify any multivoxel clusters that belonged to different anatomical structures in the two template images after the co-registration.

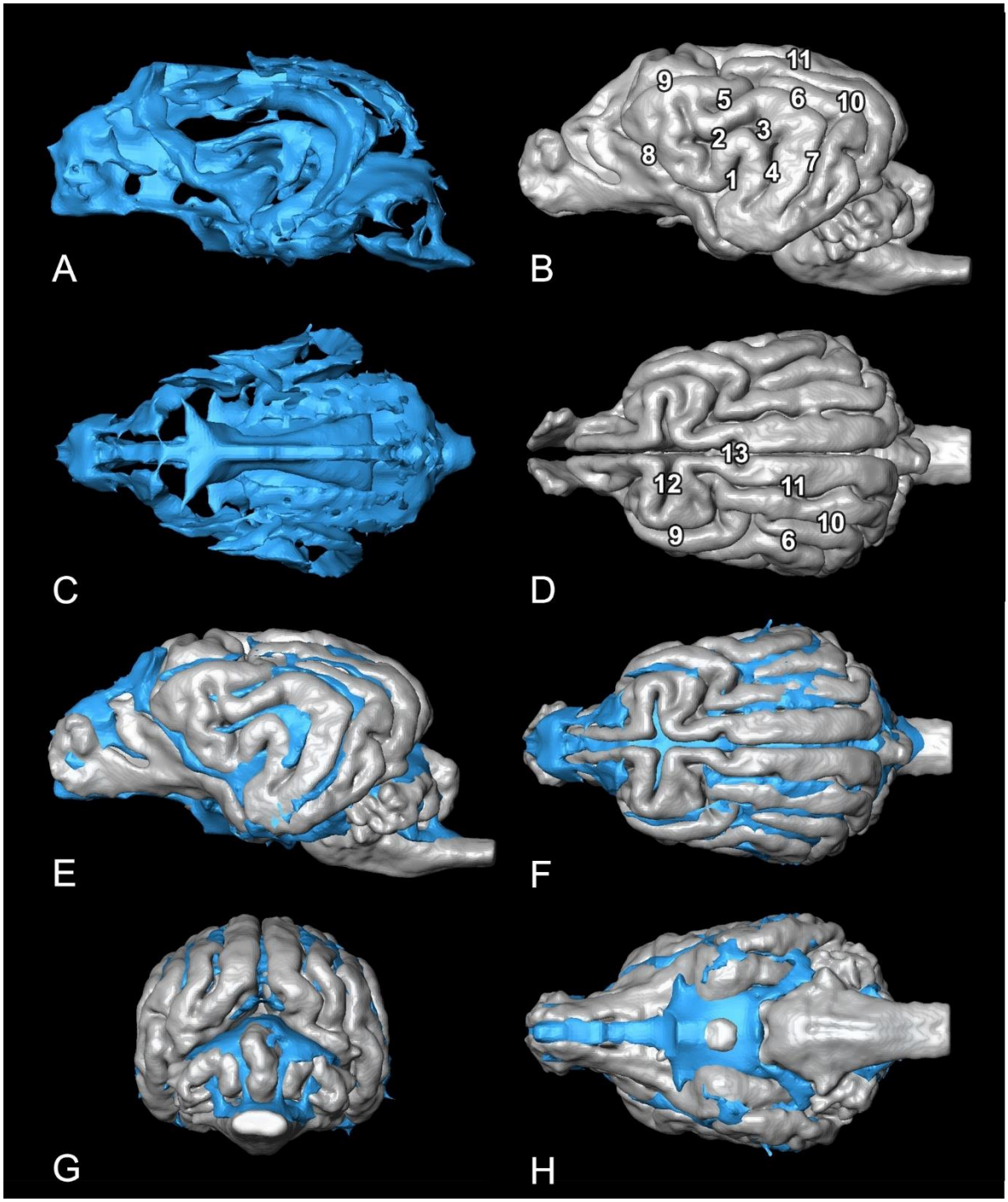

Figure 36. Comparing the average-based T2-weighted brain template (liquor cerebrospinalis filled regions modelled in blue) with the T1-weighted individual template brain (surface model of the brain in grey) in the same coordinate system. Separate (A, B, C, D) and co-registered 3D models (E, F, G, H) are presented to show the location of the sulci. A, B, E) Left lateral view. C, D, F) Dorsal view. G) Caudal view. H) Ventral view. 1) Fissura pseudosylvia. 2) Sulcus ectosylvius rostralis. 3) Sulcus ectosylvius medius. 4) Sulcus ectosylvius caudalis. 5) Sulcus suprasylvius rostralis. 6) Sulcus suprasylvius medius. 7) Sulcus suprasylvius caudalis. 8) Sulcus presylvius. 9) Sulcus coronalis. 10) Sulcus ectomarginalis. 11) Sulcus marginalis. 12) Sulcus cruciatus. 13) Fissura longitudinalis cerebri.

A known difficulty is that the literature contains different descriptions of the canine brain areas regarding their names, placement and boundaries. Consequently, although the gyri placements in our individual-based label map were determined according to the major anatomy textbooks (Constantinescu & Schaller, 2011; Evans & de Lahunta, 2012; Nickel et al., 2003; Singh, 2018; Uemura, 2015), the lack of clear definitions regarding the end of a gyrus resulted in subjective markings. Furthermore, the nomenclature of the sulci and gyri is not consistent across the different textbooks. For example, the gyrus suprasylvius (Evans & de Lahunta, 2012) is referred to as the gyrus ectomarginalis or gyrus ectosagittalis elsewhere (Constantinescu & Schaller, 2011); the gyrus postcruciatus (Constantinescu & Schaller, 2011; Evans & de Lahunta, 2012; Nickel et al., 2003) is referred to as the gyrus sygmoideus posterior (Adrianov & Mering, 2010; Palazzi, 2011); and the gyrus marginalis (Evans & de Lahunta, 2012; Nickel et al., 2003) is referred to as the gyrus lateralis (Palazzi, 2011). This inconsistent naming is an additional reason for differences. Finally, our individual-based label map contains no lobar distinctions. In fact, only gyri are highlighted because different textbooks define the main lobes of the brain differently. For example, some include the postcruciate gyrus in the frontal lobe (Thomson & Hahn, 2012; Uemura, 2015) and others do not (Constantinescu & Schaller, 2011; Nickel et al., 2003; Schmidt & Kramer, 2015; Singh, 2018). There is also a discrepancy in how long the occipital lobe is described to extend toward the rostral and ventral directions (Nickel et al., 2003; Singh, 2018; Thomson & Hahn, 2012; Uemura, 2015); thus, the parieto-occipital and temporo-occipital boundaries are also not well identified in dogs.

It should be noticed that the individual gyral patterns can be different among the individual specimens, for example due to the variations in the depth, form and length of a given groove on the cerebral surface or because of differences in the shape of the olfactory bulbs related to the various canine head shapes. This means that the shape of a gyrus cannot be expected to be exactly the same in the two images, but the primary aim of this label map was to serve as a guide for a quick basic identification tool, after which a more precise individual classification can be completed based on the given MR dataset. In contrast to human brains, dog brains highly differ in relation to the head shape (brachy-, mesati-, or dolichocephalic). At present, this diversity has been considered in only one study (Milne et al., 2016), but the brain templates used in the study contained only a few selected structures (brain as a whole, hippocampal formation, caudate nuclei, ventricular system), and the templates are not publicly available. Several neuroimaging software packages (e.g., SPM, FSL, BrainVoyager, 3D Slicer, MRIcron) contain an algorithm that automatically extracts data about the scanned human brain and normalises it to a template brain. Clearly, there is a need for deep learning algorithms (Akkus et al., 2017) for brain shape-specific templates that could automate this step for canine studies, in addition to the automatic normalisation of an individual brain to a selected template.

In conclusion of this visualisation study, an individual-based MRI label map was created for the identification of macroscopic anatomical structures of a canine brain. The main features of this brain template were as follows: (a) it provided more detailed labelling by marking 86 labels representing cortical and subcortical structures [compared to 39 labels (Datta et al., 2012), 5 labels (Milne et al., 2016) and 26 labels (Nitzsche et al., 2018)]; (b) co-registration to the latest published average-based template (Nitzsche et al., 2018) proved that the localisation of the gyri almost exactly overlapped between the two volumes, and thus the region identified with the individual-based label map is very likely associated with the same area on the average-based brain map; (c) it is compatible with freeware and commercial neuroimaging software packages (e.g., MRIcron, MRIcroGL, ITK Snap); (d) it defined a coordinate system similar to the Talairach and MNI templates. Notably, the template is derived only from one individual dog, contrary to other studies that used average-based templates from different breeds (Datta et al., 2012; Nitzsche et al., 2018) or average-based templates that were created based on different brain types (Milne et al., 2016). Nevertheless, a comparison between our individual-based label map and an average-based data set demonstrated a good fitting.

4.3.5. Conclusion of the pilot visualisation studies

The four visualisation studies gave adequate knowledge about the use of different software packages which are designed to process various image types. First, the 3D modelling work was studied during the digitalization of a canine osseo-vascular corrosion cast and an equine petrosal bone. Then the co-registration and multimodal visualisation were practised with a cryosectioned image volume obtained from a cat head together with its corresponding structural imaging data. Lastly, the creation of an MRI label map for a template dog brain gave another perspective, and it provided a comparable neuroanatomical data for the final study.

In this way, our initial question regarding the image processing was answered:

- What **software** should be used for volume generation, co-registration of the different imaging modalities and creating 3D models?
    - For visualisation and modelling purposes the Thermo Scientific Amira (as a commercial program) or the 3D Slicer (as a freeware alternative) could be used, while refinement of the STL models can be done effectively with the Autodesk MeshMixer and the Blender (both of them freeware) software.

4.4. Final study on a beagle head

4.4.1. Subject

Based on the evaluation of the pilot cryosectioning and visualisation studies, we could initiate the main project. To ensure that our results would be comparable with other studies that show normal anatomical variations (Palazzi, 2011; Park et al., 2014) and to be in accordance with previous widely accepted laboratory studies, we chose to use the beagle breed as a model animal for our study in accordance with the replacement, reduction, refinement (3R) principles (Griffin et al., 2014). The animal was obtained from an official research company (National Research Institute for Radiobiology and Radiohygiene, Department of Radiobiology, Division of Animal Experiments and Experimental Animal House (NNK SSFO), Budapest). The subject, a healthy, two-year-old female beagle dog, weighing 13.5 kg, was vaccinated and treated against parasites according to the standard veterinary program. The research was performed in accordance with international guidelines (National Research Council, 2011). All husbandry and experimental procedures were approved by the Institutional Ethics Committee and the Hungarian Directorate for Food Chain Safety and Animal Health (PEI/001/956-4/2013).

4.4.2. Imaging protocol

The MR imaging was obtained using a 3T Magnetom TIM Trio whole-body MRI scanner (Siemens AG, Erlangen, Germany) with a 12-channel phased array head coil. Under the same anaesthetic episode and immediately following the MRI, CT scans were obtained using a Siemens Somatom Perspective 128 slice CT (Siemens AG, Erlangen, Germany). The animal was placed in dorsal recumbency during the MR and CT procedures. Transverse slices (which in human MRI terminology correspond to coronal slices) were oriented perpendicular to the defined axis of the brain, which was set through the rostral and caudal commissures. To avoid any unintentional movements during general anaesthesia, and to ensure that both the MR and CT examination took place with the animal in the same position (both antemortem and postmortem), the dog was placed into a double plastic tube, which fixed the position of the body and the head separately. A system was created using plastic screws to hold the head fixed at the zygomatic arch on both sides and at the nuchal region. The holding device was checked for radiopacity and MR compatibility to avoid any artefacts during scanning. The anaesthesia premedication was 6 ml of propofol administered intravenously (Fresenius Kabi, Neufahrn bei Freising, Germany; Propofol 1% MCT/LCT Fresenius emulsion for injection, 10 mg/ml) via the right cephalic vein. After intubation, inhalational anaesthesia with 2.5 volume concentration (%V/V) isoflurane (IsoFlo, Abbott) was performed.

The MR scanning was accomplished first, during which the following sequences were obtained: T2-weighted sequence in the sagittal plane (TR = 6000 ms, TE = 90 ms, slice thickness = 2 mm, FOV = 96×160 mm^2 and a 192×320 matrix with a voxel size of 0.5×0.5×2 mm); T2-weighted imaging in the transverse plane (TR = 10342 ms, TE = 90 ms, slice thickness = 2 mm, FOV = 96×160 mm^2 and a 192×320 matrix with a voxel size of 0.5×0.5×2 mm); 3D T2-SPACE sequence in the transverse plane (TR = 1000 ms, TE = 89 ms, slice thickness = 0.5 mm, FOV = 160×160 mm^2 and a 324×320 matrix with a voxel size of 0.5×0.5×0.5 mm); and T1-weighted imaging in the transverse plane (TR = 300 ms, TE = 2.8 ms, slice thickness = 3 mm, FOV = 160×160 mm^2 and a 320×320 matrix with a voxel size of 0.5×0.5×3 mm). After the native scans, dynamic contrast-enhanced MR angiography was also performed by administering 3 ml of gadobutrol (Gadovist, Bayer Schering Pharma AG, Berlin, Germany), followed by 10 ml of saline (0.9% NaCl) intravenously through the cephalic vein. During the angiographic examination, a coronal T1-weighted sequence was obtained using the following imaging parameters: TR = 2.9 ms, TE = 1.1 ms, slice thickness = 1 mm, FOV = 270×360 mm^2 and a 288×521 matrix with a voxel size of 0.93×0.7×1 mm. Following the MR imaging, the animal was transferred in the same position to the CT unit, and then CT scanning was carried out (130 kV, 30 mAs, slice thickness = 1 mm, pitch = 0.5, spiral scanning mode). The head and the cervical region up to the third cervical vertebra were scanned. For reconstruction, a soft tissue-specific (J30s kernel) reconstruction and a bone-specific reconstruction (H70s kernel) with a voxel size of 1×1×1 mm was used.

After the *in vivo* imaging, the animal was euthanized while still under general anaesthesia by intravenously administering a 1.5 ml of T-61 injection (T-61 solution, Merck Animal Health Company, Kirkland, Canada). Two hours later, while the animal was still in dorsal recumbency, both the common carotid arteries and the external jugular veins were minimally invasively exposed near the thoracic inlet, and cannulas were placed into the vessels. An 18 ml aliquot of red polyurethane rubber (VytaFlex-10, Smooth-On Inc., Macungie, Pennsylvania, USA) was injected through the common carotids to fill the arterial system of the head. Two and a half hours postmortem, the same MR protocol (except MR angiography) was performed on the cadaver to provide the possibility for antemortem and postmortem comparison and to check the brain for the resin filling. Following the repeated MR scanning, the cadaver was placed into a -80°C deep freezer to minimise further lytic process taking place after death and to prepare the tissues for cryosectioning. To obtain a high-resolution CT image series from the skull, the frozen head block (separated at the level of the sixth cervical vertebra) was scanned with a YXLON Precision microfocus CT (240 kV, 2 mAs, number of projections = 1260, FOV = 1024×1024, voxel size = 0.23×0.23×0.23 mm).

4.4.3. Block embedding

3D reconstructions were made from the acquired DICOM images using Amira software. Based on the *in vivo* and *ex vivo* CT and MR images, we precisely defined the transverse plane of milling, and the preferred boundaries of the frozen neurocranium block were determined (**Figure 37**). The horizontal extension extended from the level of the infraorbital foramen to the cranial vertebral incisure of the third cervical vertebra (a total of 150.19 mm). The vertical extension went from the highest point of the calvaria to the level of the upper fourth premolar teeth (a total of 80.06 mm). Based on this 3D model, a head block was made and embedded into a custom-made thermoregulated plexiglass box using the earlier tested gelatin solution.

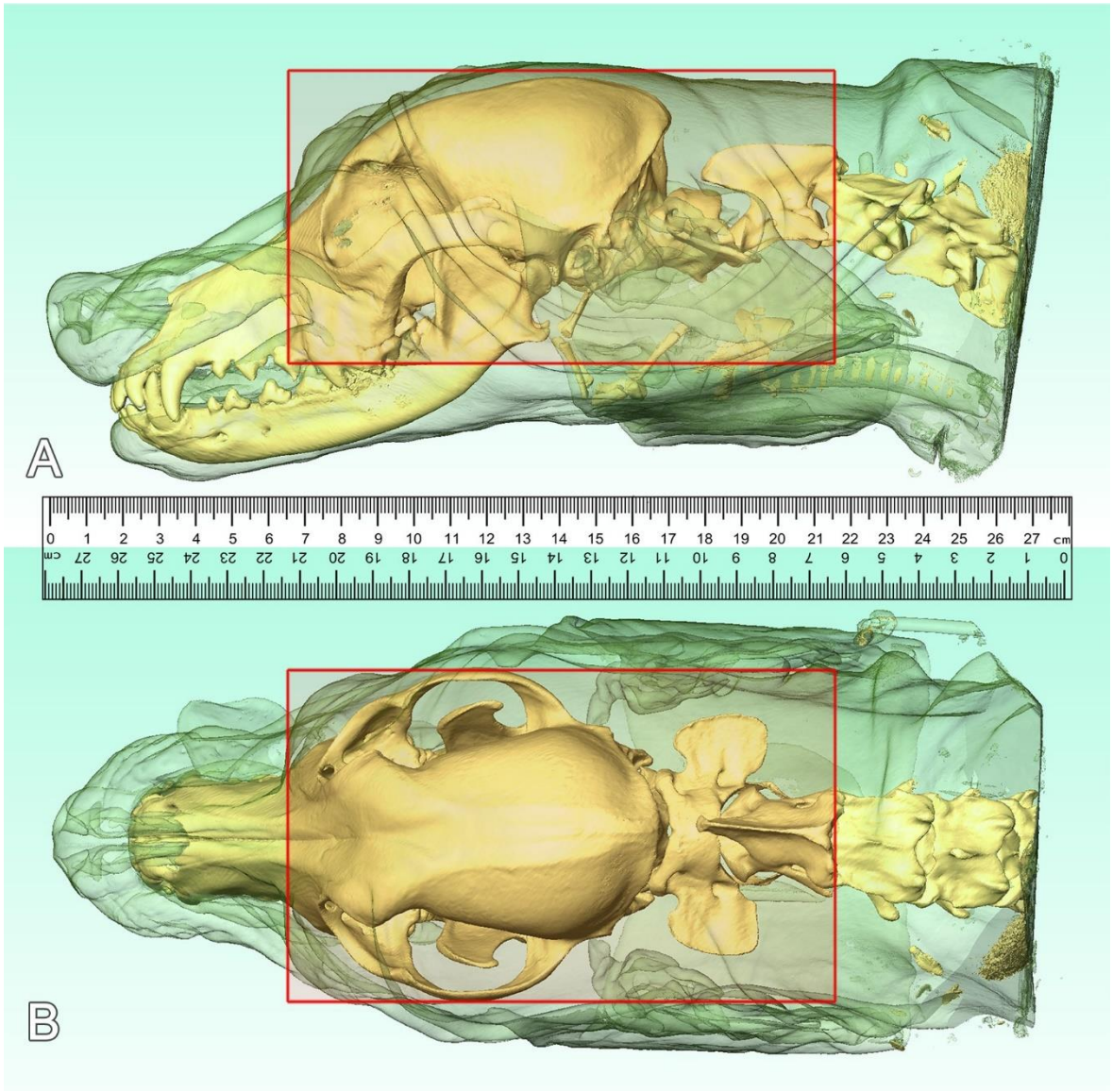

Figure 37. Localising the boundaries of the beagle head block. Based on the CT scans, 3D models were made to determine the borders of the block (shown with a red rectangle). Skin presented with 70% opacity, bones in white–yellow. A) Lateral view. B) Dorsal view.

4.4.4. Cryosectioning

The cryomacrotomisation was performed with that same Kondia NCT B-640 precision milling machine (NCT Industrial Electronics Ltd., Budapest, Hungary), which system's properties we find to be optimal in our pilot studies. The milled surface was cleaned with 10% isopropyl alcohol, cooled before each sectioning with a CO_2 cryo-gun (Linde AG, Germany) and ground with dry ice pellets. The embedding box was repeatedly filled with dry ice to achieve sufficient mantle cooling around the block (**Figure 38**). Liquid nitrogen was also used to cool the block. The layer thickness was set to be 100 µm for the milling (rotational speed = 3000 RPM, cutter diameter = 200 mm, feed rate = 300 MPR). We used a Nikon D800 camera and an AF-S VR Micro-Nikkor 105 mm f/2.8G IF-ED lens with polarised filters and colour checkers (ISO-100, focus distance 105 mm, exposure time 1/200 sec, max aperture 3.1, F-stop f/8, with X-Rite ColorChecker passport and polarising filters). Photos were recorded in 24-bit colour depth and 300 DPI raw images; the dimension of each picture was 7360×4912 pixels, which was set to the extent of the neurocranium block. Overall, we recorded 1112 images.

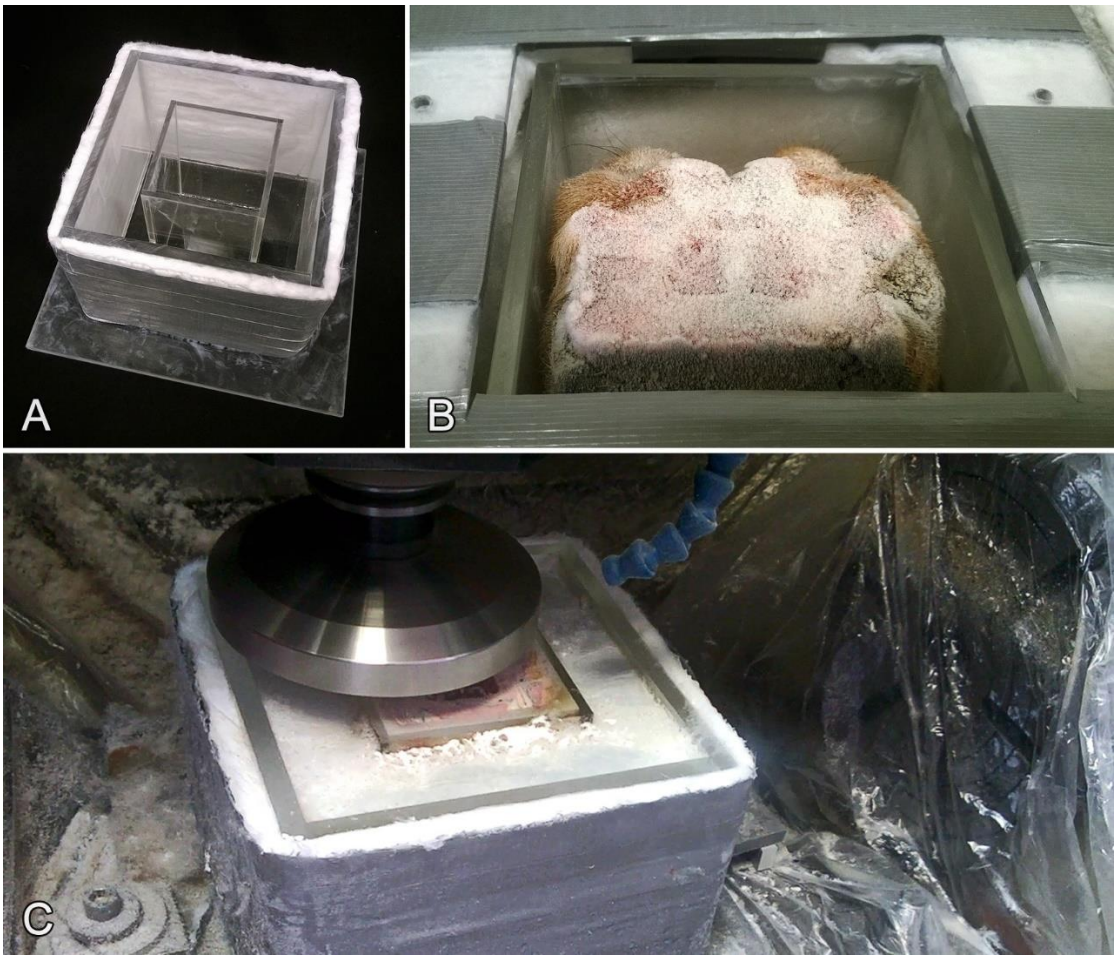

Figure 38. The plexiglass embedding box during the different stages of the procedure. A) The empty box. B) With the beagle head block. C) During the cryosectioning.

4.4.5. Image registration

The RGB images were imported into the Amira program, creating a single volume where the voxel size was 19.5×19.5×100 μm; then the DICOM images from the *in vivo* and *ex vivo* CT and MR imaging were also brought into the same "*Project View*" space. Possible shifts between adjacent colour images were corrected with the "*Align Slices*" module, and then the whole volume was resampled and joint photographic experts group (JPEG) format images were exported in all the main orthogonal (dorsal, sagittal, transverse) planes. CT images were aligned with the MR images using the "*Register Images*" module, and the whole RGB volume from the cryomacrotomisation was also fit to the MRI series. Thus, all three volumes (MR, CT and cryosectioned RGB images) were in the same coordinate system. Registration steps included rigid and non-rigid transformations. The rigid transformations were rotation and translation, and the non-rigid transformations were isoscaling, anisoscaling and shearing. The metrics used in Amira during the registration included "*Correlation*" and "*Normalized Mutual Information*". The primary data of the registration consisted of the cryosectioned image volume, and the data overlaid on it was the bone kernel-defined CT volume. The registration was accomplished automatically by the software. After aligning the centres of the primary and overlay data, a rigid transformation was applied, followed by a non-rigid transformation. In the multiplanar viewer the overlay of the two image sets was checked in all of the three main orthogonal planes.

Fitting of the osseous structures, which were clearly visible in both the cryosectioned and CT images, was used to verify the proper alignment. The verification also included inspection of the area of the lamina cribrosa, the frontal sinus, external sagittal crest, external occipital protuberance, tympanic bulla, and the placement of the basioccipital, basisphenoid and presphenoid bones. After the registration was successfully completed between the two datasets, the CT series was resampled using the "*Resample transformed image*" module. Next, the aligned CT series was used as a primary dataset and the MR series was used as the overlay dataset, and rigid and non-rigid transformations were applied as described above to properly align the two datasets. After checking the results of the co-registration, the MR image volume was also resampled, and thus all three image volumes were aligned with each other. Using the "*Slice*" module, the same orthogonal views could be set on the three imaging modalities, making them directly comparable in the same position according to the global coordinate system. Additionally, the beagle MR data was co-registered to the individual golden retriever template brain and the corresponding MRI label map.

4.4.6. Digital endocranial casting

The DICOM images from the high-resolution CT imaging series were imported to the 3D Slicer program (freeware, https://www.slicer.org), and the sagittal, dorsal and transverse planes were established for the later segmentation work using the "*Reformat*" module. The "*CastImageFilter*" effect of the "*Simple Filters*" module provided higher contrast to the osseous structures. First, the midsagittal plane was set; then the dorsal plane was defined using the basisphenoid–basioccipital axis and the bilateral cupula cochleae, and finally the transverse plane was set to be perpendicular to both the sagittal and dorsal planes (**Figure 39**).

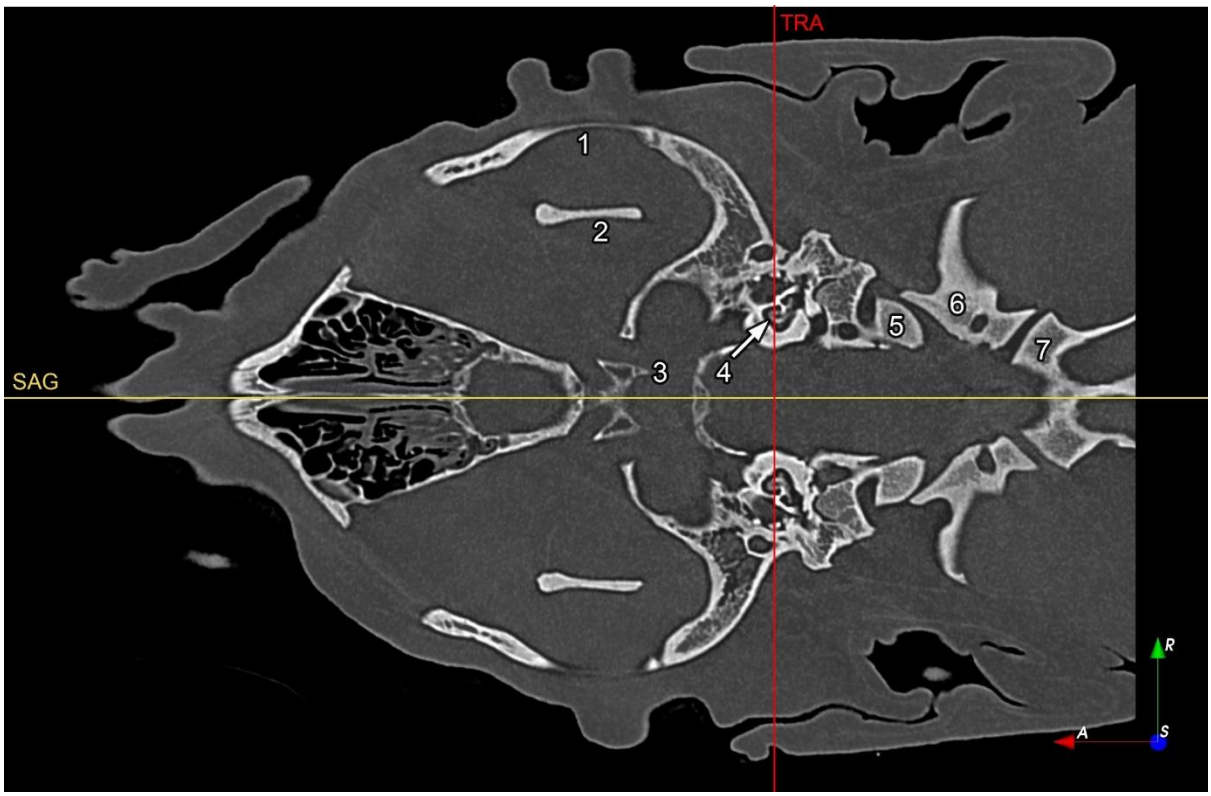

Figure 39. High-resolution CT scan of the beagle head, reformatted in the dorsal plane. Sagittal (SAG, in yellow) and transverse (TRA, in red) planes are visualised in the image. 1) Arcus zygomaticus. 2) Ramus ossis mandibulae. 3) Processus clinoideus rostralis. 4) Cupula cochleae. 5) Condylus occipitalis. 6) Atlas. 7) Axis.

Using the "*Segment Editor*" module, a skull segment was created based on automatic thresholding to highlight all the osseous structures (**Figure 40/A, B**). After that, an endocranial block was made that covered the entire neurocranial cavity, overlapping with the surrounding bones (**Figure 40/C**). Performing a subtract command with the "*Logical operators*" menu, the skull segment was subtracted from the extended endocranial block; thus, as a result, the endocranial contour exactly followed the endosteal lining (**Figure 40/D**).

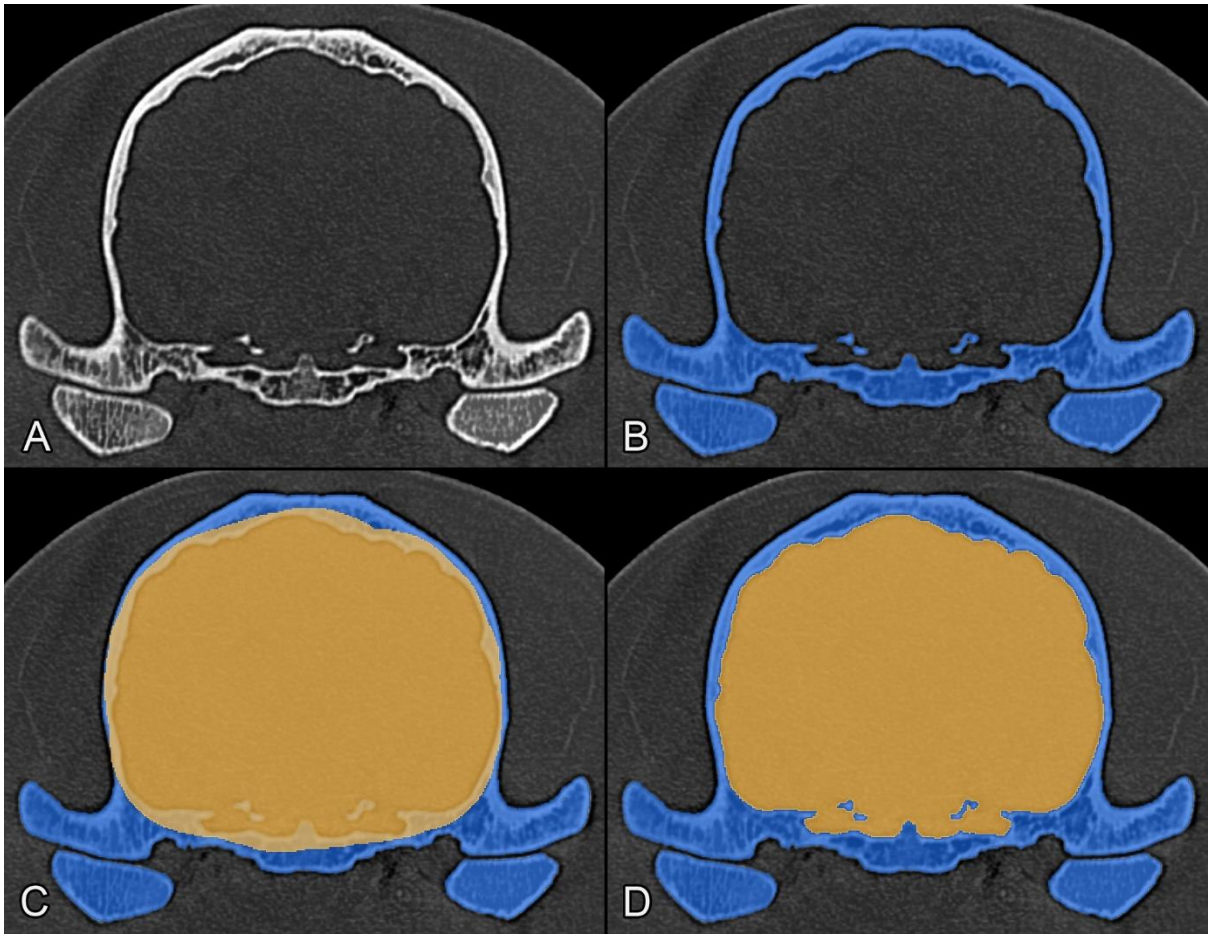

Figure 40. Main steps of the endocast segmentation. A) Transverse CT of the beagle skull at the level of the dorsum sellae. B) The segmented osseous structures (in blue). C) Creating an extended endocranial block (in yellow). D) The result after the subtraction operation.

Openings in the skulls were closed along the orthogonal planes where the channels left the skull (e.g., canalis opticus and fissura orbitalis were closed along the transverse plane, meatus acusticus internus and foramina ethmoidales along the sagittal plane or foramen ovale, and foramen caroticum along the dorsal plane). The meatus temporalis was closed below the level of junction with the intracranial space along the dorsal plane, whilst the canalis condylaris, canalis sinus transversi, canalis caroticus and canalis petrooccipitalis were kept as a connected part of the endocast.

Following the segmentation procedure, a surface model was exported in STL format and refined with MeshMixer. The final 3D model was visualised with 3D Slicer from different angles, and a 3D portable document format (PDF) document was also created. This PDF enables the reader to interact with the model (e.g., jump to predefined views, rotate or slice the model and modify its visibility) without the need of any special 3D software; it only requires a standard PDF reader (e.g., Adobe Acrobat Reader, https://www.adobe.com) (**Figure 41**).

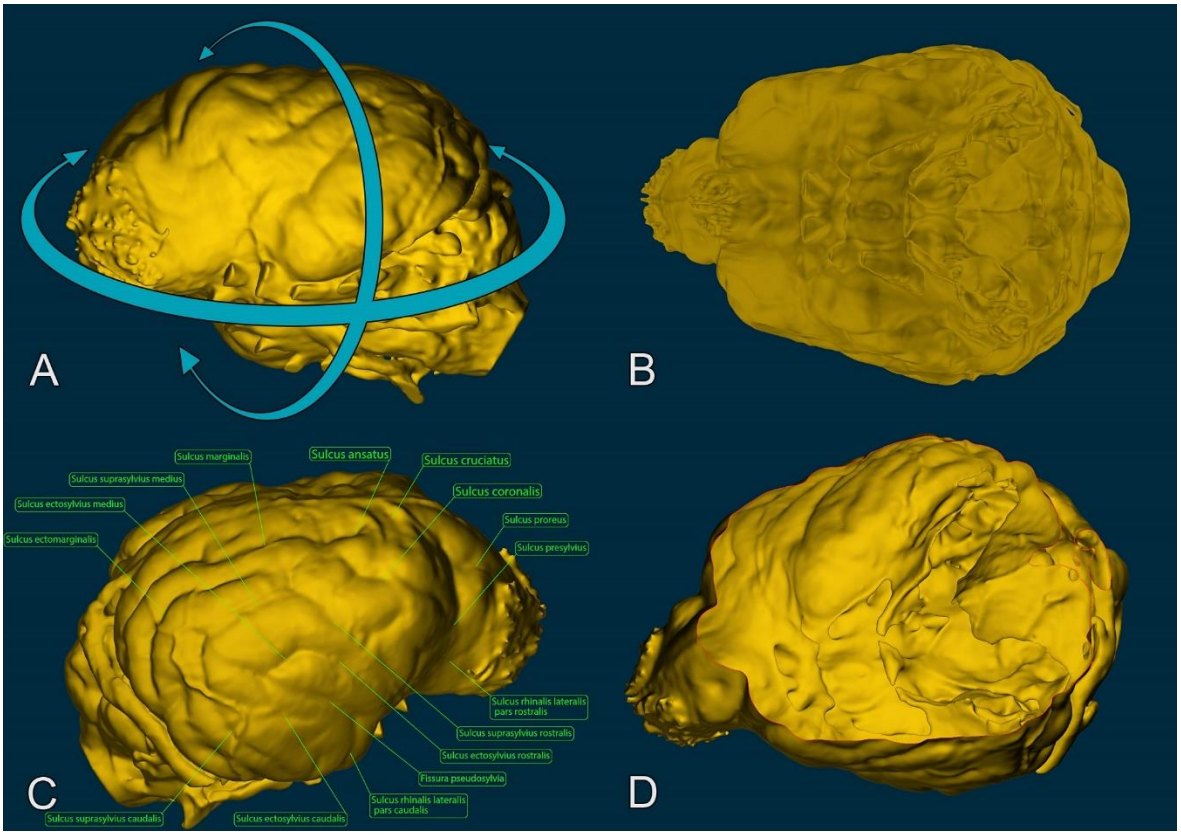

Figure 41. Main features of a 3D PDF. A) Models can be rotated in every direction. B) Transparency can be changed. C) Annotations and figure scenes can be created. D) The 3D model of the beagle endocast can be cut at arbitrary angles to view inside.

Annotations were also made in this 3D PDF to interactively show the placement of the impressions of the main gyri, sulci, foramina and channels on the beagle endocast, which consequently reflects the underlying brain's morphology. Finally, the STL model was 3D-printed with SLS technology in actual size, and its surface was colorized with an acrylic dye.

4.4.7. Segmentation and 3D modelling

Adobe Photoshop CS3 (https://www.adobe.com) was used to create two sets of greyscale images from the original RGB series with selective filtering and enhancing the structures to filter out the vessels for the semi-automatic segmentation. To highlight the arteries and veins, Photoshop action files were created which performed a pre-programmed action series on multiple images. In the case of the arteries, a "*High pass filter*" was used to enhance the contrast, the 'red' channel was extracted to a separate layer from the RGB image, and selective colour reducing was carried out on the red channel. Subsequently, a black and white conversion was applied by removing the cyan tones, and then the contrast was enhanced and the brightness was slightly reduced with the "*Brightness and contrast*" module.

Then, the RGB image was converted and saved in greyscale to allow the segmentation with Amira. To select the veins (which were already dark due to the postmortem highly deoxygenated blood they contained, which also made their distinction easier), the "*Color balance*" and "*Selective color*" modules were used to increase the tone of the veins. A black and white conversion was then applied, and the contrast was increased in the "*Brightness and contrast*" module, followed by a decrease in the gamma correction. Following that, a greyscale conversion was performed and the sample image was saved. The complete batch process was recorded in separate Photoshop action files for the arteries and veins. After creating these action files, an automatic process was initiated which converted all of the 1112 cryosectioned RGB images (**Figure 42**). The JPEG image series was imported into Amira, and the same 19.5×19.5×100 µm volumes were generated and aligned with the original RGB volume. For each greyscale volume, an "*Edit New Label Field*" module was generated, and a manually controlled semi-automatic segmentation was performed in the "*Segmentation*" area. The brain, bones, arteries and veins were labelled separately. Stereolithography models were created from each label field using the "*Generate Surface*" module. Smoothing and refinement of the STL models were carried out in Amira and MeshMixer.

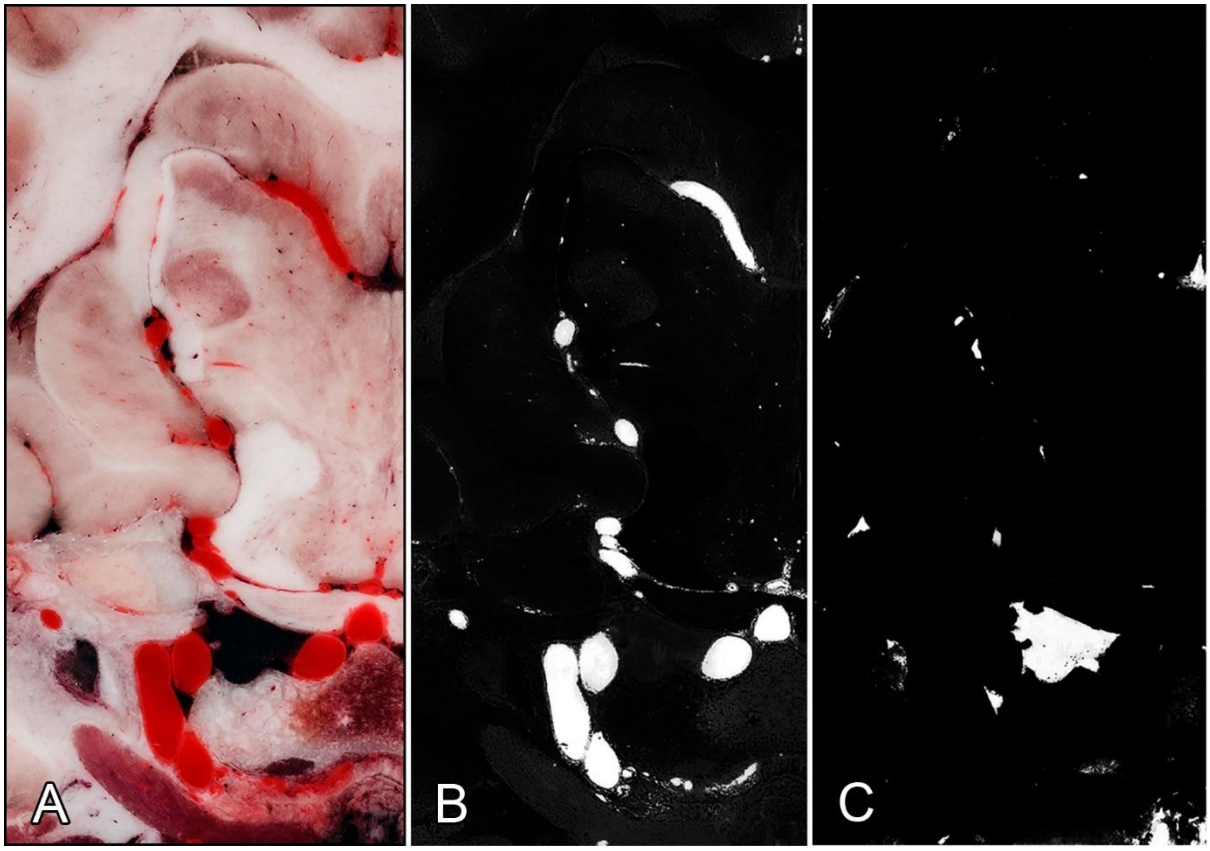

Figure 42. Subtracting the vessels from a cryosectioned image, demonstrating the effect of the applied filters on the same slice. A) Original RGB image. B) Greyscale image with the arteries selectively filtered out. C) Greyscale image with the veins selectively filtered out.

5. Results

5.1. Recording high-resolution anatomical images

By using that CNC milling machine which provided an optimal workflow and a decreased artefact-formation together with applying high-resolution DSLR photography, the brain and the surrounding structures were visualised with a high level of clarity and detail. The resolution and the quality of the images are demonstrated with close-up views showing the fine details of the ethmoturbinates (**Figure 43**), or structures of the middle cranial fossa (**Figure 44**).

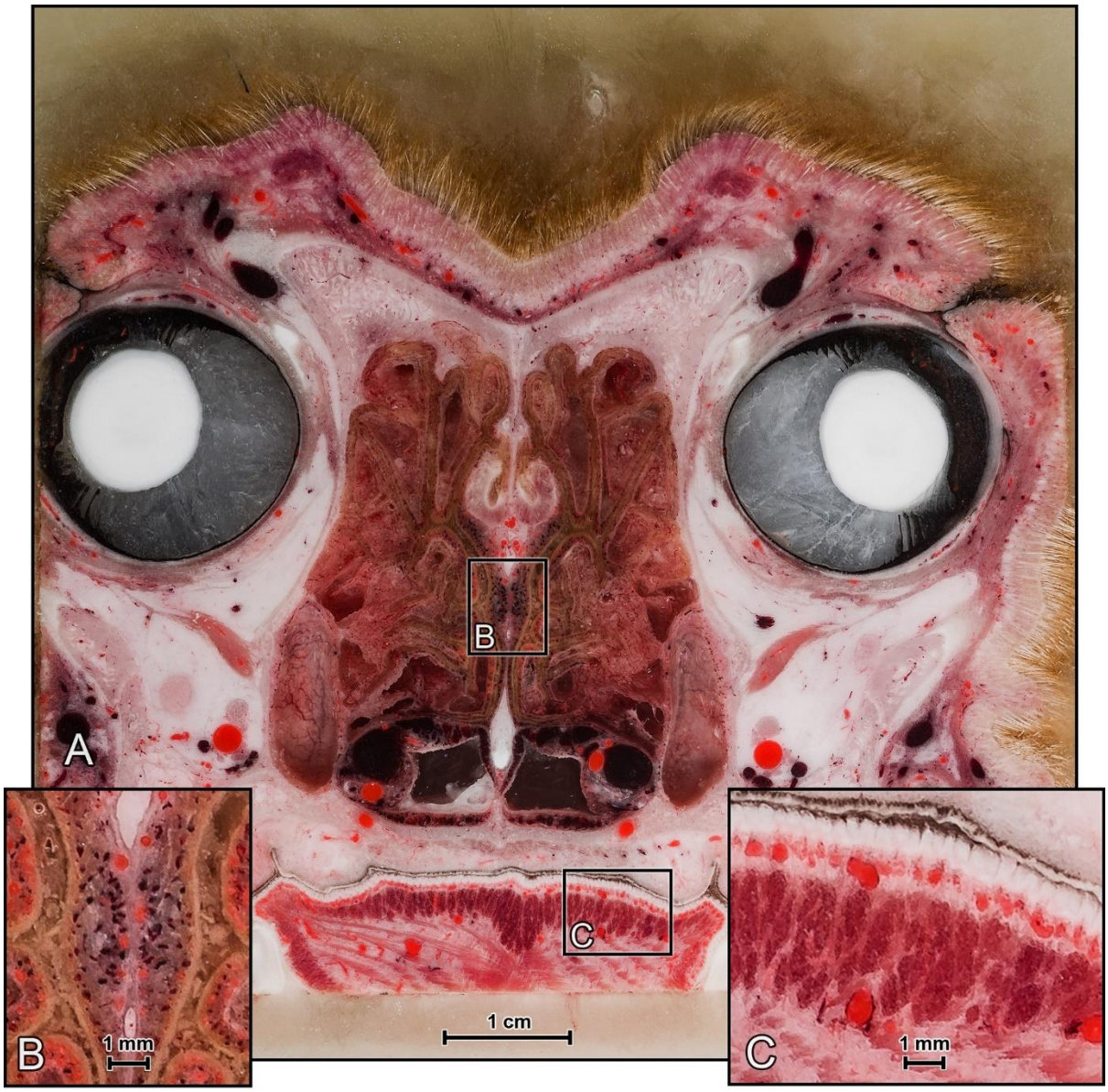

Figure 43. Transverse section at the level of the eyeball of the beagle, showing the result of the milling and the high resolution photography. A) Cryosectioned image. B) Vessels of the nasal septum and the ethmoturbinates. C) Intrinsic muscles and vessels of the tongue.

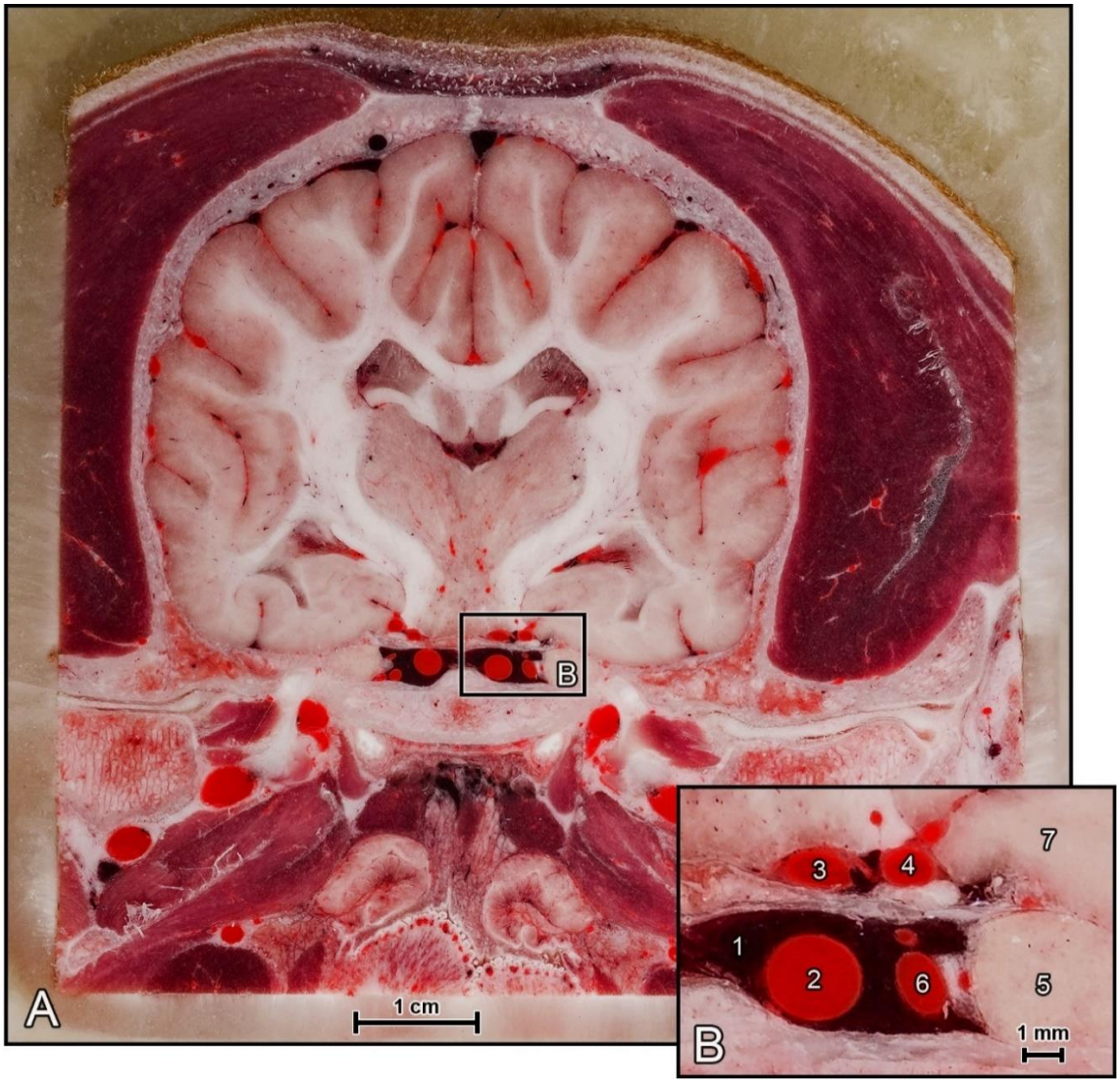

Figure 44. Transverse section at the mid-thalamic level of the beagle head block. A) Cryosectioned image. B) Close-up view. 1) Sinus cavernosus. 2) A. carotis interna. 3). A. communicans caudalis. 4) A. cerebri caudalis. 5) N. ophthalmicus et maxillaris. 7) Subiculum. 6) R. anastomoticus cum a. carotide interna of a. ophthalmica externa.

As we evaluated the quality of the images, we had to take into consideration those changes which can result from the cooling process. Artefacts can occur because the brain contains a large amount of water (approximately 70%). Rapid cooling of the tissues during the embedding procedure (using liquid nitrogen or dry ice) can result in soft tissue expansion. We observed this effect, as a small part of the splenial gyrus was moved underneath the tentorium cerebelli membranaceum, and the pyramid of the vermis moved towards the foramen magnum. The subarachnoid space and the encephalic ventricles were also smaller compared to those seen on the MRI. If the cooling process is not properly performed, or it takes a longer time to freeze the block, then discoloration of the grey matter and so-called “freeze line” artefacts can be seen during the cryosectioning, as we had seen it in our pilot studies (**Figure 45**).

Another case that can arise during cryosectioning is when fibrous tissues are present in the working area (e.g., tendons or thicker perimysium and epimysium). These tend to become frayed or fibrous if they are not properly cooled prior to sectioning, and they are not milled down sufficiently by the device (**Figure 46/A**). This phenomenon has also been observed by other researchers (Park et al., 2014; Spitzer et al., 1996). If this happens, then manual intervention is required, for example, using a scalpel or scissors to trim these fibres. However, if the upcoming layer is appropriately cooled, this ensures optimal results in the cryosectioning (**Figure 46/B**). During the cryomacrotomisation of the brain in the final beagle study we did not see freeze lines on the surfaces, which confirmed that the cooling of the neurocranium block was appropriate. No signs of discoloration occurred, and any major fibres that formed in the course of the milling were continuously cut to remove the filaments. Hence, the grey matter appeared in its original reddish colour, and even though no tissue staining was applied, the boundary between the grey and white matter and the location of the major subcortical nuclei could be clearly identified (**Figure 47**).

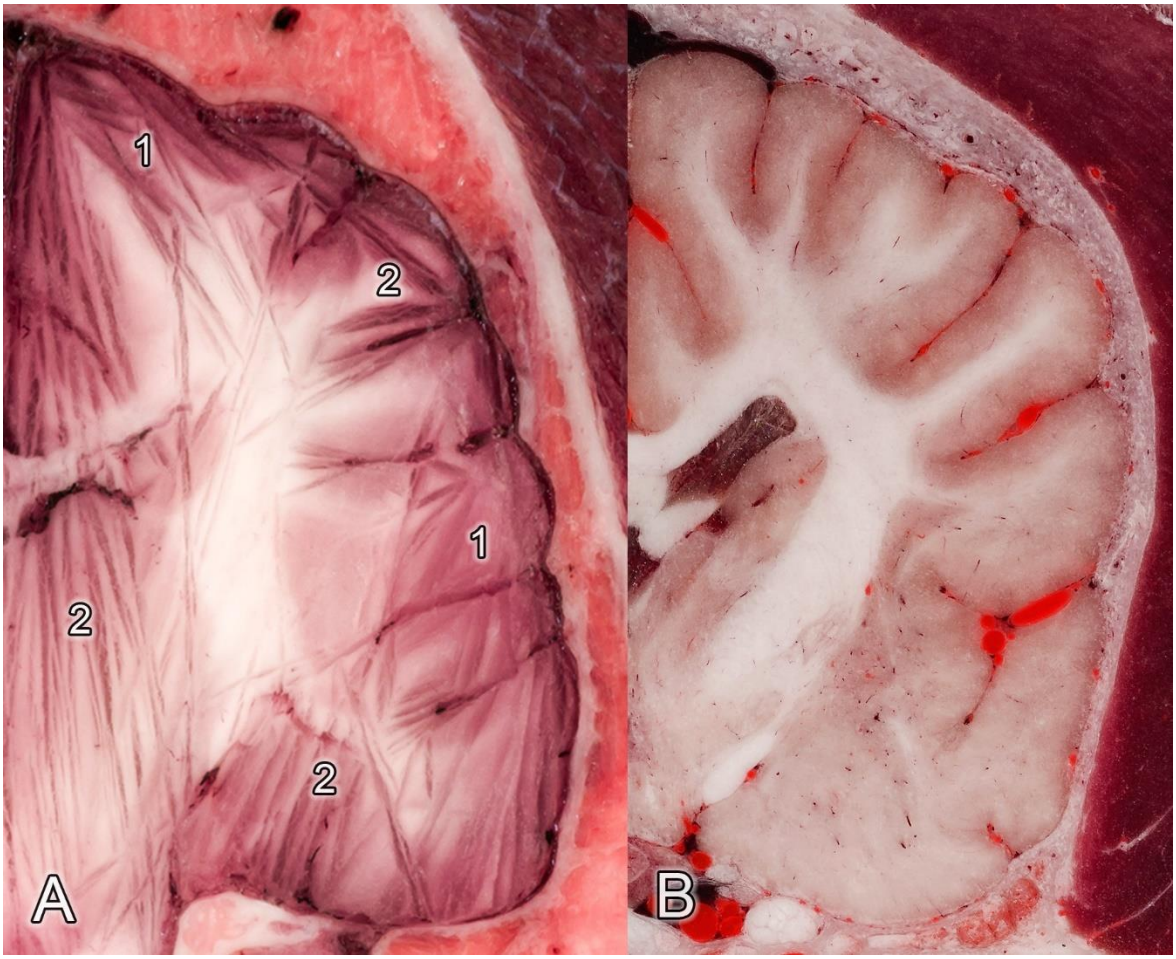

Figure 45. Transverse, cryosectioned RGB images. A) Dog brain from the fifth pilot study. B) Dog brain from the final study. 1) Discoloration of the grey matter. 2) Freeze line artefact.

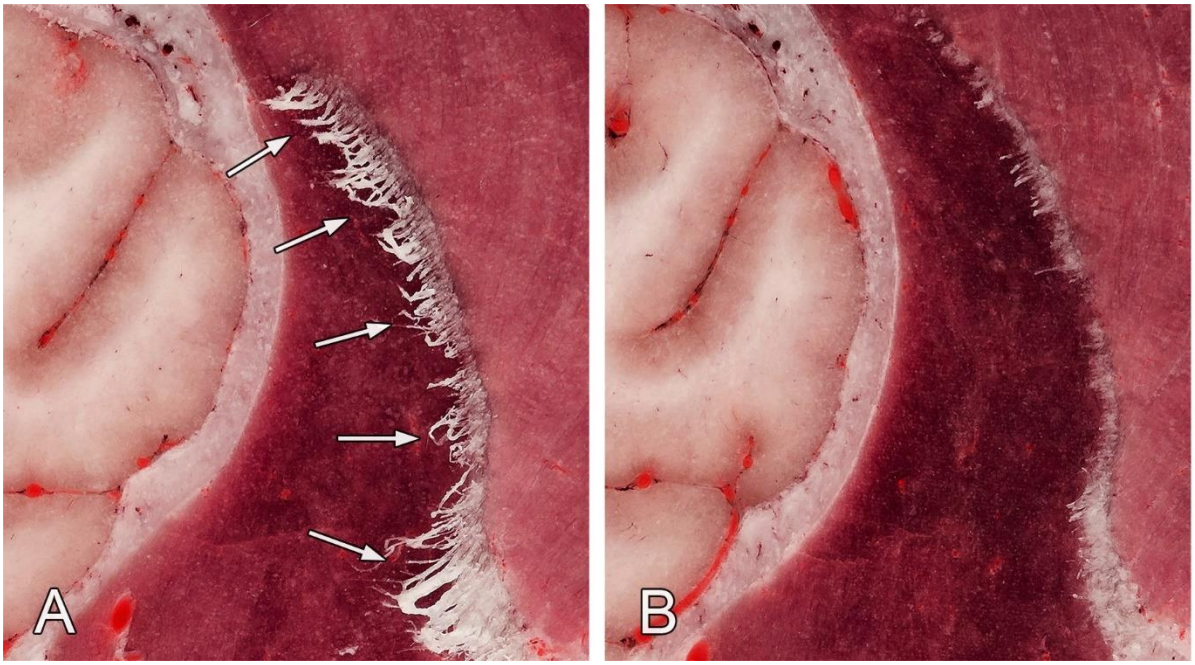

Figure 46. Demonstrating the importance of proper cooling to prevent fibre formation. A) Arrows show the fibrous tendinous tissue of the temporal muscle attaching to the coronoid process of the mandible. B) After treatment with dry ice and liquid nitrogen, these fibres hardened enough to eliminate them in the upcoming sectioning.

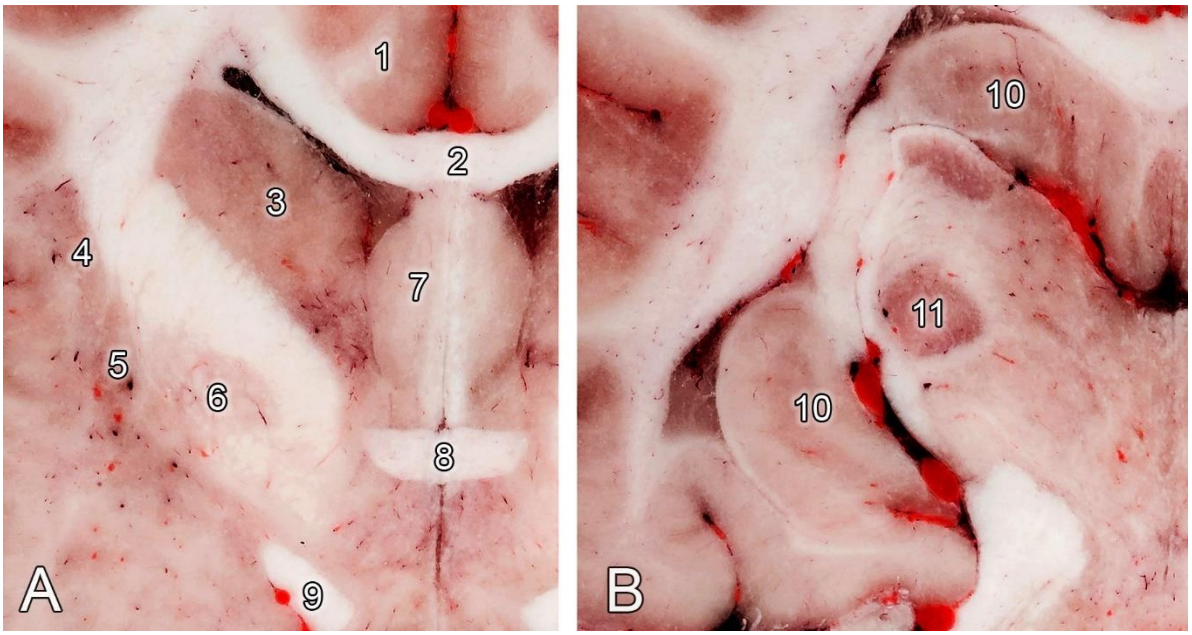

Figure 47. A zoom-in of the beagle brain in the RGB images showing the subcortical nuclei and tracts. Transverse sections. A) At the level of the rostral commissure. B) At the level of the lateral geniculate body. 1) Gyrus cinguli. 2) Corpus callosum. 3) Nucleus caudatus. 4) Claustrum. 5) Putamen. 6) Pallidum. 7) Area septalis. 8) Commissura rostralis. 9) Tractus opticus. 10) Hippocampus. 11) Nucleus geniculatus lateralis.

5.2. Multimodal visualisation of the imaging datasets

The relatively small (100 µm) slice interval made it possible to reconstruct the other orthogonal (dorsal and sagittal) planes without losing the details of the individual structures (**Figure 48**). This means that even at higher magnifications, the structures of the computer-reconstructed (CORE) slices appear sharp, detailed and uninterrupted, as if the cryosectioning had occurred along that plane. Registering the CT and MR images to the cryosectioned volume resulted in a nearly perfect comparison between the different imaging modalities. Any possible biases from the original position are the result of the mild expansion of the tissues during the freezing process. Images of various sites showed good multimodal comparability (**Figures 49** and **50**).

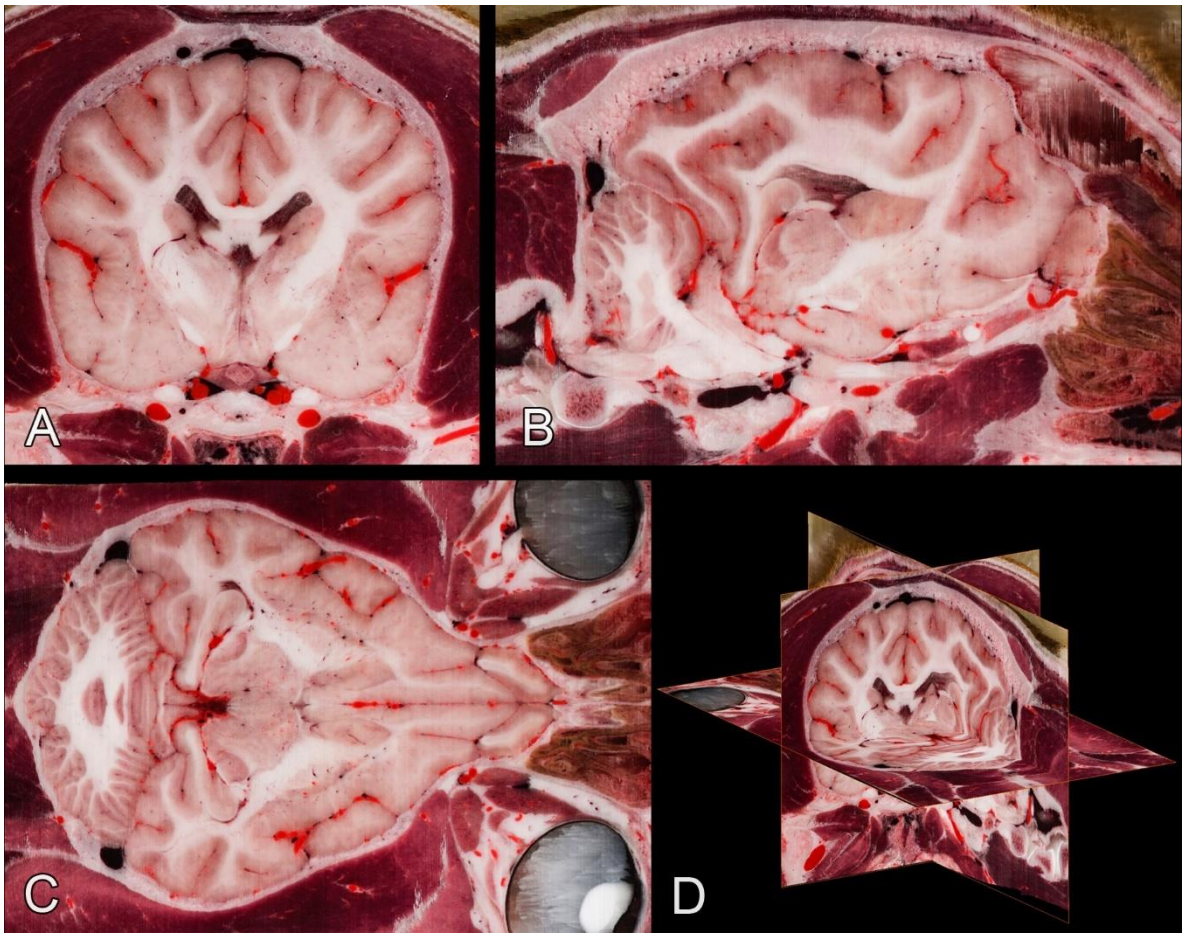

Figure 48. Multiplanar reconstructions of the beagle brain based on the original transverse cryosectioned RGB images. A) Transverse plane (original, photographic image). B) Sagittal plane (CORE image). C) Dorsal plane (CORE image). D) 3D composite image of the main orthogonal views.

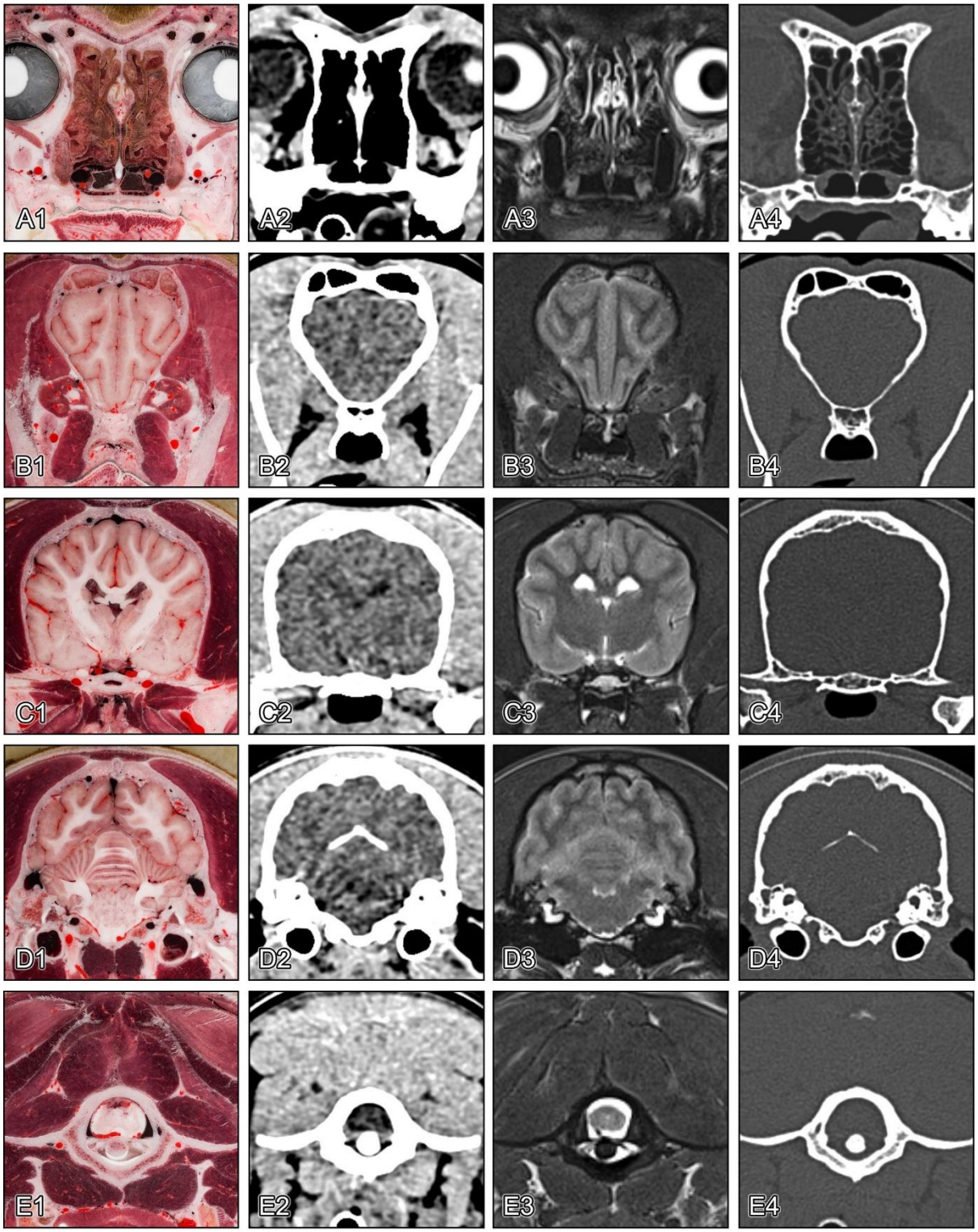

Figure 49. The different imaging modalities of the beagle head at the same transverse level. Rows: A) At the level of the orbit. B) At the level of the gyrus precruciatus. C) At the level of the hypophysis. D) At the level of the cerebellum. E) At the level of the dens axis. Columns: 1) Cryosectioned RGB images. 2) CT images with brain (J30s) kernel. 3) T2-weighted MR images. 4) CT images with bone (H70s) kernel.

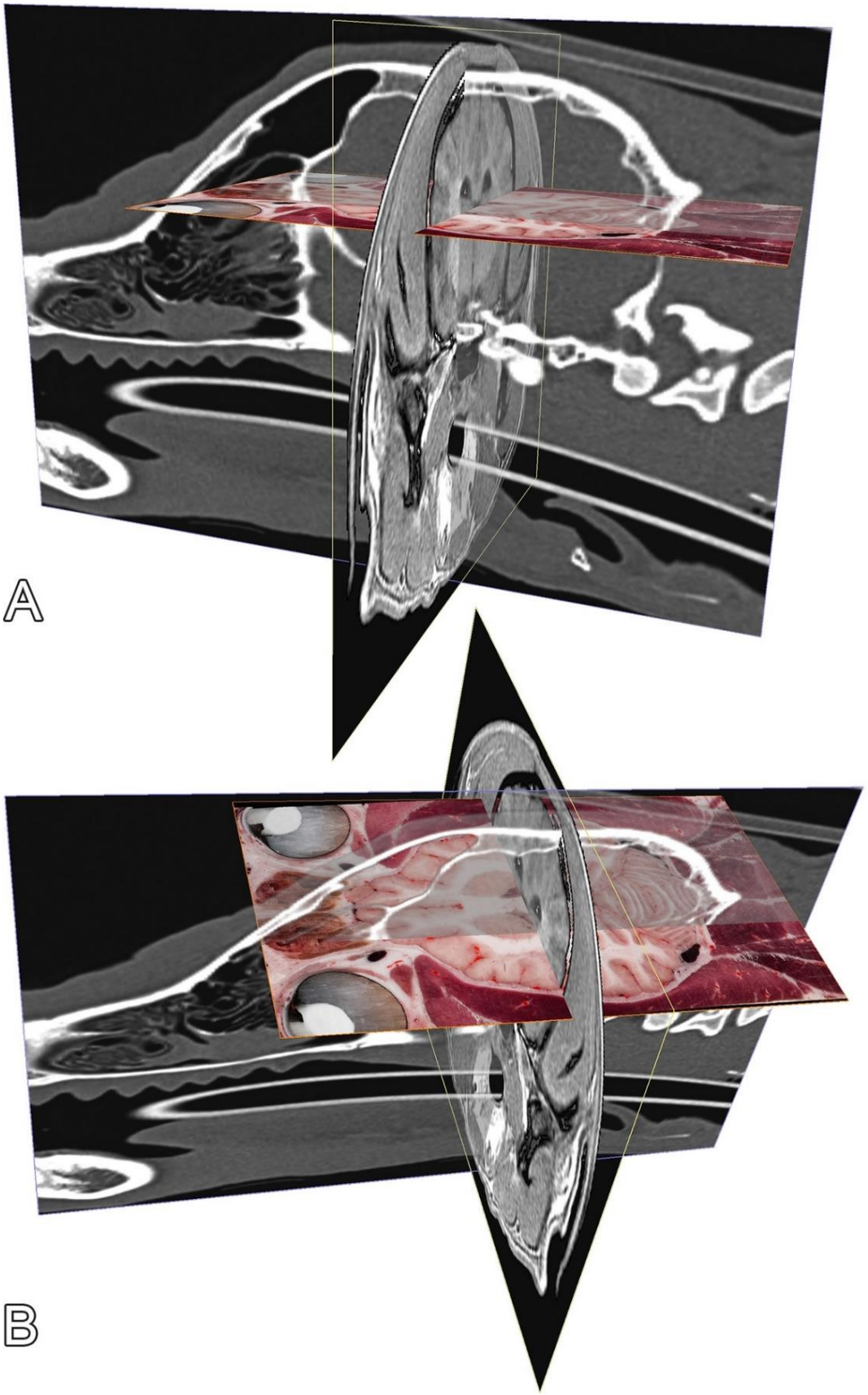

Figure 50. The co-registered imaging modalities of the beagle head in perspective views. T1-weighted MR image (in the transverse plane), CT image (in the sagittal plane) and CORE image (in the dorsal plane) are shown. A) Left caudo-lateral view. B) Left dorso-lateral view.

As a part of the data visualisation, the T2-weighted MR image sequence from the beagle study was also co-registered to the template golden retriever MR dataset. Visualising the two datasets overlaid on each other with the 3D Slicer program showed that the beagle brain volume was transformed in the same coordinate system of the template image. As a result, the localisation of the following regions were bilaterally verified to be in the same place: 1) mid of the interthalamic adhesion; 2) mid of the pituitary gland; 3) rostral end of the corpus callosum; 4) caudal end of the corpus callosum; 5) frontal pole; 6) occipital pole; 7) cruciate sulcus; 8) ramus ascendens of the splenial sulcus; 10) rostral, dorsal and caudal poles of the cerebellum; 11) roof of the fourth ventricle; 12) rostral commissure; 13) caudal commissure; 14) mid of the middle ectosylvian sulcus; 15) mid of the head of caudate nucleus; 16) hippocampus at the level of the caudal commissure; 17) mid of the caudal colliculus; and 18) widest points of the cerebrum on the temporal lobes. The evaluation performed with SPM12 also confirmed an appropriate co-registration result, and the MRI label map was subsequently projected onto the beagle dataset (**Figure 51**).

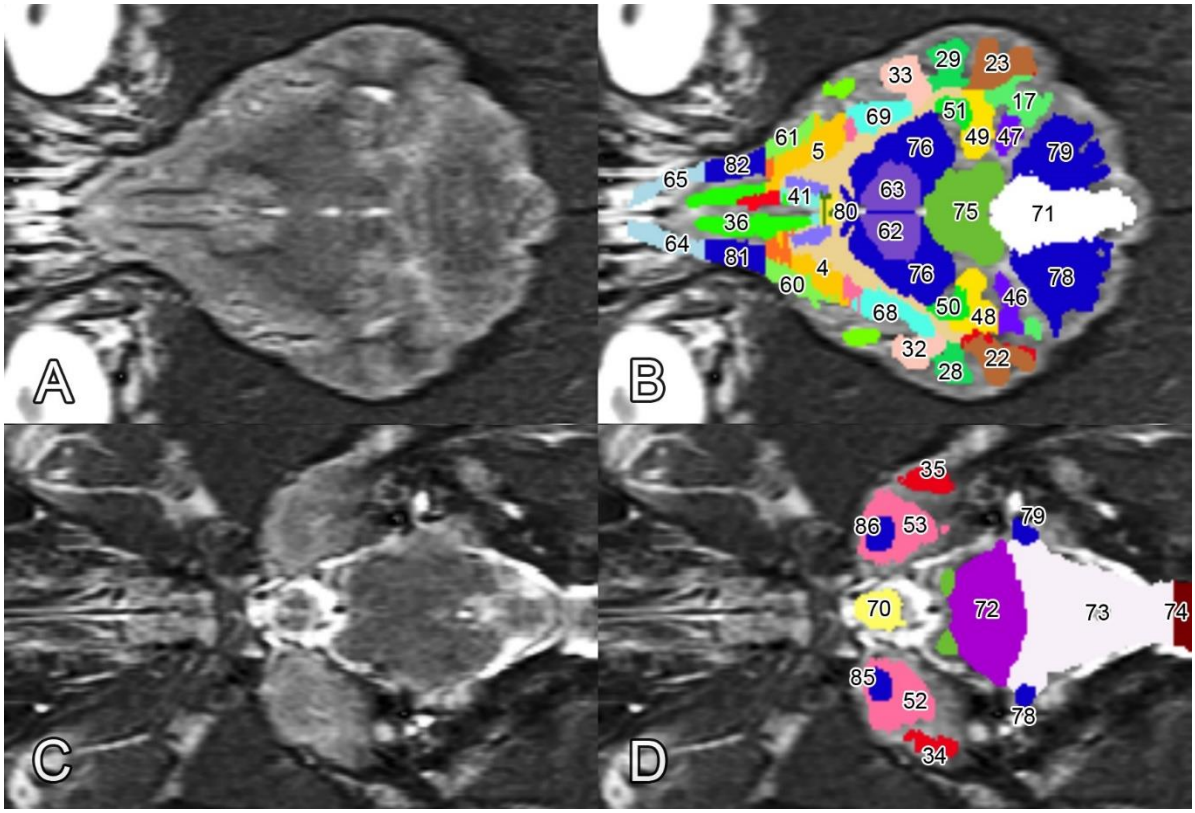

Figure 51. Projecting the co-registered MRI label map to the beagle brain data

The numbers and colours in part ‘B” and “D” of the figure are according to **Table 1.**

A, C) T2-weighted MRI of the beagle brain. B, D) Overlay of the label map on the beagle MR data. A, B) At the level of the rostral commissure. C, D) At the level of the hypophysis.

5.3. Studying brain morphology with digital endocasting

Based on the high-resolution CT dataset, it was possible to completely segment the entire endocranial surface and generate a 3D model from it, that could be projected back to the different orthogonal planes to show the highlighted endocranial cavity (**Figure 52**).

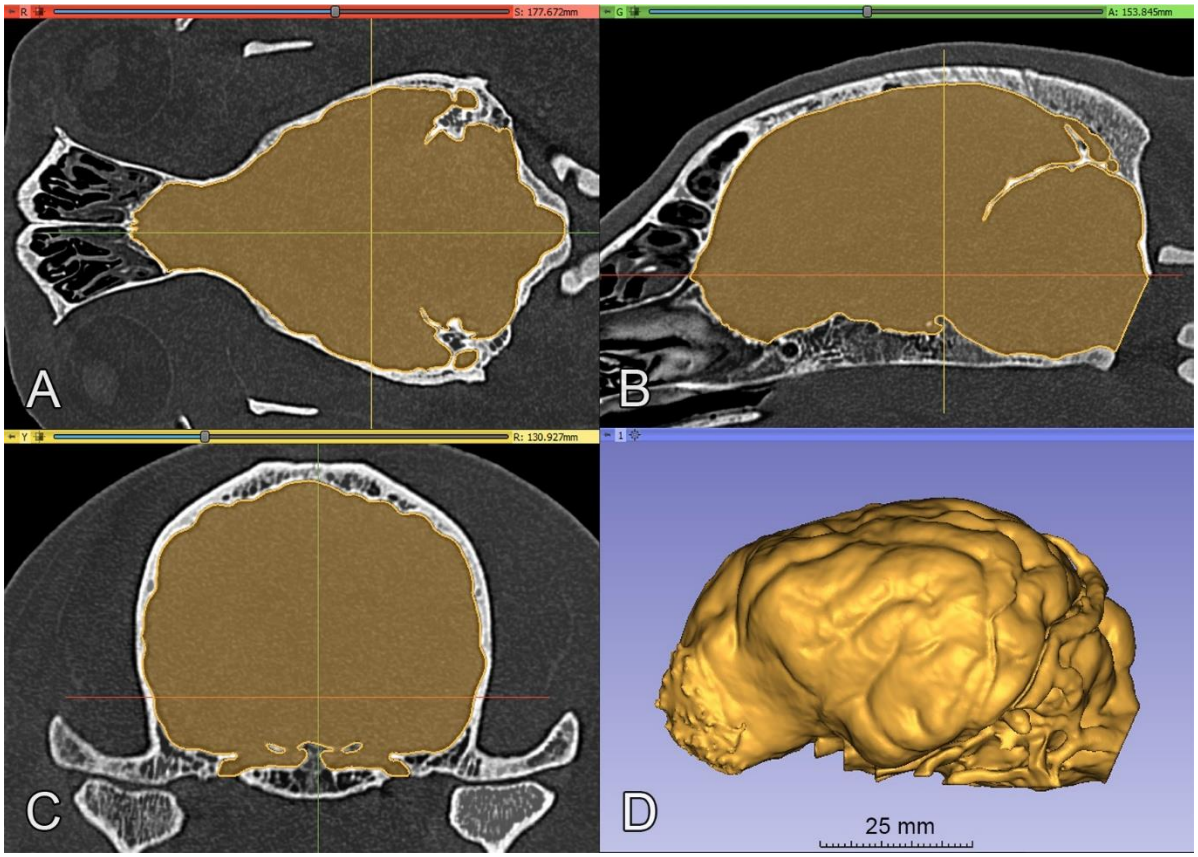

Figure 52. The endocast of the beagle. A, B, C) The model is projected onto the CT images. A) Dorsal view. B) Sagittal view. C) Transverse view. D) The final 3D model, left lateral view.

The resulting surface mesh model was so detailed that the impressions of the gyri and sulci that are located on the outer surface of the brain could be individually distinguished on the endocast together with the main channels and foramina, which serve as passageways to different intracranial blood vessels and nerves (**Figure 53**). Due to the fact that the endocast reflects the impressions and extensions on the osseous structures, it should be noted that the real size of the encephalon is slightly smaller, as there is a subarachnoid space between the endosteum and the surface of the brain. Another remark is that on the ventral aspect of the endocast where the diencephalon and the mesencephalon are located, one would mostly see the shape of the middle cranial fossa bordered by the dorsum sellae from the caudal direction and by the passageway of the different vessels and cranial nerves from the side (e.g., foramen ovale, foramen rotundum, fissura orbitalis) (**Figure 53/D**).

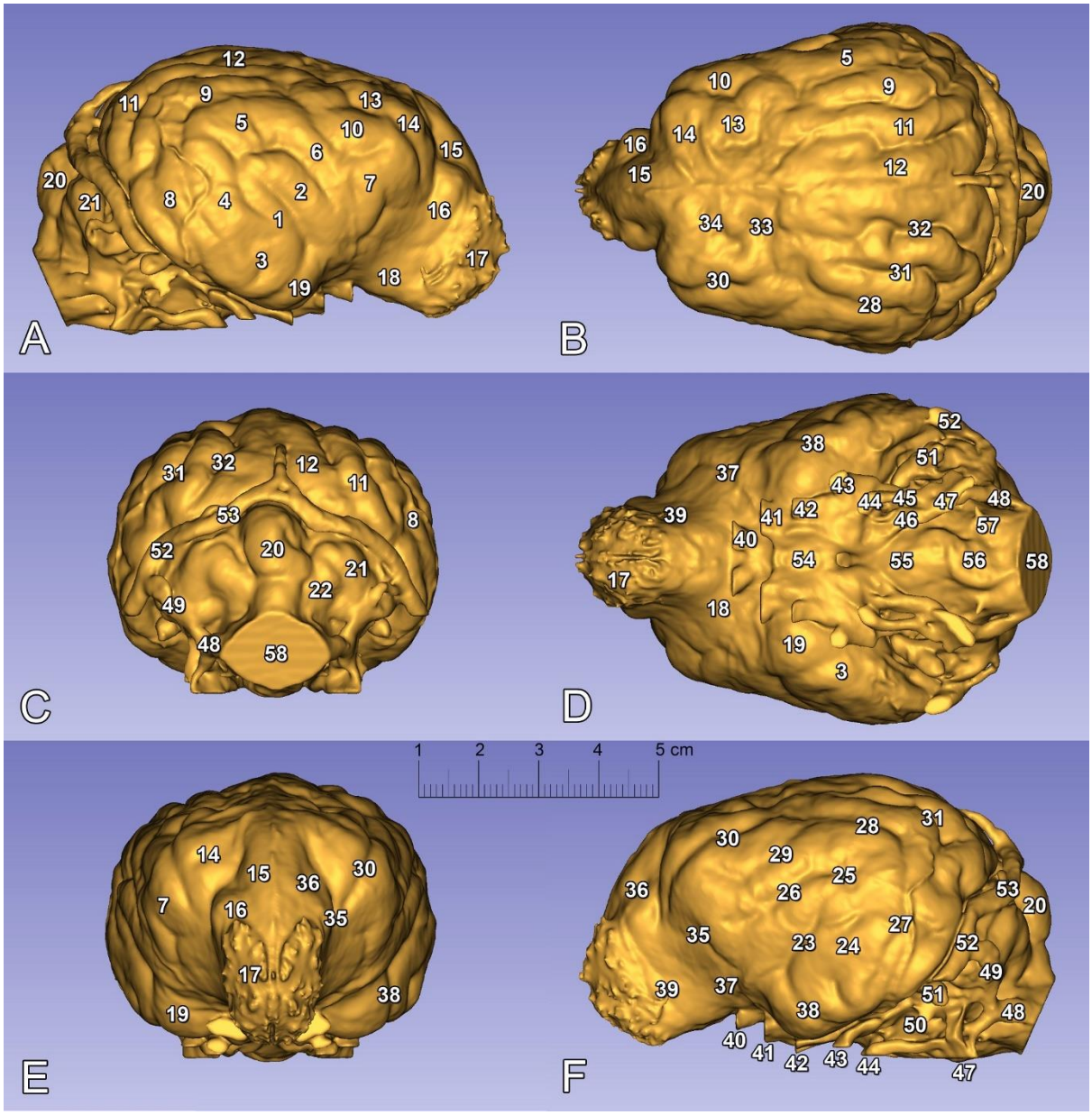

Figure 53. The endocast of the beagle. A) Right lateral view. B) Dorsal view. C) Caudal view. D) Ventral view. E) Rostral view. F) Left lateral view. 1) Gyrus sylvius caudalis. 2) Gyrus sylvius rostralis. 3) Gyrus compositus caudalis. 4) Gyrus ectosylvius caudalis. 5) Gyrus ectosylvius medius. 6) Gyrus ectosylvius rostralis. 7) Gyrus compositus rostralis. 8) Gyrus suprasylvius caudalis. 9) Gyrus suprasylvius medius. 10) Gyrus suprasylvius rostralis. 11) Gyrus ectomarginalis. 12) Gyrus marginalis. 13) Gyrus postcruciatus. 14) Gyrus precruciatus. 15) Gyrus frontalis. 16) Gyrus proreus. 17) Bulbus olfactorius. 18) Pedunculus olfactorius. 19) Lobus piriformis. 20) Tuber vermis. 21) Lobulus ansiformis cerebelli, crus caudale. 22) Lobulus paramedianus cerebelli. 23) Fissura pseudosylvia. 24) Sulcus ectosylvius caudalis. 25) Sulcus ectosylvius medius. 26) Sulcus ectosylvius rostralis. 27) Sulcus suprasylvius caudalis. 28) Sulcus suprasylvius medius. 29) Sulcus suprasylvius rostralis. 30) Sulcus coronalis. 31) Sulcus ectomarginalis.

Figure 53. ***(continued)*** 32) Sulcus marginalis. 33) Sulcus ansatus. 34) Sulcus cruciatus. 35) Sulcus presylvius. 36) Sulcus proreus. 37) Sulcus rhinalis lateralis, pars rostralis. 38) Sulcus rhinalis lateralis, pars caudalis. 39) Foramina ethmoidalia. 40) Canalis opticus. 41) Fissura orbitalis. 42) Foramen rotundum. 43) Foramen ovale. 44) Foramen caroticum. 45) Canalis caroticus. 46) Canalis petrooccipitalis. 47) Foramen jugulare. 48) Canalis condylaris. 49) Foramen mastoideum. 50) Meatus acusticus internus. 51) Fossa subarcuata. 52) Meatus temporalis. 53) Canalis sinus transversi. 54) Fossa hypophysealis. 55) Impressio pontina. 56) Impressio medullaris. 57) Canalis nervi hypoglossi. 58) Foramen magnum.

Due to the high-resolution CT scanning and the thorough segmentation process, one can also see the imprintings of the arteries on the endocast. For example, the course of the middle meningeal artery can be seen as it crosses the lateral surface of the hemispheres (between structures 4 and 8 in **Figure 53/A**, or next to structure 27 in **Figure 53/F**), and the curve of the basilar artery is visible on the ventral aspect (next to structure 56 in **Figure 53/D**). As the surface area and the volume of a mesh are automatically calculated by the software, both of them could be precisely measured; the surface area of the endocast was 149.745 cm^2, whilst the total volume of the endocast was 91.193 cm^3.

To show the 3D model interactively, a 3D PDF was created based on the digital model in which the endocast can be studied not only from predefined scene views but from any arbitrary angle by rotating the object (available on Figshare: https://figshare.com/s/aa55495db0dacfdec2c4). The model can be visualised with different settings with regard to the cutting plane, opacity or lighting effects and is also supported with various annotations. A total of 12 scene views were created and 62 structures were marked on the endocast as follows:

- Annotations in the ‘Gyri’ view: gyrus proreus, gyrus precruciatus, gyrus postcruciatus, gyrus suprasylvius rostralis, gyrus suprasylvius medius, gyrus suprasylvius caudalis, gyrus frontalis, gyrus marginalis, gyrus ectomarginalis, gyrus compositus rostralis, gyrus compositus caudalis, gyrus ectosylvius rostralis, gyrus ectosylvius medius, gyrus ectosylvius caudalis, gyrus sylvius rostralis, gyrus sylvius caudalis.

- Annotations in the ‘Sulci’ view: sulcus presylvius, sulcus proreus, sulcus coronalis, sulcus cruciatus, sulcus ansatus, sulcus marginalis, sulcus ectomarginalis, sulcus suprasylvius rostralis, sulcus suprasylvius medius, sulcus suprasylvius caudalis, sulcus ectosylvius rostralis, sulcus ectosylvius medius, sulcus ectosylvius caudalis, fissura pseudosylvia, sulcus rhinalis lateralis pars rostralis, sulcus rhinalis lateralis pars caudalis.

- Annotations in the ‘Canales’ view: canalis opticus, fissura orbitalis, foramen rotundum, foramen ovale, foramen caroticum, canalis caroticus, canalis petrooccipitalis, foramen jugulare, canalis nervi hypoglossi, canalis nervi trigemini, foramen ethmoidale, meatus acusticus internus, meatus temporalis, foramen mastoideum, canalis sinus transversi, canalis condylaris, foramen magnum.

- Annotations in the ‘Other structures’ view: bulbus olfactorius, pedunculus olfactorius, fossa hypophysealis, regio dorsum sellae, lobus piriformis lobulus paramedianus cerebelli, lobulus ansiformis cerebelli, tuber vermis, fossa subarcuata, sulcus sinus petrosi dorsalis, line of a. basilaris, line of a. meningea media, line of a. cerebri media.

Finally, with the SLS technology the endocast was printed in its actual size using polyamide powder for the 3D printing, colorized with acrylic dye and varnish spray was applied for the surface treatment. This created a tangible object from the digital endocast (**Figure 54**).

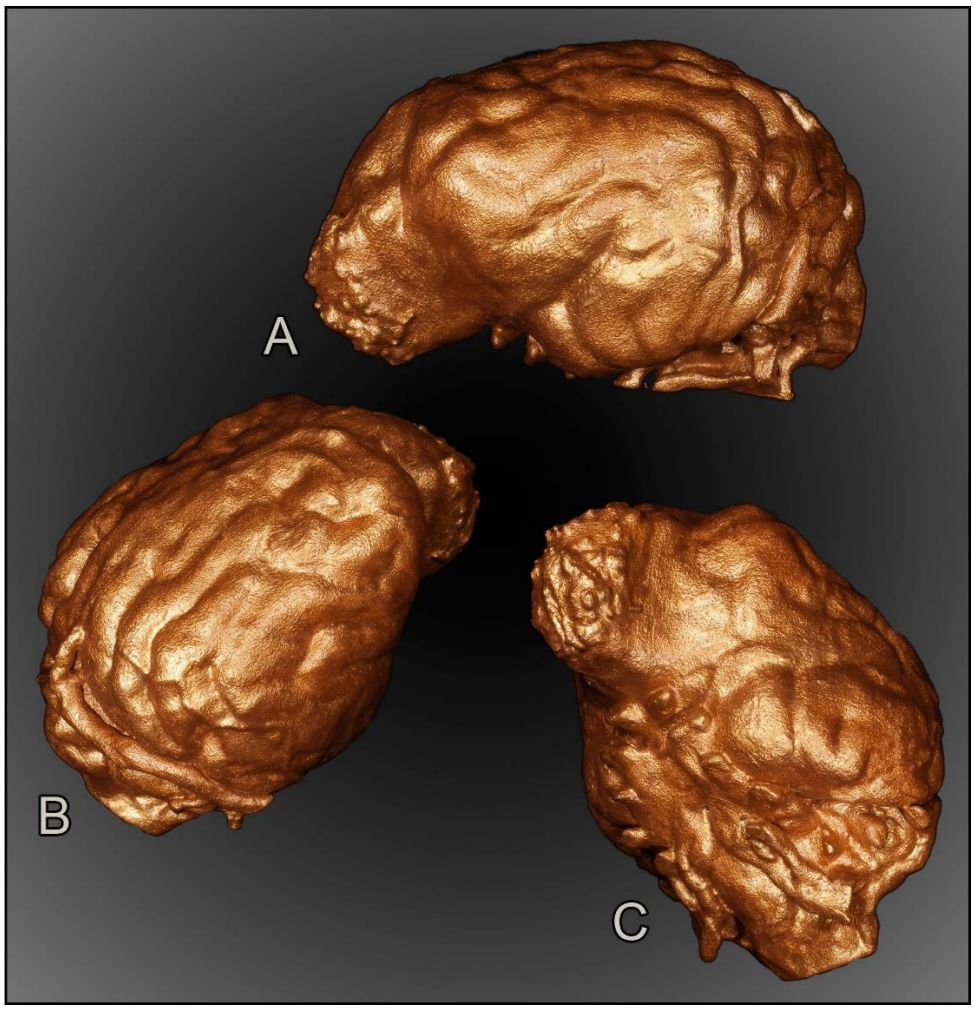

Figure 54. 3D-printed and colorized model of the beagle endocranial cast. A) Left lateral view. B) Right dorso-lateral view. C) Left ventro-lateral view.

5.4. Vascular 3-dimensional modelling and image fusion

Arteries and veins were segmented from the cryosectioned image volume, and separate 3D models were generated and transferred into a common space, showing differences between the detailed segmentations and when focusing only on the main branches (**Figure 55**). This can be best seen in the area of the lamina cribrosa, where the caudal septal nasal arteries (structure 25 in **Figure 55/A, C**) pass into the nasal cavity. In “A” and “C” parts of **Figure 55**, only the main contour of the ethmoidal fossa is highlighted by the larger vessels in the images, but in pictures in “B” and “D” parts the neighbouring small nasal branches are also visible.

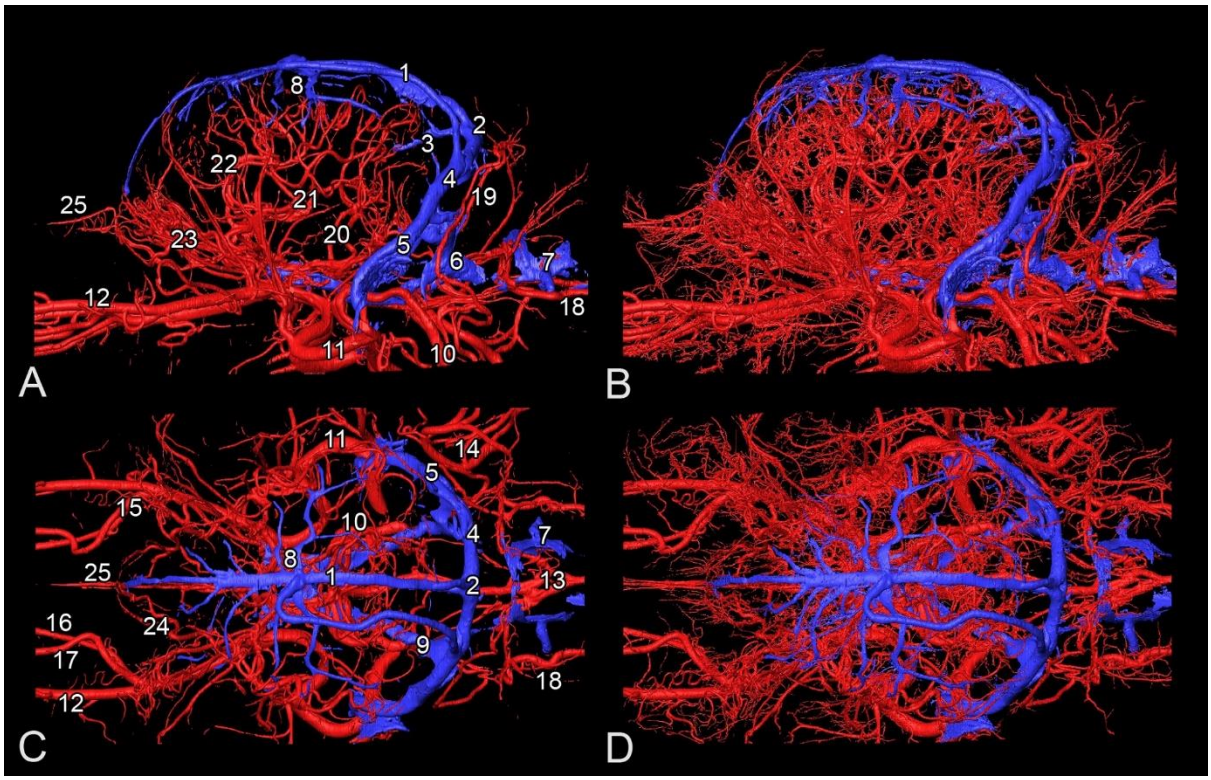

Figure 55. Arteries (in red) and veins (in blue) in the 3D model of the beagle head with different levels of detail. A, C) Basic model. B, D) Highly detailed model. A, B) Lateral view. C, D) Dorsal view. 1) Sinus sagittalis dorsalis. 2) Confluens sinuum. 3) Sinus rectus. 4) Sinus transversus. 5) Sinus temporalis. 6) Sinus sigmoideus. 7) Plexus vertebralis internus ventralis. 8) Vv. cerebri dorsales. 9) Sinus petrosus ventralis. 10) A. carotis interna. 11) A. maxillaris. 12) A. infraorbitalis. 13) A. spinalis ventralis. 14) A. auricularis caudalis. 15) A. palatina descendens. 16) A. palatina major. 17) A. sphenopalatina. 18) A. vertebralis. 19) Ramus occipitalis a. auricularis caudalis. 20) A. cerebri caudalis. 21) A. cerebri media. 22) A. cerebri rostralis. 23) Rami musculares et ciliares a. ophthalmicae externae. 24) A. ethmoidalis externa. 25) Aa. nasales septales caudales.

There were various multimodal visualisation possibilities as all the image volumes (RGB and greyscale-converted images, MR and CT series) and the 3D surface models were registered in the same coordinate system. These image volumes could be shown in any association with each other, thus providing an easier identification of the vessels in the greyscale-converted images (**Figure 56**). Additionally, by determining the shape and position of the arteries and veins, the tracking on the MR and CT imaging was more straightforward (**Figures 57** and **58**).

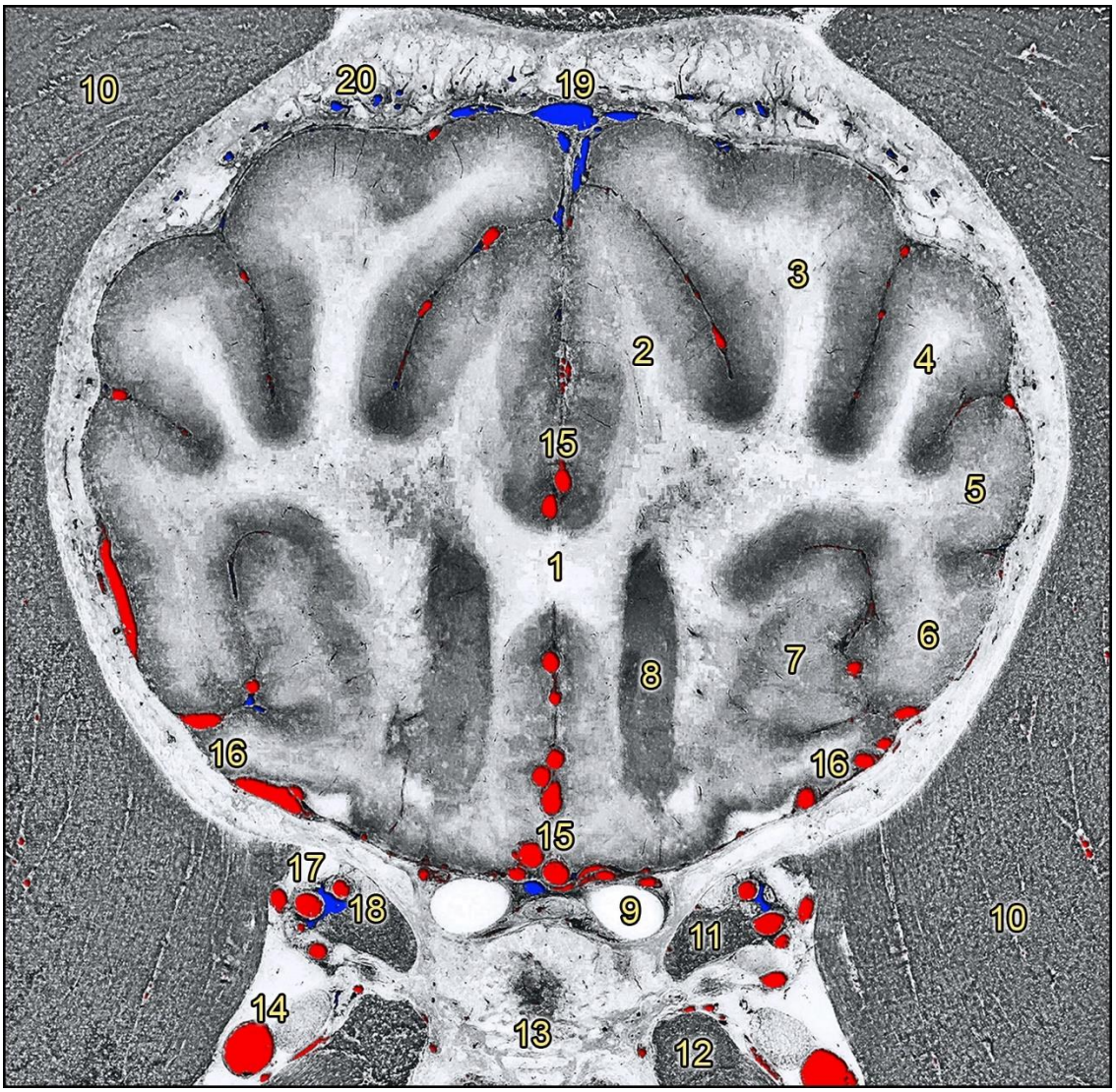

Figure 56. Transverse section at the level of the frontal lobe of the beagle head. Composite image with the greyscale-converted cryosectioned image and the colorized crossing vessels (arteries in red, veins in blue). 1) Corpus callosum. 2) Gyrus cinguli. 3) Gyrus postcruciatus. 4) Gyrus suprasylvius rostralis. 5) Gyrus ectosylvius rostralis. 6) Gyrus compositus rostralis. 7) Gyrus proreus. 8) Nucleus caudatus. 9) N. opticus. 10) M. temporalis. 11) Radices mm. bulbi. 12) M. pterygoideus medialis. 13) Corpus ossis presphenoidalis. 14) A. maxillaris. 15) Rami a. cerebri rostralis. 16) Rami a. cerebri mediae. 17) Rami a. ophthalmicae externae. 18) V. ophthalmica externa ventralis. 19) Sinus sagittalis dorsalis. 20) Vv. diploicae frontalis.

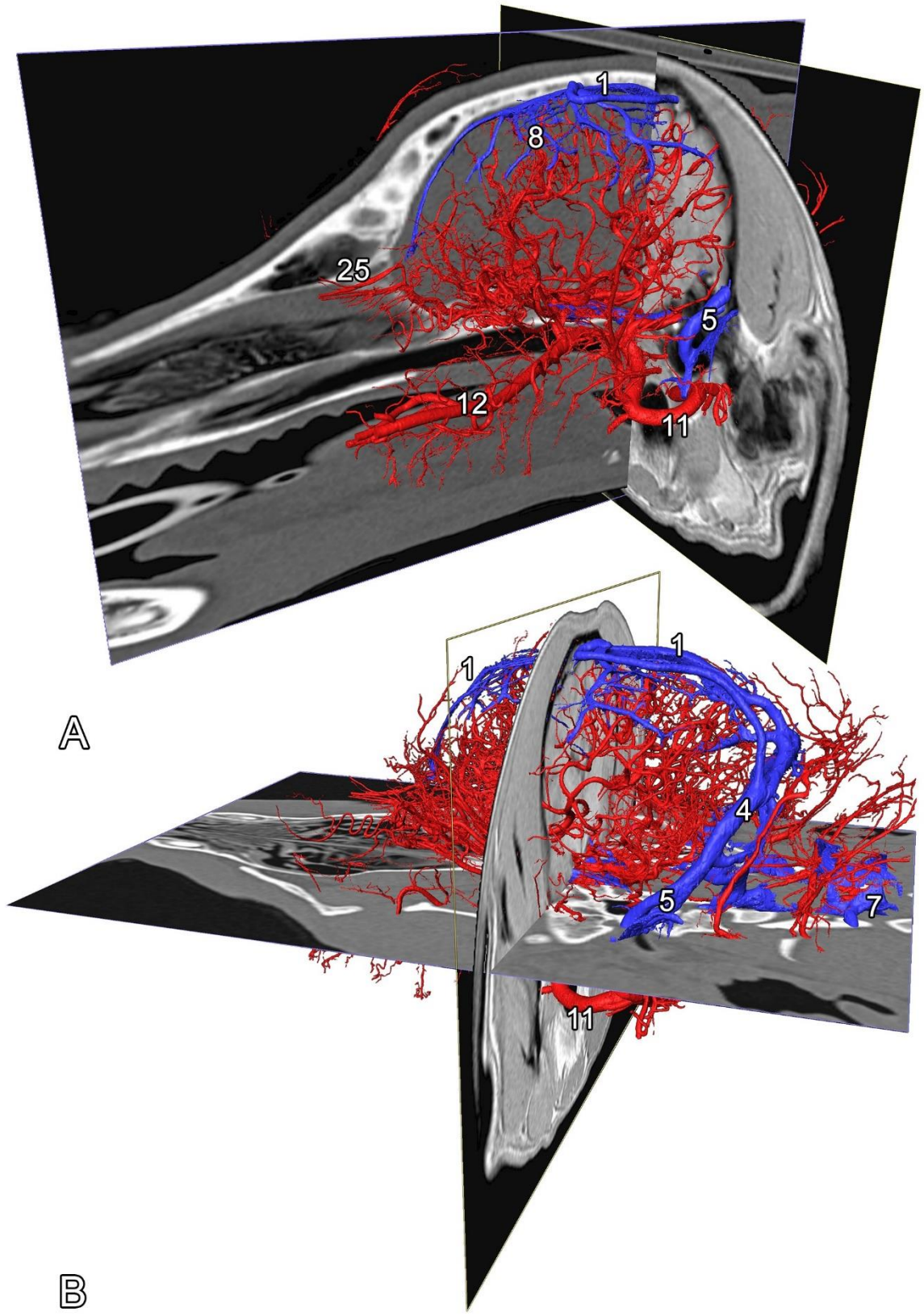

Figure 57. The different imaging modalities of the beagle head with the vascular models. Arteries in red, veins in blue. Numbers are according to **Figure 55.** A) 3D models with the transverse T1-weighted MR and sagittal CT images, left rostro-lateral view. B) 3D models with the transverse T1-weighted MR and dorsal CT images, left caudo-lateral view.

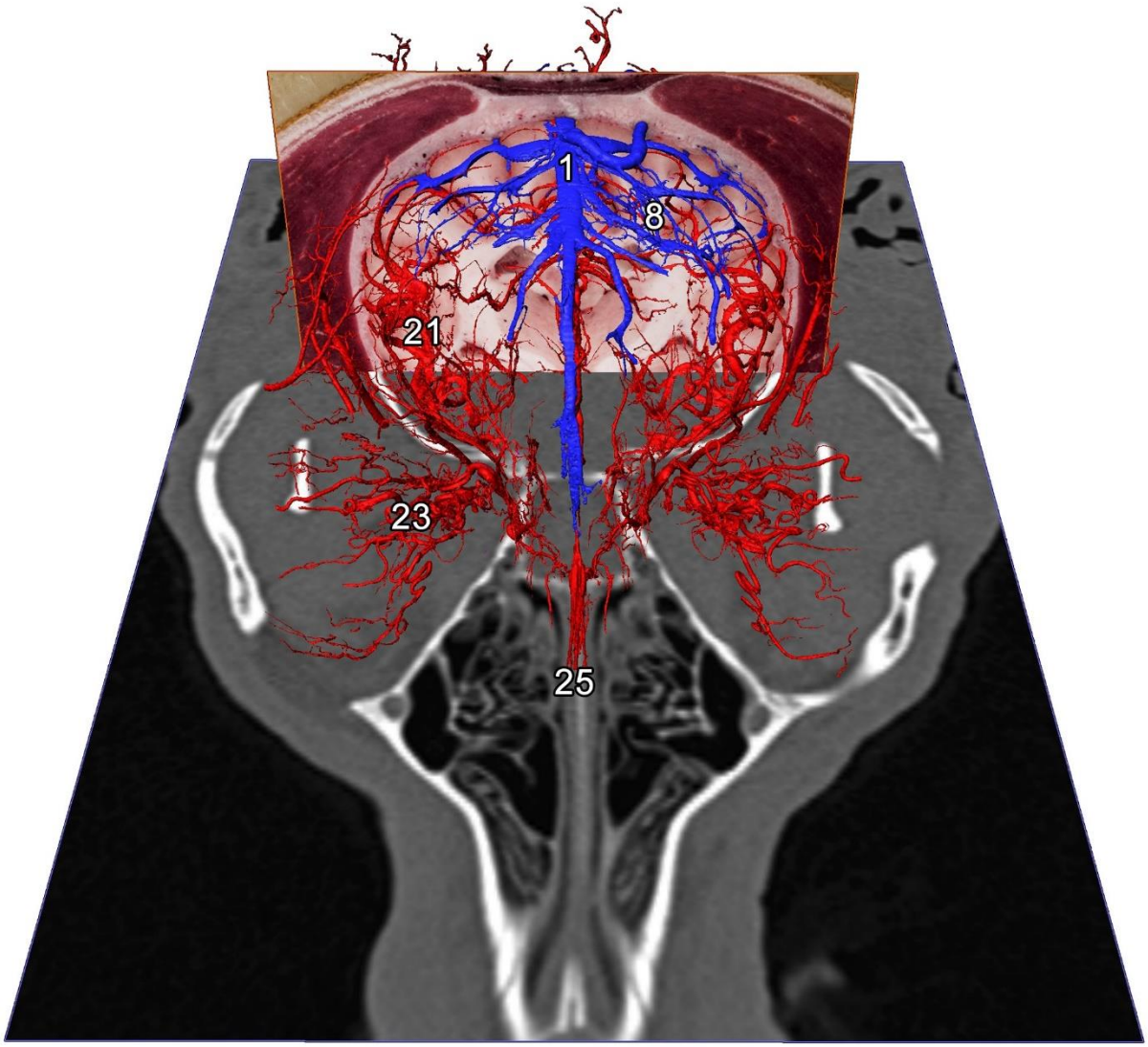

Figure 58. The different imaging modalities of the beagle head with the vascular models, rostro-dorsal view. Arteries in red, veins in blue. Numbers are according to **Figure 55.** Cryosectioned RGB image (in the transverse plane) and CT image (in the dorsal plane).

Finally, to provide further perspectives for the possible use of these types of datasets, we demonstrated how could the interactive use of the software allow to dynamically examine the subtracted and volume-rendered 3D models of the brain and its main supplying vessels: the volume and surface models could be cut in any orthogonal or oblique planes (**Figure 59**). By choosing an optional coordinate point inside the brain, all of the three main imaging modalities could be visualised in different planes in the 3D model of the skull (**Figure 60**). In this way, inspection of any neurocranial structures is possible by changing the slice number and switching between the planes and the imaging modalities.

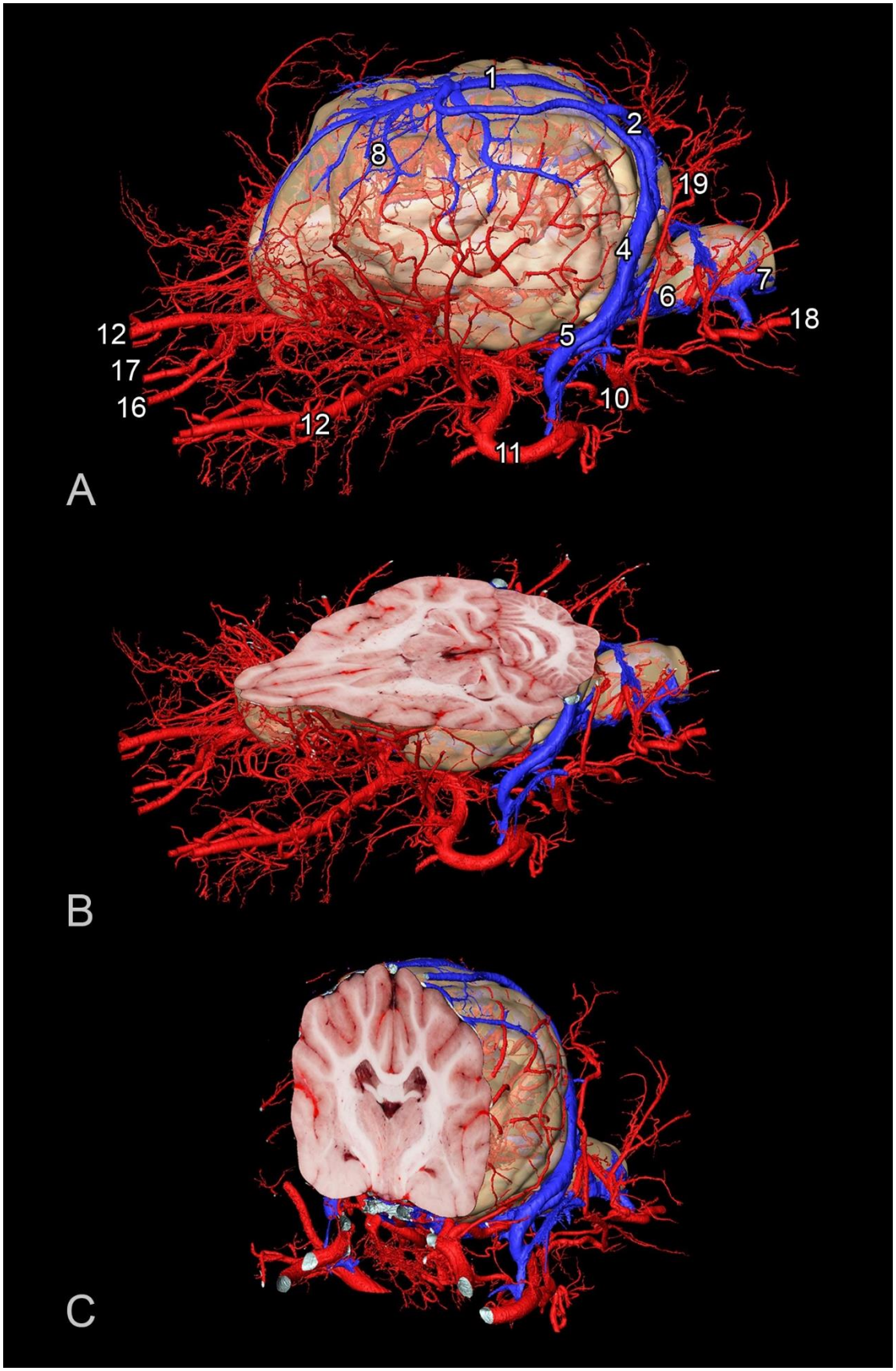

Figure 59. 3D models of the vessels and the extracted beagle brain. Arteries in red, veins in blue. Numbers are according to **Figure 55.** A) Vessels with complete brain. B) Models were cut in the dorsal plane. C) Models were cut in the transverse plane.

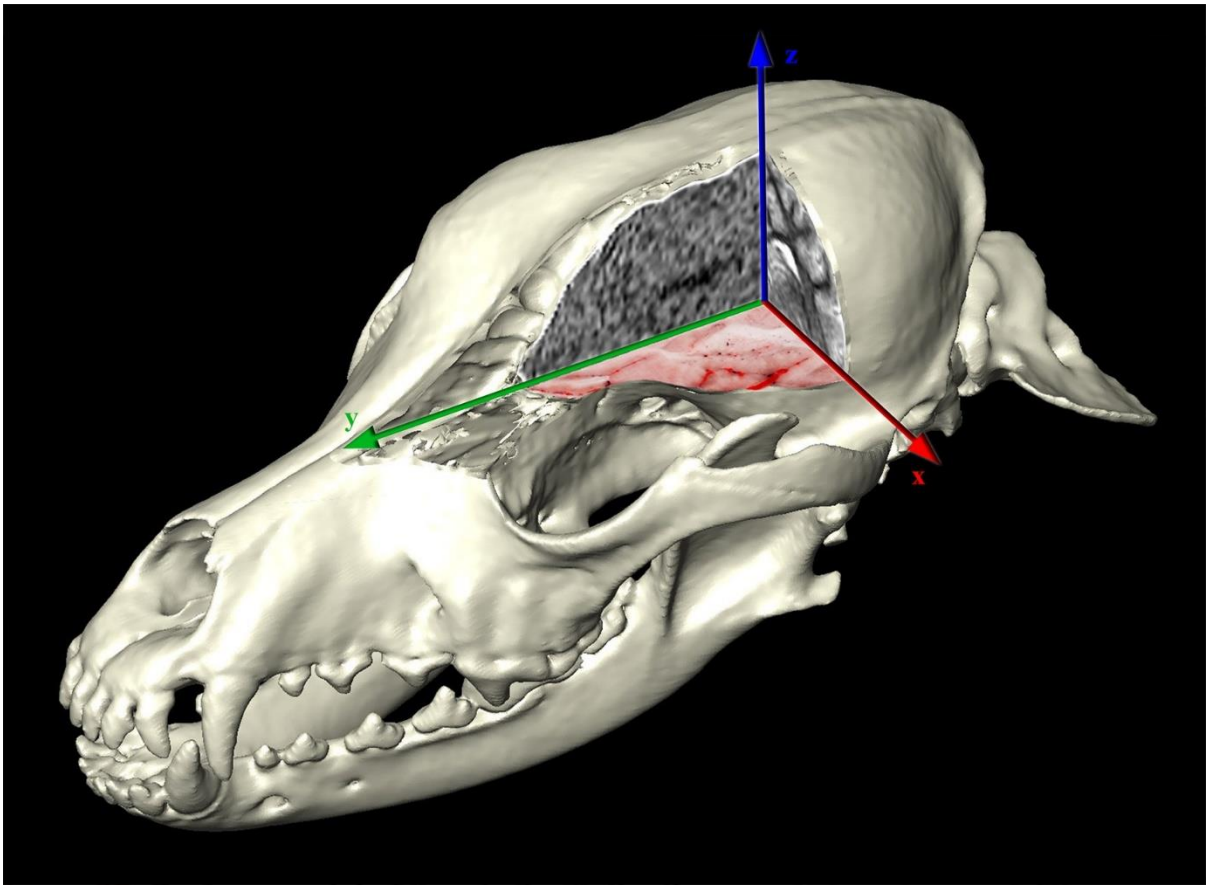

Figure 60. 3D model of the beagle skull with the three main imaging modalities presented in the different orthogonal planes. CORE–RGB image in the dorsal plane, T2-weighted MR image in the transverse plane, and CT image (with brain kernel) in the sagittal plane.

5.5. Labelled anatomical illustrations

The high-resolution images from the original transverse plane and the from the CORE sagittal and dorsal planes, together with the structural imaging data (CT with bone and brain kernels, T2-weighted MR image) and surface models gave us the possibility to present the annotated images like in a neuroanatomy atlas. On the following pages three pairs of cryosectioned RGB images and their corresponding data show this concept. To keep the integrity of the colorized pictures (avoiding to put numbers/arrows on the top of them, which would cover the underlying structures), we decided to make greyscale copies from the RGB images, and to place them to the adjacent pages with the figure legends. In this way one can easily identify the localisation of the presented cryosectioned slices based on the guide on the endocasts; the corresponding MR and CT images can be seen, and a detailed annotation provides an effective help in the identification of the individual anatomical structures (**Figures 61, 62, 63, 64, 65** and **66)**.

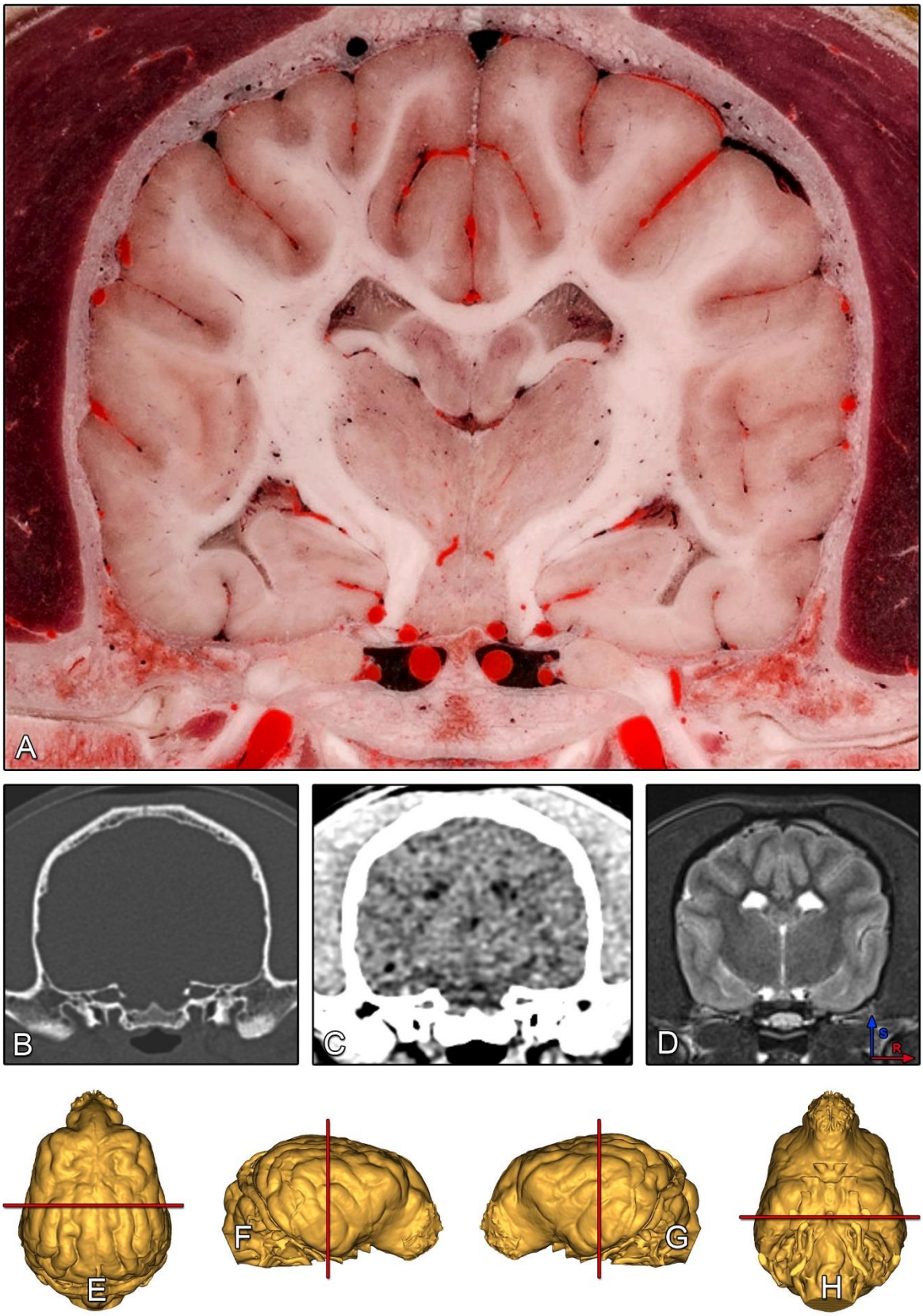

Figure 61. Transverse section at the level of the mammillary body. A) Original RGB image. B) CT image with bone kernel. C) CT image with brain kernel. D) T2-weighted MR image. The level of section is shown on the 3D endocast model of the beagle with red lines. E) Dorsal view. F) Right lateral view. G) Left lateral view. H) Ventral view.

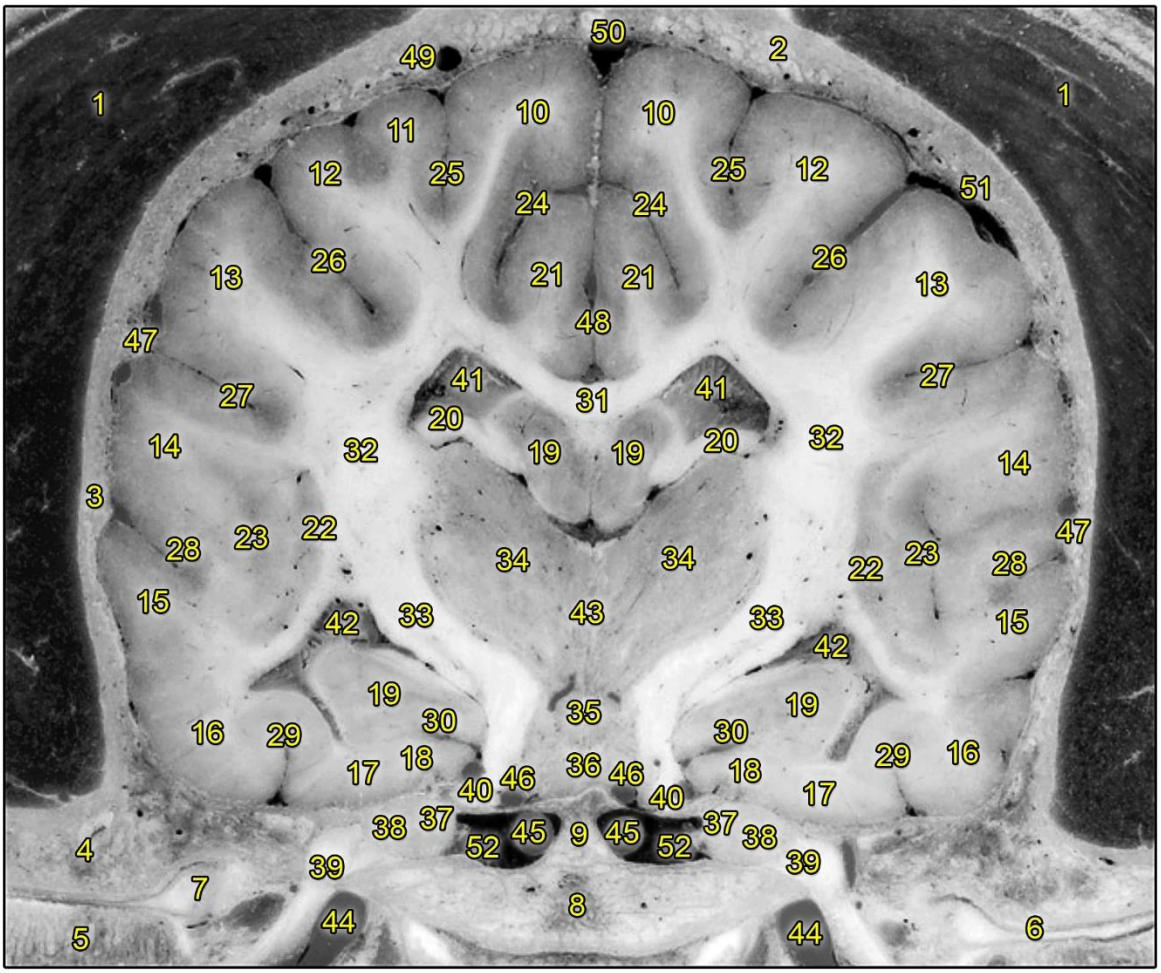

1) M. temporalis
2) Os parietale
3) Pars squamosa ossis temporalis
4) Processus zygomaticus ossis temporalis
5) Caput mandibulae
6) Articulatio temporomandibularis
7) Discus articulationis temporomandibularis
8) Corpus ossis basisphenoidalis
9) Dorsum sellae
10) Gyrus marginalis
11) Gyrus ectomarginalis
12) Gyrus suprasylvius medius
13) Gyrus ectosylvius medius
14) Gyrus sylvius caudalis
15) Gyrus ectosylvius caudalis
16) Gyrus compositus caudalis
17) Gyrus parahippocampalis
18) Subiculum
19) Hippocampus
20) Crus fornicis
21) Gyrus cinguli
22) Claustrum
23) Cortex insularis
24) Sulcus splenialis
25) Sulcus marginalis
26) Sulcus suprasylvius medius
27) Sulcus ectosylvius medius
28) Sulcus ectosylvius caudalis
29) Fissura rhinalis lateralis, pars caudalis
30) Sulcus hippocampi
31) Corpus callosum
32) Centrum semiovale
33) Capsula interna
34) Thalamus
35) Hypothalamus
36) Corpus mamillare
37) N. ophthalmicus
38) N. maxillaris
39) N. mandibularis
40) N. oculomotorius
41) Ventriculus lateralis, pars centralis
42) Ventriculus lateralis, cornu temporale
43) Adhesio interthalamica
44) A. maxillaris
45) A.carotis interna
46) A. communicans caudalis
47) Rami a. cerebri mediae
48) Rami a. cerebri rostralis
49) V. diploica parietalis
50) Sinus sagittalis dorsalis
51) V. cerebri dorsalis
52) Sinus cavernosus

Figure 62. Greyscale-converted reference image of **Figure 61**, with annotations.

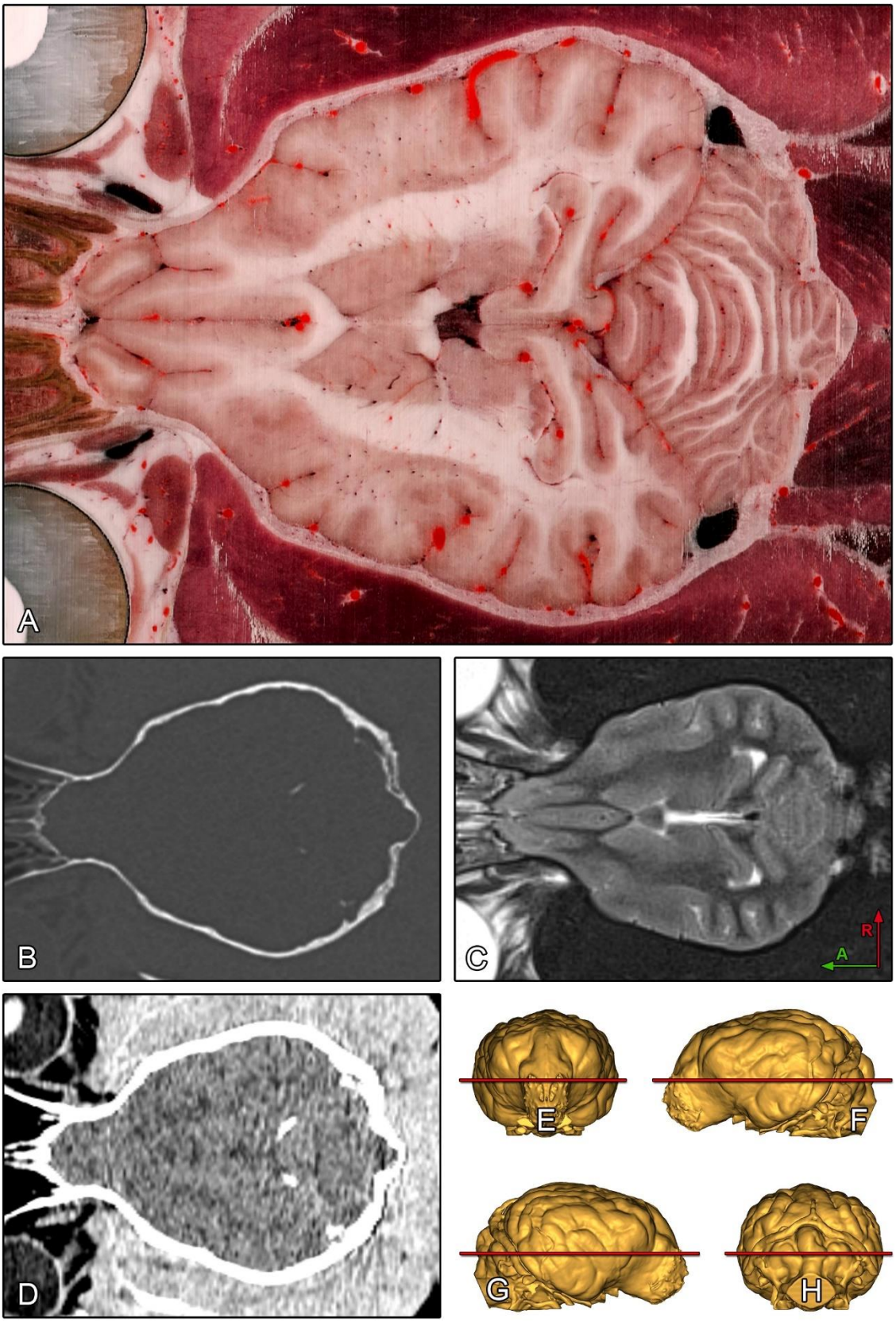

Figure 63. Dorsal section at the level of the rostrum corporis callosi. A) CORE–RGB image. B) CT image with bone kernel. C) T2-weighted MR image. D) CT image with brain kernel. The level of section is shown on the 3D endocast model of the beagle with red lines. E) Rostral view. F) Left lateral view. G) Right lateral view. H) Caudal view.

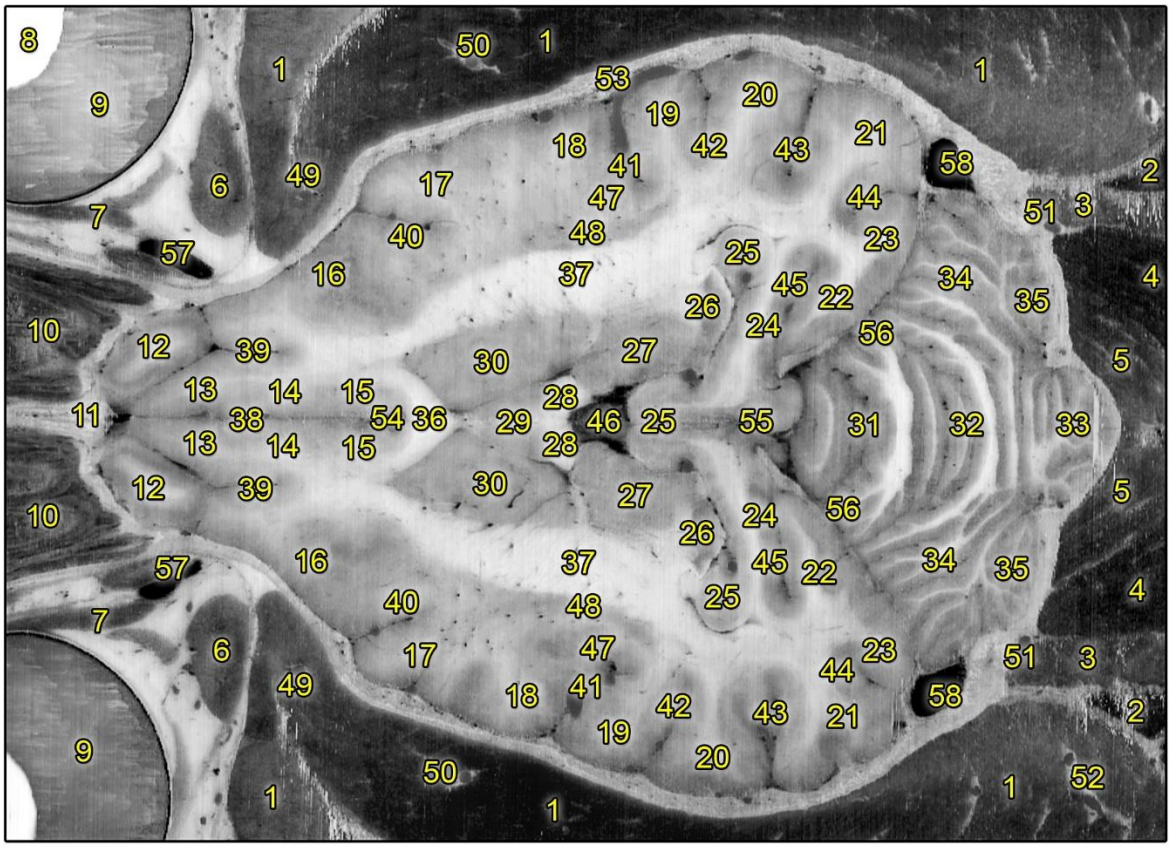

1) M. temporalis
2) M. splenius
3) M. obliquus capitis cranialis
4) M. obliquus capitis caudalis
5) M. rectus capitis dorsalis major
6) M. rectus dorsalis
7) M. rectus medialis
8) Lens
9) Corpus vitreum
10) Ethmoturbinalia
11) Lamina cribrosa
12) Bulbus olfactorius
13) Gyrus frontalis
14) Gyrus genualis
15) Gyrus cinguli
16) Gyrus proreus
17) Gyrus compositus rostralis
18) Gyrus sylvius rostralis
19) Gyrus sylvius caudalis
20) Gyrus ectosylvius caudalis
21) Gyrus suprasylvius caudalis
22) Gyrus splenialis
23) Gyrus occipitalis
24) Gyrus parahippocampalis
25) Hippocampus
26) Corpus geniculatum laterale
27) Thalamus
28) Columna fornicis
29) Area septalis
30) Nucleus caudatus
31) Culmen
32) Vermis cerebelli
33) Tuber vermis
34) Lobulus ansiformis, crus rostrale
35) Lobulus ansiformis, crus caudale
36) Rostrum corporis callosi
37) Centrum semiovale
38) Fissura longitudinalis cerebri
39) Sulcus proreus
40) Sulcus presylvius
41) Fissura pseudosylvia
42) Sulcus ectosylvius caudalis
43) Sulcus suprasylvius caudalis
44) Sulcus ectomarginalis
45) Sulcus retrosplenialis
46) Ventriculus tertius
47) Cortex insularis
48) Claustrum
49) A. temporalis profunda rostralis
50) A. temporalis profunda caudalis
51) A. occipitalis
52) R. muscularis a. auricularis caudalis
53) Rami a. cerebri mediae
54) Rami a. cerebri rostralis
55) Rami a. cerebri caudalis
56) Rami a. cerebelli rostralis
57) Plexus ophthalmicus
58) Sinus temporalis

Figure 64. Greyscale-converted reference image of **Figure 63**, with annotations.

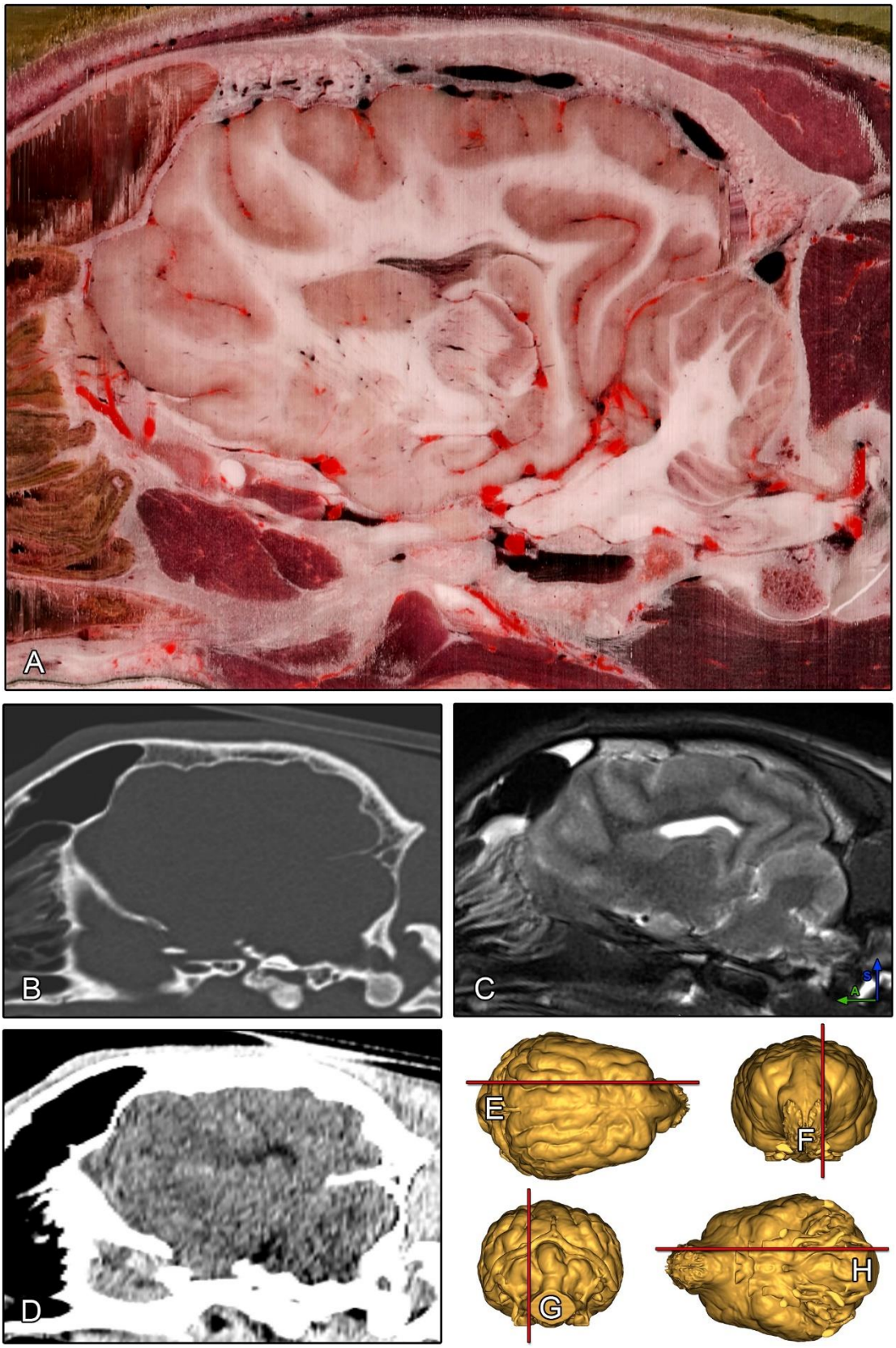

Figure 65. Sagittal section at the level of the lateral geniculate body. A) CORE–RGB image. B) CT image with bone kernel. C) T2-weighted MR image. D) CT image with brain kernel. The level of section is shown on the 3D endocast model of the beagle with red lines. E) Dorsal view. F) Rostral view. G) Caudal view. H) Ventral view.

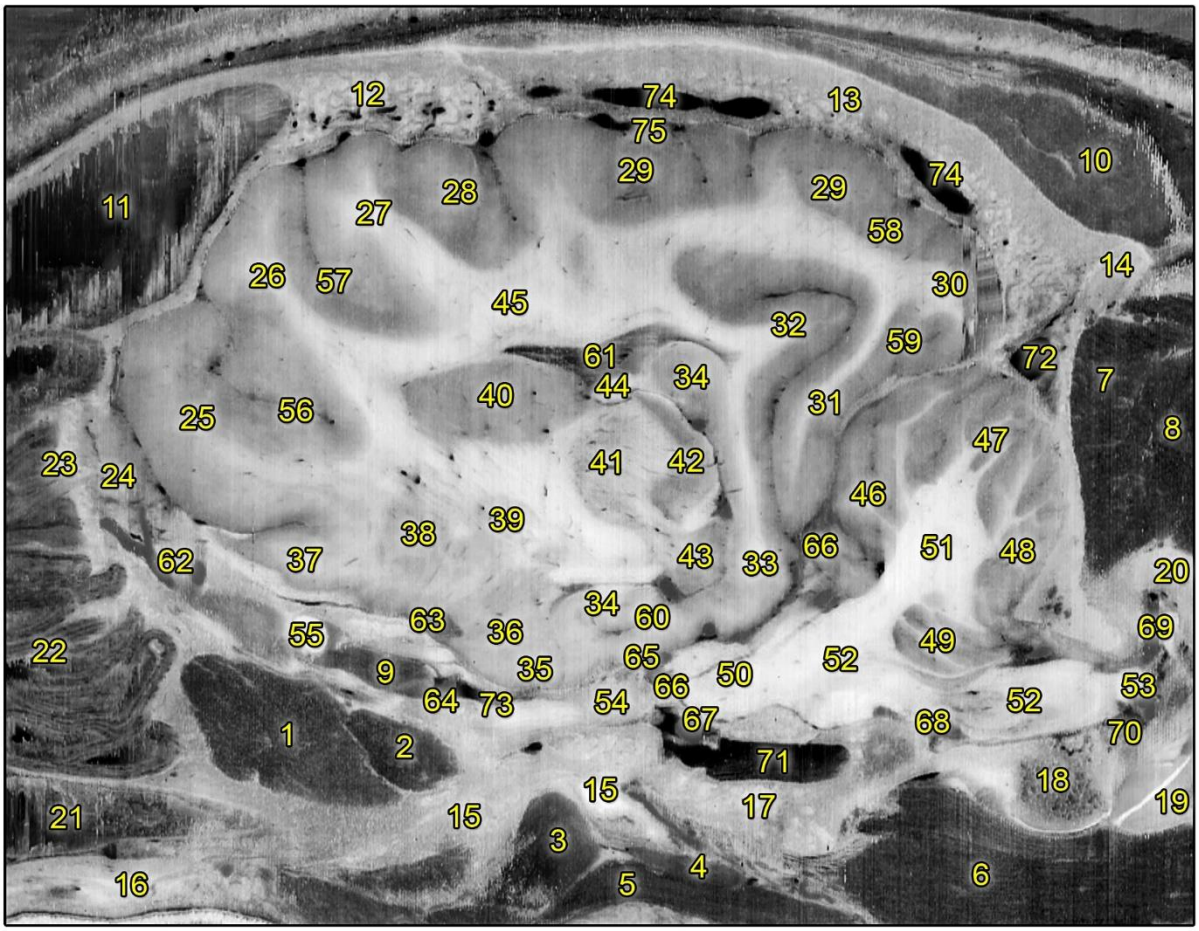

1) M. pterygoideus medialis
2) M. pterygoideus lateralis
3) M. tensor veli palatini
4) M. levator veli palatini
5) M. pterygopharyngeus
6) M. longus capitis
7) M. rectus capitis dorsalis major
8) M. obliquus capitis caudalis
9) M. retractor bulbi
10) M. temporalis
11) Sinus frontalis
12) Os frontale
13) Os parietale
14) Crista nuchae
15) Processus pterygoideus
16) Palatum durum
17) Os basioccipitale
18) Condylus occipitalis
19) Arcus ventralis atlantis
20) Arcus dorsalis atlantis
21) Meatus nasopharyngeus
22) Ethmoturbinalia
23) Lamina cribrosa
24) Bulbus olfactorius
25) Gyrus proreus
26) Gyrus precruciatus
27) Gyrus postcruciatus
28) Gyrus suprasylvius rostralis
29) Gyrus ectomarginalis
30) Gyrus occipitalis
31) Gyrus splenialis
32) Gyrus cinguli
33) Gyrus parahippocampalis
34) Hippocampus
35) Lobus piriformis
36) Amygdala
37) Pedunculus olfactorius
38) Putamen
39) Pallidum
40) Nucleus caudatus
41) Thalamus
42) Corpus geniculatum laterale
43) Corpus geniculatum mediale
44) Crus fornicis
45) Centrum semiovale
46) Lobulus quadrangularis
47) Lobulus ansiformis, crus rostrale
48) Lobulus paramedianus
49) Flocculus
50) Pedunculus cerebellaris medius
51) Corpus medullare cerebelli
52) Medulla oblongata
53) Medulla spinalis
54) N. ophthalmicus
55) N. opticus
56) Sulcus presylvius
57) Sulcus cruciatus
58) Sulcus marginalis
59) Sulcus occipitotemporalis
60) Sulcus hippocampi
61) Ventriculus lateralis
62) A. ethmoidalis externa
63) A. cerebri media
64) A. ophthalmica externa
65) A. cerebri caudalis
66) A. cerebelli rostralis
67) A. carotis interna
68) A. basilaris
69) R. spinalis a. vertebralis
70) Plexus vert. int. ventralis
71) Sinus petrosus ventralis
72) Sinus transversus
73) V. emiss. fissurae orbitalis
74) V. diploica parietalis
75) V. cerebri dorsalis

Figure 66. Greyscale-converted reference image of **Figure 65**, with annotations.

6. Discussion

6.1. Assessment and comparison

One of the main advantages of the cryosectioning is that any region of the body can be studied regardless of the tissue composition, including thick bones that can be easily cut. Therefore, high-resolution RGB images can be obtained, and if the layer thickness is small enough, multiplanar reconstructions can be made in any arbitrary plane using specially designed software (e.g., Amira or 3D Slicer). When structural imaging techniques (MR, CT) are associated, the volumes can be registered together; thus, multimodal atlases can be easily generated in the same coordinate system. Antemortem functional studies, tractography of the neural pathways (diffusion tensor imaging, DTI), PET and SPECT imaging can also be carried out prior to cryosectioning. The segmentation of individual structures or systems makes it possible to create 3D models that are beneficial for several fields; these include education (e.g., to help understand the relationship between a 2D image series and a 3D structure), research (comparative neuroanatomy) and clinical work (reference atlases for studying the different brain regions during surgical planning). In the current final study the brain was not removed from the neurocranial cavity, which is usually required to allow histological or macroscopic slicing (Palazzi, 2011; Thomson & Hahn, 2012), although based on these results the milling can be combined later with *in situ* perfusion techniques (Annese et al., 2006; Augulis & Sigg, 1971; Gasteiger et al., 1969). The cryosectioned structures can be seen in their original position (depending on the occurrence of freezing expansion or shrinkage) in relation to the surrounding structures. For example, the vessels and nerves around the brain can be traced around and through the osseous structures where they leave the skull. As no fixative agent was used in our study, and only the arteries were filled with red polyurethane (without producing extravasates), all the tissues can be seen in their original colour (the latter was also ensured by using a colour checker passport).

The time required for the entire process can be divided into three main phases: pre-sectioning, sectioning and post-sectioning. (1) The pre-sectioning part included the implementation of the diagnostic imaging techniques (e.g., CT and MRI), freezing the body and blocking the region of interest, constructing the embedding device, establishing the angle of cut in accordance with the orthogonal plane of the imaging techniques (so the milled surface can be parallel with them) and embedding the block. (2) The cryosectioning part comprised the preparation of the milling device, cooling equipment, DSLR camera and computer systems, and recording the images. (3) The post-sectioning workflow covered the photographic post-processing (e.g., setting the colour balance based on the colour checker, equalizing shadows and generating

JPEG or TIFF images from the raw CR2 image series), and depending on the aim of the study, the image analysis or 3D modelling, which consists of the volume registration, segmentation and 3D modelling work at the required level of detail. The time of the workflow is affected by the number of people who contribute to the research (e.g., in the case of multiple species, organising parallel workflows is advised) and any stops during the cryosectioning. In our case the milling procedure of the beagle neurocranium in the final study took approximately 40 hours. The pre-sectioning work required two weeks, and photo-conversion of the images took three days. The post-sectioning image analysis and 3D modelling work solely depends on the research goals (e.g., the number of modelled structures and the required level of detail) and on the number of people working simultaneously on the project.

Known technological limitations mostly relate to the milling device and the cooling process. There are no technical limitations regarding the species, as any tissue can be sectioned by the milling device, which was originally designed to work with metals, therefore even sites with surgical implants could be cryosectioned. If the block is too large it can be divided into smaller parts, as was done during the Visible Human Project (Spitzer et al., 1996). Imbalanced cooling can cause artefacts, including discoloration, surface freeze lines or expansion/shrinkage of the tissue. The 100 µm layer thickness can be still reduced, as the milling device is capable of working at a 1 µm precision level with metals. However, the expansion (due to the heat originating from the milling) and the refreezing (after capturing the surface, prior to the next sectioning) can cause not only temperature fluctuations but also uneven freezing and discoloration of the surface based on tissue quality. Thus, sectioning at less than 20–30 µm can lead to challenges with the cryomacrotomisation process if no prior tissue fixative and/or cryoprotective agent is used. Because the block is destroyed during the milling procedure (as the device is carving down the block layer by layer), the sectioned tissue cannot be used for other purposes after cryomacrotomisation. Theoretically, the achievable resolution is very high, because a high-quality DSLR camera sensor not only captures the overall surface, but the surface can be subdivided into four, twenty or hundreds of smaller regions to be captured individually. Thus, one surface can be merged from several regions, so the resolution of the final image (even with the same camera) will increase. Consequently, the pixel per centimetre ratio can be increased and is only limited by the intentions of the researcher. During the post-processing work, the limits of the segmentation depend on: (a) the original image resolution (the smaller the pixel to µm ratio, the smaller the structure that can be identified); (b) the contrast of the tissues (e.g., between the vessels and their environment, thus the brightest and the most non-tissue coloured resins should be used); (c) the efficiency of vascular filling with the polymer; and finally (d) the computer's capacity, as the hardware should be capable of dealing with large datasets (e.g., tens of gigabytes) during the computational process.

Compared to other projects that have aimed to section dogs (Böttcher et al., 1999; Park et al., 2014) and a cat (Chung et al., 2018), we obtained a higher resolution and a more detailed RGB image series from the region of interest (ROI). This was achieved due to the following factors: (a) we focused entirely on cryosectioning the neurocranium with the brain, whilst other authors sectioned and captured entire cadavers; therefore, our ROI for the head was smaller; (b) our slice interval was 0.1 mm compared to 0.2 mm (Chung et al., 2018; Park et al., 2014) or 1 mm (Böttcher et al., 1999); (c) the resolution of our images was higher, at 7360×4912 pixels compared to 5616×3328 pixels (Chung et al., 2018; Park et al., 2014) or 1928×1459 pixels (Böttcher et al., 1999); (d) the pixel size was 19.5×19.5 µm compared to 100×100 µm (Chung et al., 2018; Park et al., 2014) or 180×180 µm (Böttcher et al., 1999); (e) we used colouring agent only for the arteries, which did not affect the other tissues compared to the formalin-fixation method used previously (Böttcher et al., 1999); and (f) discoloration of the brain or freeze lines inside the brain did not occur compared to other studies (Chung et al., 2018). Progress has been made regarding image recording, because the research group who performed the cat cryosectioning (Chung et al., 2018) recently conducted a cryomacrotomisation study on a Rhesus monkey, where they sectioned the entire body with a 0.05 mm slice interval for the head and 0.5 mm intervals for the rest of the body, recording the transverse surface of the block at a 8688×5792 pixel resolution and a 24×24 µm pixel size (Chung et al., 2019).

Other canine brain and head atlases show the histological aspect of the brain, thus *ex situ* slicing was conducted and tissue staining was applied (Adrianov & Mering, 2010; Dua-Sharma et al., 1971; Fletcher & Saveraid, 2009; Lim et al., 1960; Palazzi, 2011; Singer, 1962). In our study, we did not apply any tissue staining except for colouring the arterial system; hence, the tissues showed their original colour, and the outline of the grey matter and the position of the major subcortical nuclei could still be distinguished (as seen in **Figure 47**). We wanted to show the brain in its *in situ* position, with it possible to trace the surrounding vessels, the cranial nerves, the skull and the associated structures. Other studies have also structurally imaged the canine head and brain, from just a few sections of the canine head and brain for demonstrational purposes with MRI (Hage et al., 2010; Hartmann et al., 2014; Kang et al., 2009; Kraft et al., 1989; Martín-Vaquero et al., 2011), CT (Fike et al., 1981; Kaufman et al., 1981) or ultrasonography (Cintra et al., 2014; Hudson et al., 1989), to detailed anatomical marking of the MRI images (Fletcher & Saveraid, 2009; Leigh et al., 2008; Schmidt & Kramer, 2015), using both MR and CT imaging of the brain (Assheuer & Sager, 1997), and the creation of different MRI brain templates from breed-averaged data (Datta et al., 2012; Nitzsche et al., 2018). In two other studies the brain was removed for sectioning without performing previous diagnostic imaging. In the first study, 4 mm thick transverse and sagittal plastinated slices

were made from the brain (Frohlich et al., 2003). In the second study, surface photographs and 18 transverse slices were created following formalin fixation (Thomson & Hahn, 2012). The advantage of making a cryosectioned series from a single individual who underwent prior diagnostic imaging is that these images are directly comparable to each other. Due to the small slice thickness and the fact that the image volume can be reconstructed in any arbitrary plane, our image volume could also serve as a visual aid to assist in the interpretation of previous studies if the proper slice is chosen from the beagle brain series. Studies that performed both diagnostic imaging and tissue sectioning of the canine head and brain include: (a) head CT with *in situ* sectioning of the entire head, with a slice thickness of 8 mm (George & Smallwood, 1992); (b) CT performed with *ex situ* brain slicing, creating 17 transverse sections with a 5 mm interval (De Rycke et al., 2005); (c) *in situ* formalin-fixed sectioning with 9 transverse head sections (four of which included the brain), with two transverse and one sagittal MR images (Done et al., 2009); (d) *ex situ* formalin-fixed and stained sectioning with previous CT imaging, resulting in 9 transverse sections of the brain (Nakade et al., 2003); (e) *ex situ*, formalin-fixed and histologically stained brain sections with previous MR imaging, producing 12 transverse sections (thickness of 3 to 10 mm), and three of the brain slices were correlated with the MR images (Mogicato et al., 2011); (f) *ex situ* formalin-fixed brain slicing with prior MR and CT imaging, where 9 transverse, 4 dorsal and 3 sagittal images were compared between the three methods (Jaggy & Couteur, 2010); and (g) *in situ* formalin-fixed sectioning of the entire head, with previous CT and MR imaging, creating 18 transverse sections of the entire head, which comprised 8 transverse sections where the brain could be seen (Gomercic et al., 2009).

By comparing our dataset to these previous studies, the advantages and novelties of the current cryomacrotomisation study are:

- we used only one dog to obtain all the diagnostic and cryosectioned images;
- we performed both CT and MR scanning;
- we repeated the MR imaging postmortem to have comparative data for checking the possible antemortem and postmortem changes;
- we did not use formalin fixation or dyes in order to see the original tissue colour;
- there was no need to remove the brain for sectioning or to decalcify the bones;
- we focused the complete process (blocking, embedding, cryomacrotomisation, photography and image analysis) on the neurocranium and the brain only;
- we used image capturing with a high level of detail (24-bit colour depth, 300 DPI, 7360×4912 pixels and a pixel size of 19.5×19.5 µm);
- we obtained sectioning intervals of only 100 µm;

- originally, 1112 sections of the neurocranium were made in the transverse plane, but due to the small voxel size and with the software-based volume rendering, detailed images in any other orthogonal or oblique plane could be created (as **Figure 48** shows) or volume can be resampled with an optional slice interval;
- the registration of the cryosectioned volume with the MR and CT data provided directly comparable images (shown in **Figure 49** and in **Figures 61–66**);
- segmentation of the anatomical structures and 3D reconstruction can be carried out and used on their own or merged with the 2D imaging data;
- after normalisation to another image volume, the results are comparable with previous studies, and subsequent imaging surveys can be integrated (e.g., matching with a cryosectioned brain where cryoprotection is used).

Development in the area of conventional image analysis and 3D image fusion is essential as diagnostic imaging methods gain more importance in small animal veterinary medicine (Dennis, 1998; Gavin, 2011) and in fMRI studies (Bunford et al., 2017). The canine brain has previously been examined with CT and MRI in several studies in the recent decades (Couturier et al., 2005; Hecht et al., 2019; Kärkkäinen et al., 1991; Kraft et al., 1989; Leigh et al., 2008; Martín-Vaquero et al., 2011) and has been presented in textbooks (Elliott & Skerritt, 2010; Gavin & Bagley, 2009; Wisner & Zwingenberger, 2015) and in histological (Palazzi, 2011) and diagnostic imaging atlases (Assheuer & Sager, 1997; Datta et al., 2012; Gomercic et al., 2009; Mai, 2018; Nitzsche et al., 2018; Schmidt & Kramer, 2015). Furthermore, due to similarities in development, aging and comorbidity between humans and dogs, investigations have recently focused on the canine central nervous system (Adams et al., 2000; Cotman & Head, 2008; Datta et al., 2012; Head, 2013; Su et al., 1998), and veterinary educational modules have also been published to aid in graduate learning (Christ et al., 2018; Raffan et al., 2017). Compared to the previously mentioned studies, one of the advantages of our 3D modelling methodology is that the created structures are more realistic due to the higher level of detail and surface morphology because of the original high-resolution cryosectioned images. Using the dog as a good translational model for human research is increasingly accepted (Andics et al., 2014; Andics & Miklósi, 2018; Bunford et al., 2017; Cotman & Head, 2008; Head, 2013; Khanna et al., 2006). Canine cognitive dysfunction (CCD) syndrome (Landsberg et al., 2017, 2012; Madari et al., 2015) also has some characteristics that are analogous to the early stages of human Alzheimer's disease, which indicates dogs as a promising model to more comprehensively study this disorder. It is expected that the role of dogs in comparative research will continue to grow, and therefore the need for accurate and detailed macro- and microanatomical canine brain atlases and imaging templates will also increase.

6.2. Practical benefits of the research

The knowledge derived from the cryosectioning techniques, the neuroanatomical insights obtained, and the practice with different visualisation software were advantageous for various fields, as summarized below in four sections.

6.2.1. Anatomy and 3D visualisation

We conducted the experiments regarding the cryosectioning technique and its comparison to structural imaging methods while keeping in mind which fields it could be successfully applied to. In addition to conference presentations (see details in section 9.4) and publications (Czeibert et al., 2019b, 2018; Petneházy et al., 2018b, 2018a), illustrations were made for both anatomy atlases and book chapters (Bajzik et al., 2015; Czeibert et al., 2015; Fenyves & Szentpétery, 2018; Singh, 2018) (**Figure 67**). Furthermore, as the potential of this method was acknowledged by the experts in the medical field, under a framework of cooperation with human anatomists at Semmelweis University, we carried out pilot studies that will potentially serve as an aid in rheumatology and ophthalmology (Baksa et al., publication in progress). In addition to these, developments in computer science have made it commercially possible to integrate 3D models into virtual, augmented or mixed reality technologies, which may have an important role in future research, education and medical applications (Kim et al., 2017; Samadbeik et al., 2018). In cooperation with an information technology (IT) developer group, we have begun to investigate the possibilities of the mixed reality technology by implementing the cat head slice series (from Study III) and the beagle dataset (from the final study) into a Microsoft Hololens system (https://www.microsoft.com/en-us/hololens), and we are working on its future IT applications which can support the medical and academic fields (**Figure 68**).

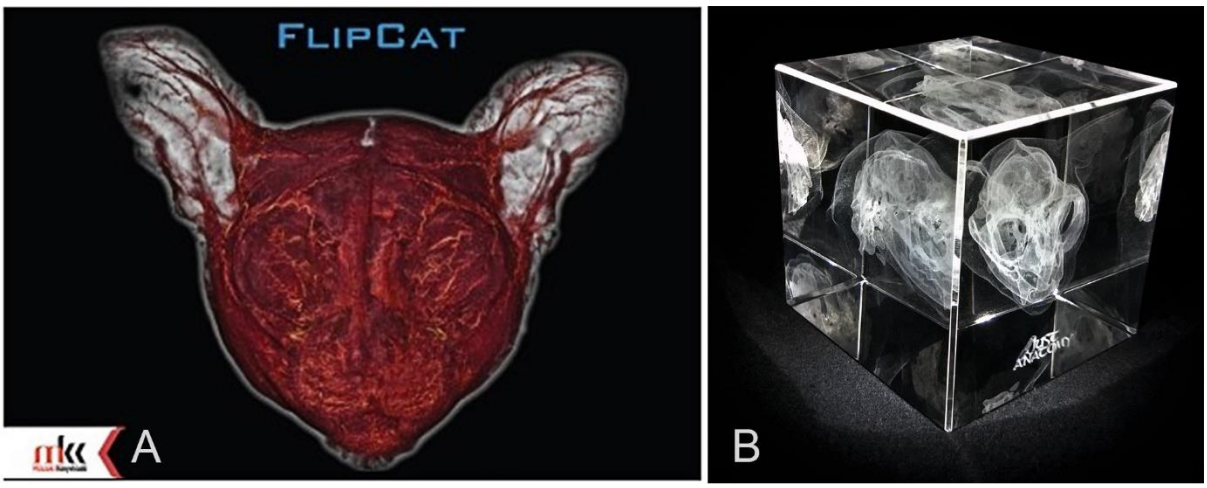

Figure 67. The flip-book of a cat (A), and the same cat's skull engraved into glass (B).

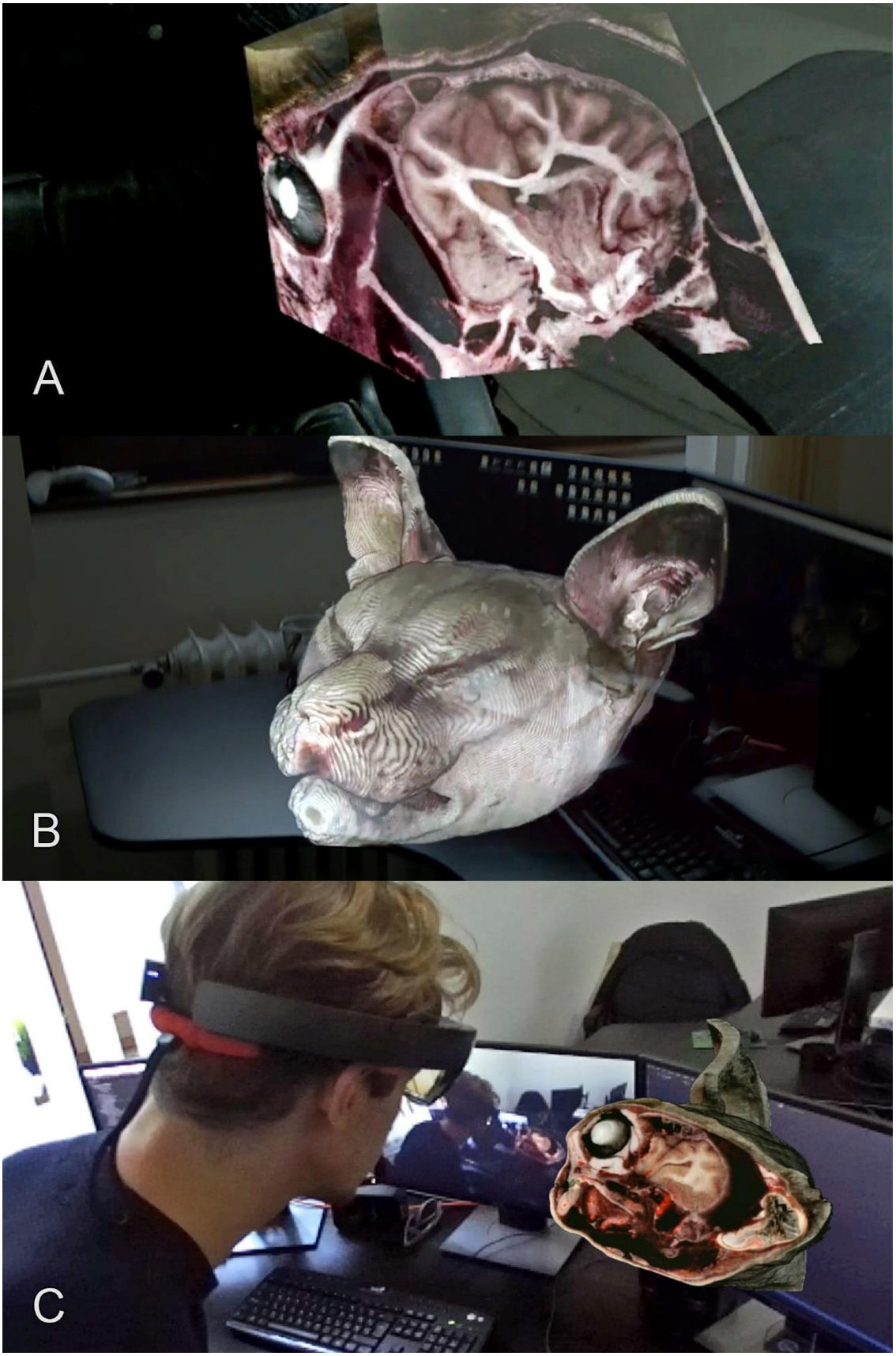

Figure 68. Visualisation with Hololens. A) Looking at the cryosectioned beagle brain. B) The cat head from Study III. C) Showing how the mixed reality looks like from an outer point of view. Sample video on YouTube: https://youtu.be/6pUM07KcqGc

6.2.2. Normalisation and fMRI analysis

I joined to the Department of Ethology and to their FDP in 2016 as a research member of the Senior Family Dog Project (SFDP, funded by the European Research Council grant No. 680040, and under the supervision of dr. Enikő Kubinyi), which aimed to investigate the canine cognitive ageing and CCD. I was also asked to assist the group who conducted awake fMRI studies on dogs. As a part of this work, that brain label map was created which was described earlier among the visualisation studies (chapter 4.3.4). In addition, I developed an image post-processing protocol with the use of various software (Amira, MRIcron, MATLAB, SPM12, 3D Slicer) to ensure that the structural and functional MRI scans of different dog breeds (e.g., golden retriever, border collie, German shepherd) could be successfully normalised to the template image, thereby enabling group-level comparisons. The normalisation procedure and our label map was already used in different canine fMRI studies (Bálint et al., 2020; Boros et al., 2020; Szabó et al., 2020, 2019). Moreover, we also identified the principal components of the canine resting-state network system, which comprises spatially distributed but functionally connected brain regions, such as the sensorimotor, frontal, striatal, auditory and cerebellar networks (**Figure 69**). This awake dog study was the first in its kind in the international scientific research field (Szabó et al., 2019). Furthermore, recently another research group also used our label map after normalizing it to their data, to indicate the different canine encephalic regions in their new beagle MRI template with our annotations (Liu et al., 2020).

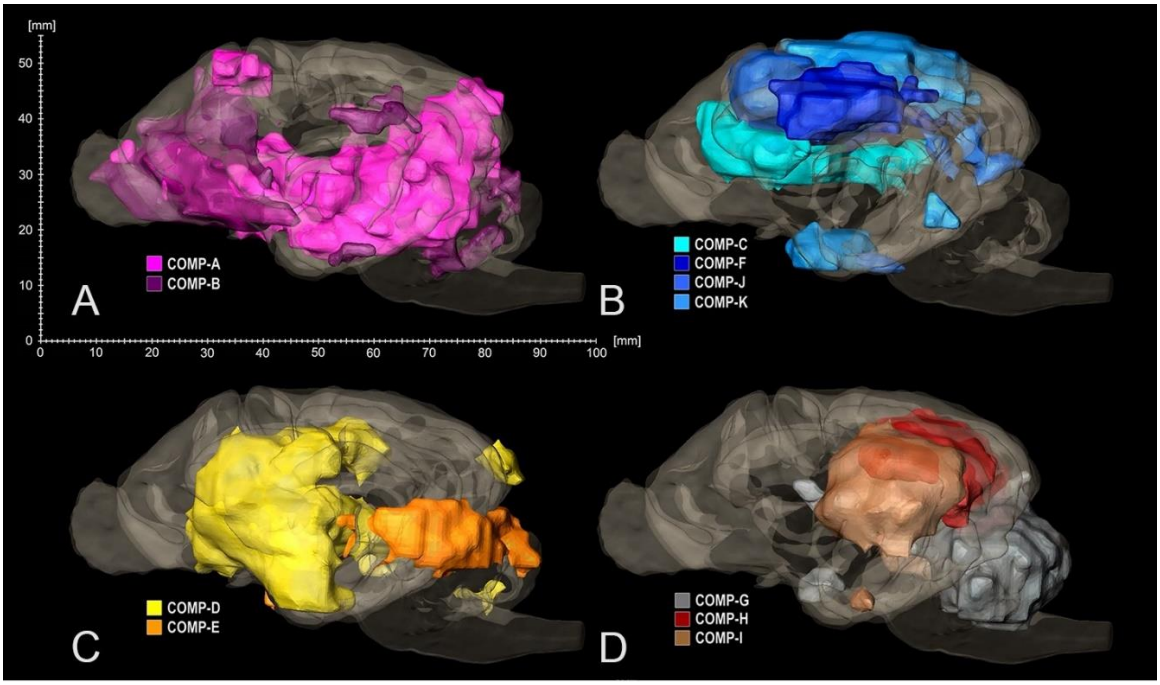

Figure 69. 3D reconstructions of the canine resting state network (for its components, see Szabó et al., 2019.) A) Default mode network. B) Frontal–sensorimotor network. C) Saliency network. D) Auditory–cerebellar network. YouTube-animation: https://youtu.be/0Q1sJgy3b5I

6.2.3. Canine brain banking

Another initiative of the SFDP was to establish a donation system where pet owners can offer their dog's body after euthanasia to the research group for scientific purposes, in line with Hungarian laws. Creating the Canine Brain and Tissue Bank (CBTB) in 2017 made it possible for us to obtain brains and other tissue samples (e.g., skin, muscle, liquor cerebrospinalis, peripheral ganglia) from dog cadavers with a short postmortem time (within 4 hours). Data acquisition, dissection and sample storage is carried out according to strict rules (**Figure 70**). Owners and veterinarians are notified about the donation possibility, and at the time of medically reasoned euthanasia, a donation consent document have to be submitted by both the owner and the veterinarian, which approves and authorizes the subsequent sampling and research processes of the brain banking group. Cadavers are transported to the CBTB unit, where I perform the dissections and sample collections, while other members are immediately processing the obtained tissues. By the end of 2019, we processed more than 130 donations. Due to the efficiency of the short postmortem processing time, the sampling protocol was proven to be successful for preserving ribonucleic acid (RNA); the samples are also stored in formalin solution (at 4°C) and in a deep freezer (at -80°C) (Czakó, 2018). This tissue collection of the CBTB has enabled not only the SFDP group to perform studies related to the canine cognitive ageing, but we made it accessible to other research groups. To date, brain samples were given to researchers working in the United States, Sweden and in the Czech Republic.

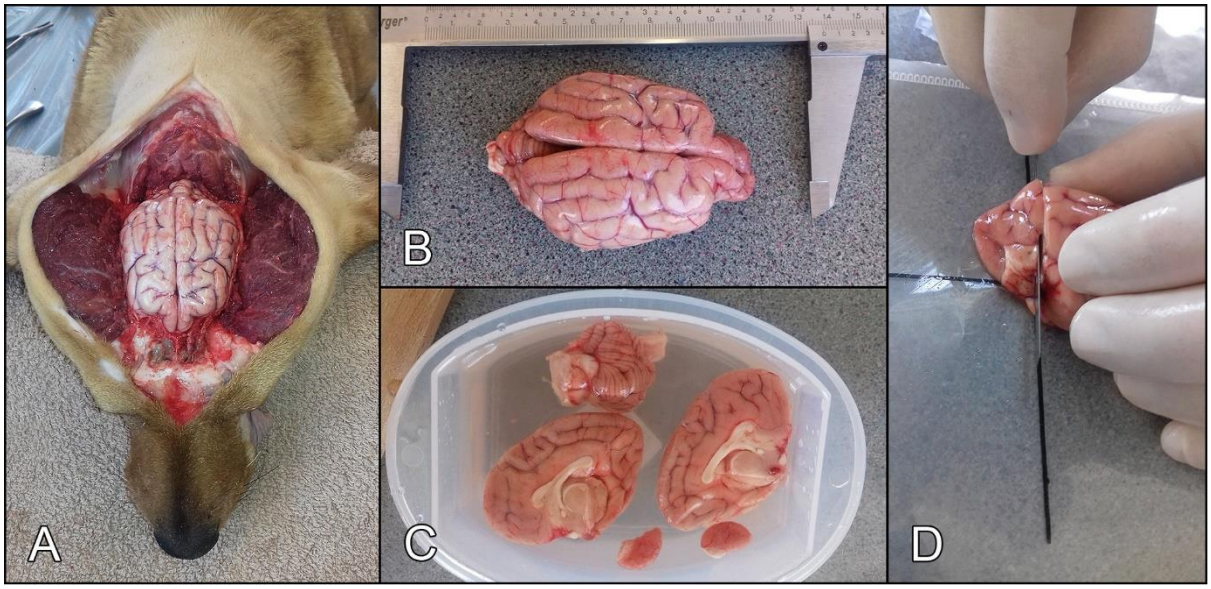

Figure 70. Sample collecting at the CBTB. A) Exposing the brain of a dog after reflecting the skin, the temporal and occipital musculature, followed by the careful removal of the calvaria. B) Measuring the main longitudinal parameters (length, width, height) of the brain. C) Separating the brain into larger blocks and rinsing. D) Making tissue slices.

6.2.4. Neurosurgical interventions

As an outcome of the interest in neuroanatomy and clinical neurology, we started to perform veterinary brain surgeries in Hungary in 2018 together with a veterinarian colleague (dr. László Lehner) at the Felicavet veterinary clinic and hospital (Budapest), regularly consulting with a human neurosurgeon (dr. Gábor Nagy). Together we performed more than thirty neurosurgical interventions in the past two years (until March 2020) in dogs and cats with various diseases. These included 15 intracranial (extra- and intraaxial) tumour removals, 3 transsphenoidal hypophysectomies, 7 ventriculoperitoneal shuntings, 2 cystoperitoneal shuntings, 6 surgical decompressions, and a cystoventricular fenestration. The knowledge I gained throughout the beagle project with the different graphics software was regularly used in data visualisation, pre-surgical 3D planning, or in a special case where a custom-made metal implant had to be created to a Chihuahua to cover the hiatus on his skull after removing an extensive tumour. We carried out the first reported canine ventriculoscopy through the lateral ventricle in order to fenestrate a large parieto-occipital cyst (Lehner et al., 2019d). The 3D models in that case helped us to define the proper position and angle of approach (**Figure 71**) and to give basic orientation guidance when the endoscope was inside the lateral ventricle (**Figures 72** and **73**).

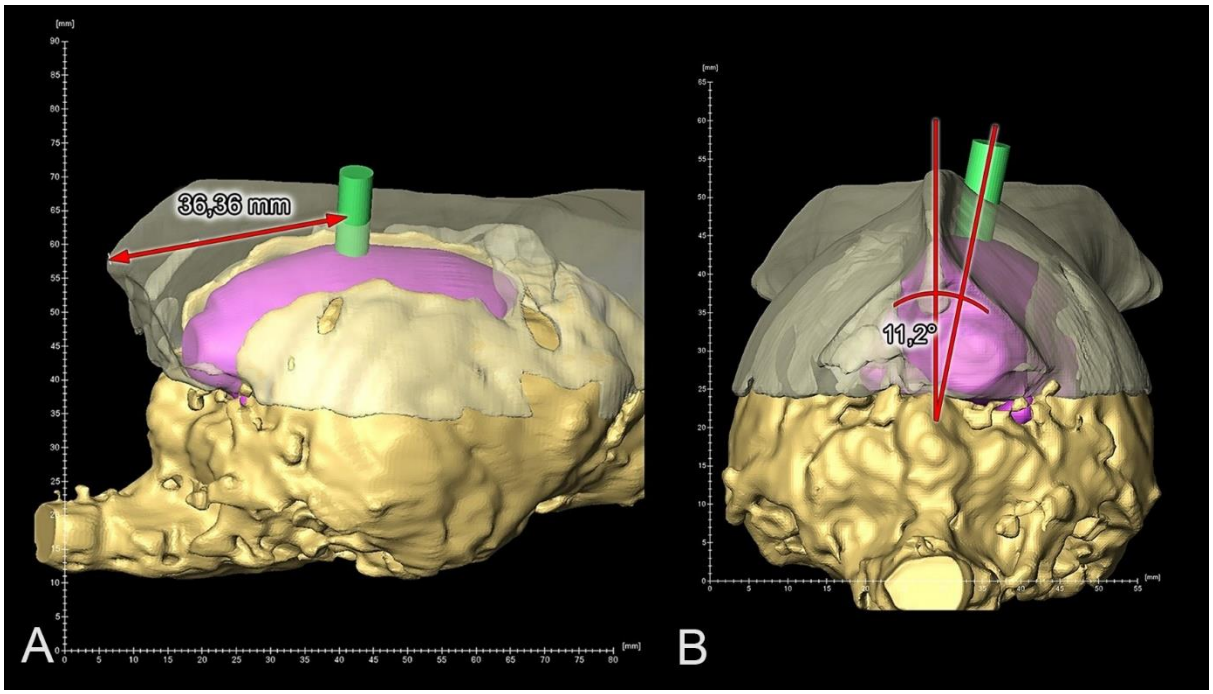

Figure 71. Preoperative 3D planning of a ventriculoscopy in a dog (case study described in Lehner et al., 2019d). Images showing the model of the brain (yellow), the cyst (purple) and the intended route of endoscopic approach (green). A) Right lateral view, distance is shown between the inion (protuberantia occipitalis externa) and the site of the planned surgical approach. B) Caudal view, the initial insertion angle of the endoscope is shown.

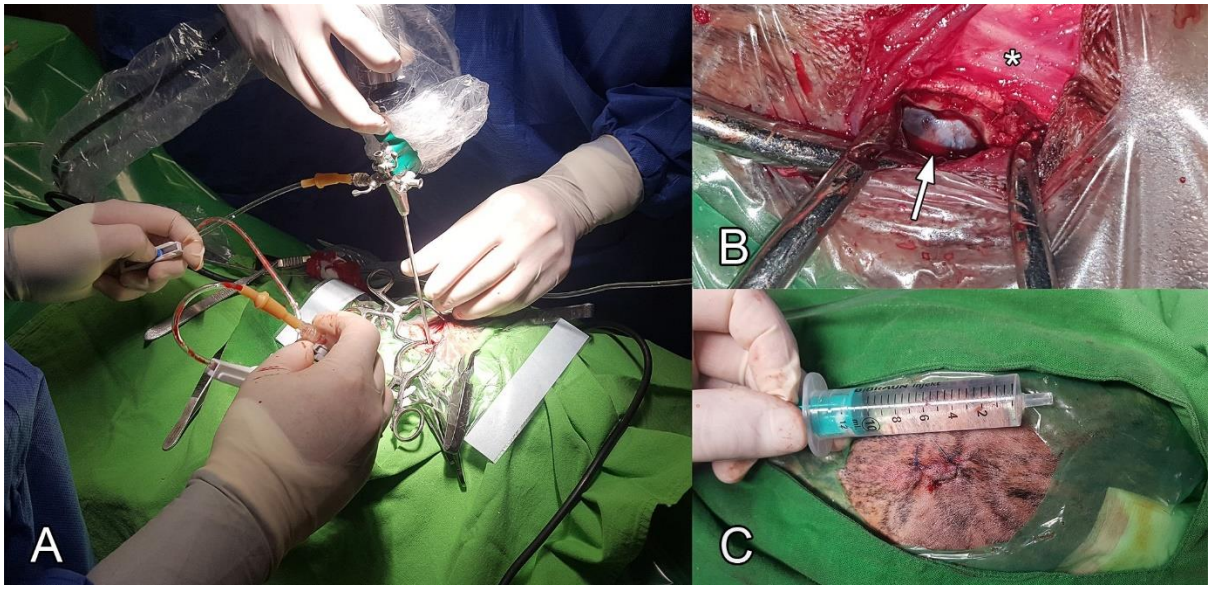

Figure 72. During the ventriculoscopy in a dog. A) Advancing the endoscope into the lateral ventricle. B) The site of the surgical approach, planned based on measurements shown in **Figure 71**. The arrow points to the hole drilled into the calvaria in which the dura mater is visible, and the asterisk (*) marks the adjacent external sagittal crest. C) After closing the wound, demonstrating the size of the minimally invasive surgical approach with a syringe.

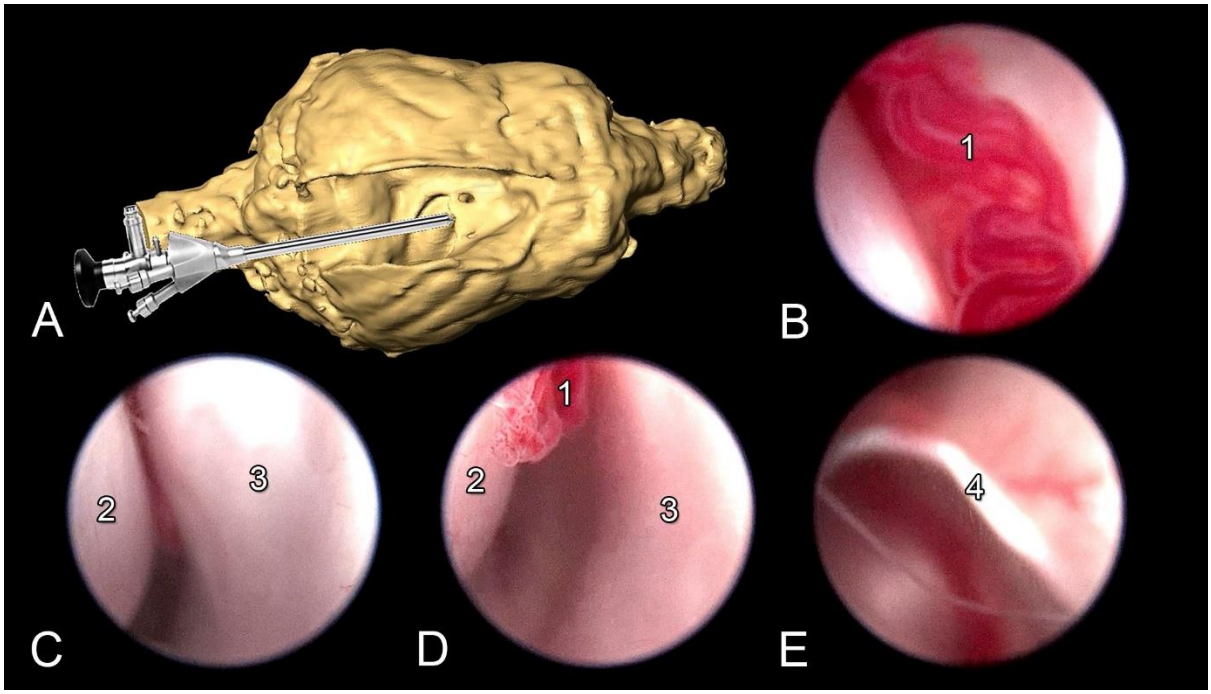

Figure 73. Ventriculoscopy in a dog. A short video about the procedure can also be seen on YouTube: https://youtu.be/K8Km3HMutjY. A) 3D model of the brain with an endoscope aiming at the lateral ventricle, dorsal view. B) Endoscopic view at the level of the thalamus. C, D) Approaching the temporal horn. E) Border of the fenestration. 1) Plexus chorioideus. 2) Hippocampus. 3) Wall of the ventricle. 4) Septum between the cyst and the ventricle.

Furthermore, we used the cryosectioned beagle dataset and its 3D models in the pre-surgical planning phase, when we approached a dog's hypophyseal tumour through the oral cavity (transpharyngeally–transsphenoidally). In this case, we had to exactly define that 5 mm wide spot on the base of the skull where we had to drill through to reach the pituitary gland, while avoiding the injury of to the surrounding major intracranial vessels and nerves (**Figure 74**). We also published multiple case reports (Lehner et al., 2019b, 2019d, 2019a, 2019c, 2018).

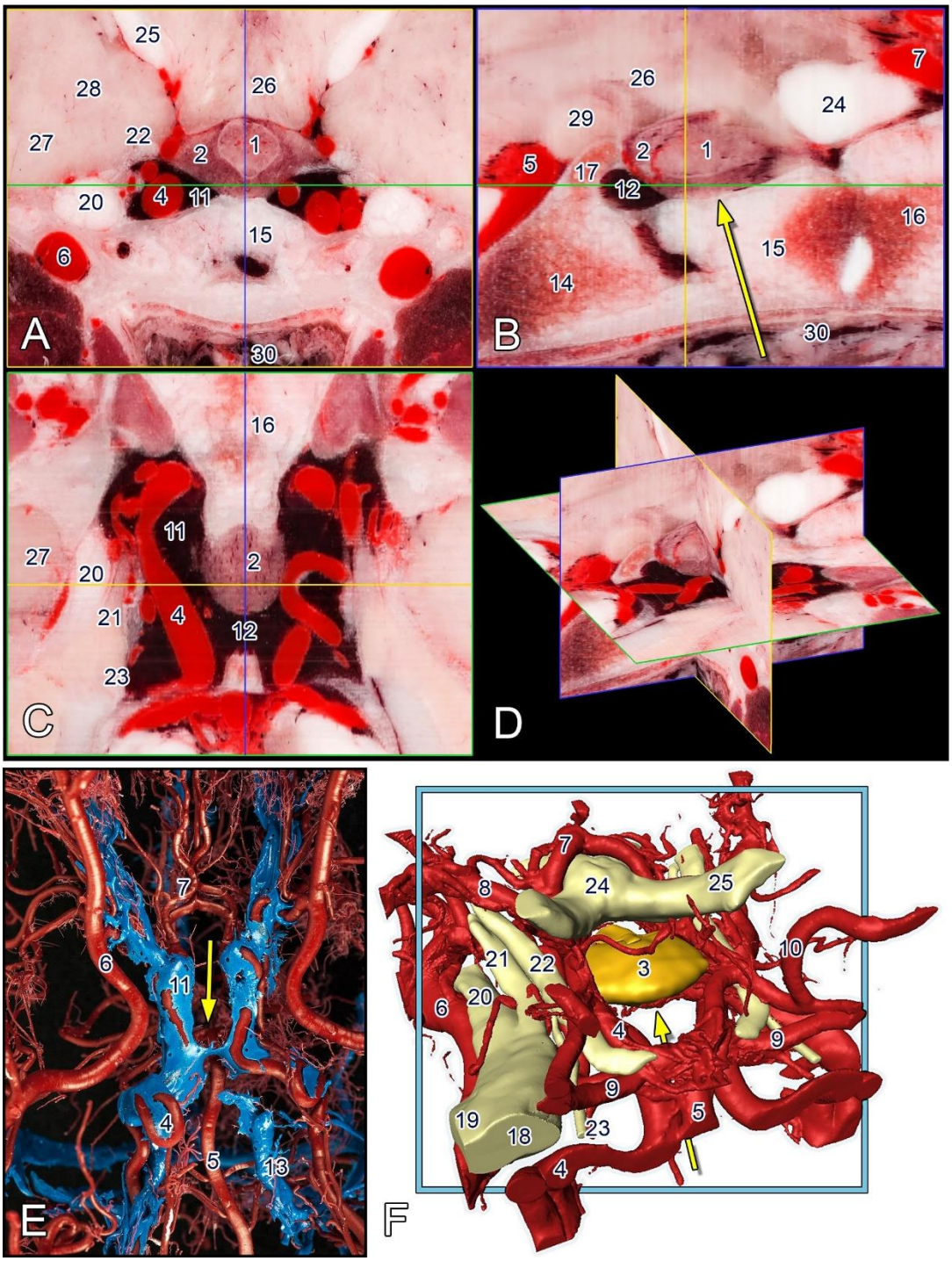

Figure 74. Illustrating the anatomical considerations of a transsphenoidal approach to access the pituitary gland of a dog. For the figure legend, see the next page.

Figure 74. ***(continued)*** Illustrating the anatomical considerations of a transsphenoidal approach to access the pituitary gland of a dog. A, B, C, D) Orthogonal views from the beagle brain dataset showing the main anatomical structures around the pituitary gland. A) Transverse view. B) Sagittal view. C) Dorsal view. D) Multiplanar 3D view. E) Corrosion cast with the main arteries (in red) and veins (in blue) around the hypophyseal region, ventral view. F) 3D model of the structures around the middle cranial fossa; created from the beagle dataset, left caudo-lateral view. G) T2-weighted MR image of the hypophyseal tumour (encircled in red), transverse view. H) Endoscopic view during the surgery, ventral aspect. I, J) The dog presented in Lehner et al. 2019c, 1 month before (I) and 3 months after (J) the removal of her pituitary microadenoma. The yellow arrows (in images B, E, F) show the direction of the transpharyngeal–transsphenoidal surgical approach.

1) Neurohypophysis. 2) Adenohypophysis. 3) Hypophysis. 4) A. carotis interna. 5) A. basilaris. 6) A. maxillaris. 7) A. cerebri rostralis. 8) A. cerebri media. 9) A. cerebelli rostralis. 10) A. cerebri caudalis. 11) Sinus cavernosus. 12) Sinus intercavernosus. 13) Sinus petrosus ventralis. 14) Corpus ossis basioccipitalis. 15) Corpus ossis basisphenoidalis. 16) Corpus ossis presphenoidalis. 17) Dorsum sellae. 18) N. trigeminus. 19) N. mandibularis. 20) N. maxillaris. 21) N. ophthalmicus. 22) N. oculomotorius. 23) N. abducens. 24) Chiasma opticum. 25) Tractus opticus. 26) Hypothalamus. 27) Lobus piriformis. 28) Amygdala. 29) Corpus mamillare. 30) Nasopharynx.

6.3. Conclusion

The improved method utilised for cryosectioning in our final study was proven successful to serve as a good base for providing a comparative, multimodal image series of a canine brain. The cryomacrotomisation procedure is not equivalent to a histological study, but it represents a macro-anatomical cross-sectional approach. The desired resolution in future studies depends on the aim of the study; we believe that the resolution used here is sufficient for a reliable comparison to the CT and MRI series and for the segmentation of major anatomical structures. When investigating smaller structures and thinner layers (below 20–30 μm), we recommend the standard histological procedures.

The main achievement of the project is that this was the first study in dogs that has visualised the brain using comparative imaging modalities resulting in excellent quality and detail, with high-resolution images of 100 μm layer thickness. Possibilities also include the application of 3D modelling and 3D printing technologies to enhance learning in graduate and postgraduate studies. In the results section, we presented the main advantages of our improved cryosectioning technique and gave several examples through multiplanar reconstructions of how this method can aid comparative imaging by merging the diagnostic imaging modalities (CT, MR) with cryosectioned images and 3D models. We also plan to use a cryoprotective agent (e.g., sucrose, glycerol, dimethyl-sulfoxide) prior to freezing the block in future works. Due to the detail of the images, the image sets are suitable for selective structure segmentation and extraction, as was shown for the skull, brain, arteries and veins. Thus, the resulting models can be exported, enlarged and studied in any perspective, providing an excellent support to accompany textbooks on this subject. We are considering the investigation of inter-subject variability to broaden the findings presented herein, as it would be worthwhile to obtain cryosectioned image series from dog breeds with dolichocephalic, mesaticephalic and brachycephalic skull conformations.

To conclude, the cryomacrotomisation technique is a unique complementary tool for studying cross-sectional anatomy and to create volumetric data. We have already seen advantageous outcomes which resulted from the neuroanatomical studies and the 3D visualisation in various academic and clinical fields. Therefore, results of these works are awaited and are anticipated to future scientific discovery.

7. New scientific results

Ad 1. Providing high-resolution, multimodal, macro-anatomical images from a canine brain.

The image set we recorded from the final study has the highest level of detail among the macro-anatomical canine brain studies conducted to date. The high-resolution digital photography and the small milling interval enabled us to create different multiplanar reconstructions, annotated illustrations and 3D models, which could be directly compared with the CT and MR imaging datasets of the same animal.

Ad 2. Developing a custom-made cryosectioning workflow.

The cryomacrotomisation procedure up to this point had only been used in a couple of research facilities across the world, and it requires dedicated teams and specially designed cryosectioning devices. We developed our own method by testing various milling systems and freezing settings. An optimal setup proved to be feasible for carrying out high-quality studies with a small team and an engineering CNC machine.

Ad 3. Creating a canine brain MRI label map for research.

To provide an aid in the fMRI analysis and to complete the cryosectioning study with a digital neuroanatomical guide, an individual dog brain template was chosen and an MRI label map was created which comprises the main canine encephalic structures.

Ad 4. Composing accessible 3D models from complex structures.

During the visualisation studies different 3D models and publicly available videos and images were created, like an osseo-vascular model of a French bulldog head and neck demonstrating the blood supply; a transparent equine petrosal showing the hidden intraosseous structures; and the arteries with different details of a cat head.

Ad 5. Associated advances in canine neuroscience and small animal neurosurgery.

The achievements on these fields are connected to our main project as the results of its direct scientific and clinical utilisation; with the fMRI analysis we identified the functional resting-state network system of awake dogs; and the neuroanatomical knowledge and 3D surgical planning allowed us to perform brain surgeries in dogs on a regular basis, thereby enabling a new clinical field in veterinary medicine in Hungary.

8. References

Adams, B., Chan, A., Callahan, H., Milgram, N.W.: **The canine as a model of human cognitive aging: Recent developments**, Prog. Neuro-Psychoph. 24. 675–92, 2000.

Adhi, M., Duker, J.S.: **Optical coherence tomography – current and future applications**, Curr. Opin. Ophthalmol., 24. 213–21, 2013.

Adluru, N., Zhang, H., Fox, A.S., Shelton, S.E., Ennis, C.M., Bartosic, A.M., Oler, J.A., Tromp, D.P.M., Zakszewski, E., Gee, J.C., Kalin, N.H., Alexander, A.L.: **A diffusion tensor brain template for Rhesus Macaques**, NeuroImage, 59. 306–18, 2012.

Adrianov, O.S., Mering, T.A.: **Atlas of the canine brain**, 1st ed., Arlington, Massachusetts: NPP Books, 2010.

Akkus, Z., Galimzianova, A., Hoogi, A., Rubin, D.L., Erickson, B.J.: **Deep learning for brain MRI segmentation: state of the art and future directions**, J. Digit. Imaging, 30. 449–59, 2017.

Amunts, K., Lepage, C., Borgeat, L., Mohlberg, H., Dickscheid, T., Rousseau, M.-É., Bludau, S., Bazin, P.-L., Lewis, L.B., Oros-Peusquens, A.-M., Shah, N.J., Lippert, T., Zilles, K., Evans, A.C.: **BigBrain: an ultrahigh-resolution 3D human brain model**, Science, 340. 1472–5, 2013.

Andics, A., Gábor, A., Gácsi, M., Faragó, T., Szabó, D., Miklósi, Á.: **Neural mechanisms for lexical processing in dogs**, Science, 353. 1030–2, 2016.

Andics, A., Gácsi, M., Faragó, T., Kis, A., Miklósi, A.: **Voice-sensitive regions in the dog and human brain are revealed by comparative fMRI**, Curr. Biol. 24. 574–8, 2014.

Andics, A., Miklósi, Á.: **Neural processes of vocal social perception: Dog-human comparative fMRI studies**, Neurosci. Biobehav. Rev., 85. 54–64, 2018.

Annese, J., Sforza, D.M., Dubach, M., Bowden, D., Toga, A.W.: **Postmortem high-resolution 3-dimensional imaging of the primate brain: blockface imaging of perfusion stained tissue**, Neuroimage, 30. 61–9, 2006.

Assheuer, J., Sager, M.: **MRI and CT atlas of the dog**, 1st ed., Berlin: Wiley, 1997.

Augulis, V., Sigg, E.B.: **Supravital staining and fixation of brain and spinal cord by intravascular perfusion**, Stain Technol., 46. 183–90, 1971.

Bajzik, G., Czeibert, K., Donkó, T., Garbera, I., Nemes, C., Petneházy, Ö., Repa, I., Sütő, Z., Szabó, G., Takács, I., Vajda, Z., Zádori, P.: **Cross-sectional, CT and MR anatomy atlas of the domestic turkey**, 1st ed., Kaposvár: University of Kaposvár, 2015.

Bálint, A., Andics, A., Gácsi, M., Gábor, A., Czeibert, K., Luce, C.M., Miklósi, Á., Kröger, R.H.H.: **Dogs can sense weak thermal radiation**, Sci. Rep., 10. 1–9, 2020.

Bergström, K., Nyberg, G., Pech, P., Rauschning, W., Ytterbergh, C.: **Multiplanar spinal anatomy: comparison of CT and cryomicrotomy in postmortem specimens**, Am. J. Neuroradiol., 4. 590–2, 1983.

Berns, G.S., Brooks, A.M., Spivak, M.: **Functional MRI in awake unrestrained dogs**, PLOS ONE, 7. e38027, 2012.

Boros, M., Gábor, A., Szabó, D., Bozsik, A., Gácsi, M., Szalay, F., Faragó, T., Andics, A.: **Repetition enhancement to voice identities in the dog brain**, Sci. Rep. 10. 1–9, 2020.

Böttcher, P., Maierl, J.: **Macroscopic cryosectioning: a simple new method for producing digital, three-dimensional databases in veterinary anatomy**, Anat. Histol. Embryol., 28. 97–102, 1999.

Böttcher, P., Maierl, J., Schiemann, T., Glaser, C., Weller, R., Hoehne, K.-H., Reiser, M., Liebich, H.-G.: **The Visible Animal Project: a three-dimensional, digital database for high quality three-dimensional reconstructions**, Vet. Radiol. Ultrasoun., 40. 611–6, 1999.

Brenner, E.: **Human body preservation – old and new techniques**, J. Anat., 224. 316–44, 2014.

Bunford, N., Andics, A., Kis, A., Miklósi, Á., Gácsi, M.: ***Canis familiaris* as a model for non-invasive comparative neuroscience**, Trends Neurosci., 40. 438–52, 2017.

Carreira, L.M., Ferreira, A.: **Anatomical variations in the pseudosylvian fissure morphology of brachy-, dolicho-, and mesaticephalic dogs**, Anat. Rec., 298. 1255–60, 2015a.

Carreira, L.M., Ferreira, A.: **Longitudinal cerebral fissure anatomy variations in brachy-, dolicho- and mesaticephalic dogs and their importance to brain surgery**, Anat. Rec., 298. 1612–21, 2015b.

Christ, R., Guevar, J., Poyade, M., Rea, P.M.: **Proof of concept of a workflow methodology for the creation of basic canine head anatomy veterinary education tool using augmented reality**, PLOS ONE, 13. e0195866, 2018.

Chung, B.S., Chung, M.S., Lee, S.-B., Youn, C., Park, J.S.: **Sectioned images of a cat head to contribute to learning of its sectional anatomy**, Int. J. Morphol., 36. 537–43, 2018.

Chung, B.S., Jeon, C.-Y., Huh, J.-W., Jeong, K.-J., Har, D., Kwack, K.-S., Park, J.S.: **Rise of the Visible Monkey: sectioned images of Rhesus monkey**, J. Korean Med. Sci., 34. 2019.

Cintra, T.C.F., Carvalho, C.F., Canola, J.C., Nepomuceno, A.C.: **Transcranial ultrasonography in healthy dogs: technique standardization and anatomic description**, Arq. Bras. Med. Vet. Zootec., 66. 61–8, 2014.

Constantinescu, G., Schaller, O.: **Illustrated veterinary anatomical nomenclature**, 3rd ed., Stuttgart: Thieme, 2011.

Cook, P.F., Brooks, A., Spivak, M., Berns, G.S.: **Regional brain activity in awake unrestrained dogs**, J. Vet. Behav., 10. 440, 2015.

Cotman, C.W., Head, E.: **The canine (dog) model of human aging and disease: dietary, environmental and immunotherapy approaches**, J. Alzheimers Dis., 15. 685–707, 2008.

Couturier, L., Degueurce, C., Ruel, Y., Dennis, R., Begon, D.: **Anatomical study of cranial nerve emergence and skull foramina in the dog using magnetic resonance imaging and computed tomography**, Vet. Radiol. Ultrasoun., 46. 375–83, 2005.

Cox, D.D., Savoy, R.L.: **Functional magnetic resonance imaging (fMRI) "brain reading": detecting and classifying distributed patterns of fMRI activity in human visual cortex**, NeuroImage, 19. 261–70, 2003.

Cuaya, L.V., Hernández-Pérez, R., Concha, L.: **Our faces in the dog's brain: functional imaging reveals temporal cortex activation during perception of human faces**, PLOS ONE, 11. e0149431, 2016.

Czakó, L.: **A new Hungarian initiative: creating the Canine Brain and Tissue Bank**, Students' Research Circle thesis, Eötvös Loránd University and the University of Veterinary Medicine, Budapest, 2018. (in Hungarian with English abstract)

Czeibert, K., Andics, A., Petneházy, Ö., Kubinyi, E.: **A detailed canine brain label map for neuroimaging analysis**, Biol. Fut., 70. 112–20, 2019a.

Czeibert, K., Baksa, G., Grimm, A., Nagy, S.A., Horák, D., Petneházy, Ö.: **FlipCat: Cat's head seen on MRI and cryosections**, 1st ed., Budapest: Műszaki Könyvkiadó Kft., 2015.

Czeibert, K., Baksa, G., Grimm, A., Nagy, S.A., Kubinyi, E., Petneházy, Ö.: **MRI, CT and high resolution macro-anatomical images with cryosectioning of a Beagle brain: Creating the base of a multimodal imaging atlas**, PLOS ONE, 14. e0213458, 2019b.

Czeibert, K., Baksa, G., Kozma, I., Pomsár, M., Rácz, B., Petneházy, Ö.: **Comparative 3-dimensional visualization of the equine petrosal bone**, Magy. Állatorvosok, 140. 737–44, 2018. (in Hungarian with English abstract)

Damestani, Y., Reynolds, C.L., Szu, J., Hsu, M.S., Kodera, Y., Binder, D.K., Park, B.H., Garay, J.E., Rao, M.P., Aguilar, G.: **Transparent nanocrystalline yttria-stabilized-zirconia calvarium prosthesis**, Nanomed-Nanotechnol., 9. 1135–8, 2013.

Datta, R., Lee, J., Duda, J., Avants, B.B., Vite, C.H., Tseng, B., Gee, J.C., Aguirre, G.D., Aguirre, G.K.: **A digital atlas of the dog brain**, PLOS ONE, 7. e52140, 2012.

De Rycke, L.M., Gielen, I.M., Van Meervenne, S.A., Simoens, P.J., van Bree, H.J.: **Computed tomography and cross-sectional anatomy of the brain in clinically normal dogs**, Am. J. Vet. Res., 66. 1743–56, 2005.

Dennis, R.: **Magnetic resonance imaging and its applications in small animals**, In Practice, 20. 117–24, 1998.

Dettmeyer, R.B.: **Forensic histopathology**, 1st ed., Berlin, Heidelberg: Springer Berlin Heidelberg, 2011.

Ding, S.-L., Royall, J.J., Sunkin, S.M., Ng, L., Facer, B.A.C., Lesnar, P. et al.: **Comprehensive cellular-resolution atlas of the adult human brain**, J. Comp. Neurol., 524. 3127–481, 2016.

Dogdas, B., Stout, D., Chatziioannou, A.F., Leahy, R.M.: **Digimouse: a 3D whole body mouse atlas from CT and cryosection data**, Phys. Med. Biol., 52. 577–87, 2007.

Done, S.H., Goody, P.C., Evans, S.A., Stickland, N.C.: **Color atlas of veterinary anatomy, volume 3. The dog and cat**, 2nd ed., Edinburgh, New York: Mosby, 2009.

Dua-Sharma, S., Shama, K.N., Jacobs, H.L.: **The canine brain in stereotaxic coordinates**, 1st ed., Cambridge, Massachusetts: The MIT Press, 1971.

Ella, A., Keller, M.: **Construction of an MRI 3D high resolution sheep brain template**, Magn. Reson. Imaging, 33. 1329–37, 2015.

Elliott, I., Skerritt, G.: **Handbook of small animal MRI**, 1st ed., Chichester, West Sussex: Wiley-Blackwell, 2010.

Elnady, F.A.: **The Elnady technique: An innovative, new method for tissue preservation**, ALTEX, 33. 237–42, 2016.

Erdogmus, D., G. Larsson, E., Yan, R., C. Principe, J., R. Fitzsimmons, J.: **Measuring the signal-to-noise ratio in magnetic resonance imaging: a caveat**, Signal Process., 84. 1035–40, 2004.

Evans, H.E., de Lahunta, A.: **Miller's anatomy of the dog**, 4th ed., St. Louis, Missouri: Saunders, 2012.

Fenyves, I., Szentpétery, Z.: **Questions and answers in small animal ophthalmology**, 1st ed., Budapest: MÁOK Kft., 2018.

Fike, J.R., LeCouteur, R.A., Cann, C.E.: **Anatomy of the canine brain using high resolution computed tomography**, Vet. Radiology, 22. 236–43, 1981.

Fletcher, T.F., Saveraid, T.C.: **An online canine MRI brain atlas**, http://Vanat.Cvm.Umn.Edu/MriBrainAtlas: University of Minnesota College of Veterinary Medicine, 2009.

Frohlich, I., Probst, A., Polgar, M., Sora, M.C., Konig, H.E.: **Plastic-embedded brain slices of the dog - a basis for clinical examination with modern diagnostic imaging**, Wien. Tierarz. Monats., 90. 62–6, 2003.

Gasteiger, E.L., Lewkowicz, J., Molitzau, D.L.: **Cinematography of brain structures prepared by perfusion staining**, Stain Technol., 44. 111–5, 1969.

Gavin, P.R.: **Growth of clinical veterinary magnetic resonance imaging**, Vet. Radiol. Ultrasoun., 52. S2-4, 2011.

Gavin, P.R., Bagley, R.S., editors.: **Practical small animal MRI**, 1st ed., Ames, Iowa: Wiley-Blackwell, 2009.

George, T.F., Smallwood, J.E.: **Anatomic atlas for computed tomography in the mesaticephalic dog: head and neck**, Vet. Radiol. Ultrasoun., 33. 217–40, 1992.

Goerner, F.L., Clarke, G.D.: **Measuring signal-to-noise ratio in partially parallel imaging MRI**, Med. Phys., 38. 5049–57, 2011.

Gomercic, H., Kramer, M., Mihaljevic, M., Duras-Gomercic, M., Gomercic, T., Hartmann, A., Jawinski, S., Klumpp, S., Sonntag, F.: **CT-und MRT-Atlas: Transversalanatomie des Hundes**, 1st ed., Stuttgart: Enke, 2009.

Griffin, G., Clark, J.M., Zurlo, J., Ritskes-Hoitinga, M.: **Scientific uses of animals: harm-benefit analysis and complementary approaches to implementing the three Rs**, Rev. - Off. Int. Epizoot., 33. 265–72, 2014.

Hage, M.C.F.N.S., Iwasaki, M., Rabbani, S.R., Kamikawa, L., Cervantes, H.J.R., Bombonato, P.P., Sterman, F.A., Otaduy, M.C.G.: **Magnetic resonance imaging in the investigation of canine heads**, Pesqui. Vet. Brasil., 30. 593–604, 2010.

von Hagens, G., Tiedemann, K., Kriz, W.: **The current potential of plastination**, Anat. Embryol., 175. 411–21, 1987.

Hartmann, A., Söffler, C., Failing, K., Schaubmar, A., Kramer, M., Schmidt, M.J.: **Diffusion-weighted magnetic resonance imaging of the normal canine brain**, Vet. Radiol. Ultrasoun., 55. 592–8, 2014.

Head, E.: **A canine model of human aging and Alzheimer's disease**, Biochim. Biophys. Acta, 1832. 1384–9, 2013.

Hecht, E.E., Smaers, J.B., Dunn, W.D., Kent, M., Preuss et al.: **Significant neuroanatomical variation among domestic dog breeds**, J. Neurosci., 39. 7748–58, 2019.

Hikishima, K., Quallo, M.M., Komaki, Y., Yamada, M., Kawai, K., Momoshima, S., Okano, H.J., Sasaki, E., Tamaoki, N., Lemon, R.N., Iriki, A., Okano, H.: **Population-averaged standard template brain atlas for the common marmoset (*Callithrix jacchus*)**, NeuroImage, 54. 2741–9, 2011.

Hirschberg, R.M., Mülling, C.K., Bragulla, H.: **Microvasculature of the bovine claw demonstrated by improved micro-corrosion-casting technique**, Microsc. Res. Tech., 45. 184–97, 1999.

Hudson, J.A., Cartee, R.E., Simpson, S.T., Buxton, D.F.: **Ultrasonographic anatomy of the canine brain**, Vet. Radiology, 30. 13–21, 1989.

Hussein, A.K., Sullivan, M., Penderis, J.: **Effect of brachycephalic, mesaticephalic, and dolichocephalic head conformations on olfactory bulb angle and orientation in dogs as determined by use of in vivo magnetic resonance imaging**, Am. J. Vet. Res., 73. 946–51, 2012.

Jaggy, A., Couteur, R. le.: **Atlas and textbook of small animal neurology: an illustrated text**, 1st ed., Hannover: Schluetersche, 2010.

Kaivosoja, T.P., Liu, S., Dijkstra, J., Huhtala, H., Sheth, T., Kajander, O.A.: **Comparison of visual assessment and computer image analysis of intracoronary thrombus type by optical coherence tomography**, PLOS ONE, 13. e0209110, 2018.

Kang, B.-T., Ko, K.-J., Jang, D.-P., Han, J.-Y., Lim, C.-Y., Park, C., Yoo, J.-H., Kim, J.-W., Jung, D.-I., Kim, Y.-B., Woo, E.-J., Cho, Z.-H., Park, H.-M.: **Magnetic resonance imaging of the canine brain at 7 T**, Vet. Radiol. Ultrasoun., 50. 615–21, 2009.

Kärkkäinen, M., Mero, M., Nummi, P., Punto, L.: **Low field magnetic resonance imaging of the canine central nervous system**, Vet. Radiology, 32. 71–4, 1991.

Kaufman, H.H., Cohen, G., Glass, T.F., Huchton, J.D., Pruessner, J.L., Ostrow, P.T., Andia-Waltenbaugh, A.-M., Dujovny, M.: **CT atlas of the dog brain**, J. Comput. Assist. Tomo., 5. 529, 1981.

Kawamura, K., Naito, J.: **Variations of the dog cerebral sulci, compared in particular with those of the cat**, J. Hirnforsch., 19. 457–67, 1978.

Khanna, C., Lindblad-Toh, K., Vail, D., London, C., Bergman, P., Barber, L., Breen, M., Kitchell, B., McNeil, E., Modiano, J.F., Niemi, S., Comstock, K.E., Ostrander, E., Westmoreland, S., Withrow, S.: **The dog as a cancer model**, Nat. Biotechnol., 24. 1065–6, 2006.

Kim, Y., Kim, H., Kim, Y.O.: **Virtual reality and augmented reality in plastic surgery: a review**, Arch. Plast. Surg., 44. 179–87, 2017.

King, C., Birch, W.: **Assessment of maceration techniques used to remove soft tissue from bone in cut mark analysis**, J. Forensic Sci., 60. 124–35, 2015.

Kraft, S.L., Gavin, P.R., Wendling, L.R., Reddy, V.K.: **Canine brain anatomy on magnetic resonance images**, Vet. Radiology, 30. 147–58, 1989.

Krucker, T., Lang, A., Meyer, E.P.: **New polyurethane-based material for vascular corrosion casting with improved physical and imaging characteristics**, Microsc. Res. Tech., 69. 138–47, 2006.

Landsberg, G., Maďari, A., Žilka, N., editors.: **Canine and feline dementia: molecular basis, diagnostics and therapy**, 1st ed., Cham: Springer International Publishing, 2017.

Landsberg, G.M., Nichol, J., Araujo, J.A.: **Cognitive dysfunction syndrome: a disease of canine and feline brain aging**, Veterinary Clinics of North America: Small Animal Practice, 42. 749–68, 2012.

Lehner, L., Czeibert, K., Csöndes, J., Balogh, N., Kerekes, Z., Jakab, C.: **Endoscope-guided transsphenoidal removal of a hypophyseal tumour in a dog. Case study**, Magy. Állatorvosok, 140. 535–50, 2018. (in Hungarian with English abstract)

Lehner, L., Czeibert, K., Koltai, Z., Jakab, C.: **Removal of frontal meningioma by bilateral transfrontal approach in dog. Case study**, Magy. Állatorvosok, 141. 533–45, 2019a. (in Hungarian with English abstract)

Lehner, L., Garamvölgyi, R., Jakab, C., Kerekes, Z., Czeibert, K.: **A recurrent suprapituitary ependymal cyst managed by endoscopy-assisted transsphenoidal surgery in a canine: a case report**, Front. Vet. Sci., 6. 2019b.

Lehner, L., Jakab, C., Czeibert, K.: **Surgical management of central Cushing-disease: successful endoscope-assisted removal of a hypophyseal microadenoma in a Boxer. Case study**, Magy. Állatorvosok, 141. 289–300, 2019c. (in Hungarian with English abstract)

Lehner, L., Nagy, G., Jakab, C., Czeibert, K.: **Ventriculoscopy in a dog: fenestration of a parieto-occipital cyst into the lateral ventricle with an endoscope. Case report**, Magy. Állatorvosok, 141. 145–56, 2019d. (in Hungarian with English abstract)

Leigh, E.J., Mackillop, E., Robertson, I.D., Hudson, L.C.: **Clinical anatomy of the canine brain using magnetic resonance imaging**, Vet. Radiol. Ultrasoun., 49. 113–21, 2008.

Lim, R.K.-S., Liu, C.-N., Moffitt, R.L., Windle, W.F.: **A stereotaxic atlas of the dog's brain**, 1st ed., Springfield: Charles C Thomas, 1960.

Liu, X., Tian, R., Zuo, Z., Zhao, H., Wu, L., Zhuo, Y., Zhang, Y.Q., Chen, L.: **A high-resolution MRI brain template for adult Beagle**, Magn. Reson. Imaging, in press, 2020.

Logothetis, N.K., Pfeuffer, J.: **On the nature of the BOLD fMRI contrast mechanism**, Magn. Reson. Imaging, 22. 1517–31, 2004.

Lufkin, R., Rauschning, W., Seeger, L., Bassett, L., Hanafee, W.: **Anatomic correlation of cadaver cryomicrotomy with magnetic resonance imaging**, Surg. Radiol. Anat., 9. 299–302, 1987.

Madari, A., Farbakova, J., Katina, S., Smolek, T., Novak, P., Weissova, T., Novak, M., Zilka, N.: **Assessment of severity and progression of canine cognitive dysfunction syndrome using the CAnine DEmentia Scale (CADES)**, Appl. Anim. Behav. Sci., 171. 138–45, 2015.

Mai, W., editor.: **Diagnostic MRI in dogs and cats**, 1st ed., Boca Raton: CRC Press, 2018.

Martín-Vaquero, P., Da Costa, R.C., Echandi, R.L., Tosti, C.L., Knopp, M.V., Sammet, S.: **Magnetic resonance imaging of the canine brain at 3 and 7 T**, Vet. Radiol. Ultrasoun., 52. 25–32, 2011.

Milne, M.E., Steward, C., Firestone, S.M., Long, S.N., O'Brien, T.J., Moffat, B.A.: **Development of representative magnetic resonance imaging-based atlases of the canine brain and evaluation of three methods for atlas-based segmentation**, Am. J. Vet. Res., 77. 395–403, 2016.

Mogicato, G., Conchou, F., Raharison, F., Sautet, J.: **Normal canine brain: comparison between magnetic resonance imaging and cross-sectional anatomy**, Rev. Med. Vet-Toulouse, 162. 400–405., 2011.

Muñoz-Moreno, E., Arbat-Plana, A., Batalle, D., Soria, G., Illa, M., Prats-Galino, A., Eixarch, E., Gratacos, E.: **A magnetic resonance image based atlas of the rabbit brain for automatic parcellation**, PLOS ONE, 8. e67418, 2013.

Nakade T., Ichikawa T., Uchida Y., Taguchi K., Taniyama H.: **Normal brain CT atlas of the Beagle dog: comparative anatomy of the coronal section**, J. Anim. Clin. Med., 12. 109–16, 2003.

National Research Council.: **Guide for the care and use of laboratory animals**, 8th ed., Washington (DC): National Academies Press (US), 2011.

Nickel, R., Schummer, A., Seiferle, E.: **Lehrbuch der Anatomie der Haustiere, Band IV: Nervensystem, Sinnesorgane, Endokrine Drüsen**, 4th ed., Berlin: Enke, 2003.

Nie, B., Chen, K., Zhao, S., Liu, J., Gu, X., Yao, Q., Hui, J., Zhang, Z., Teng, G., Zhao, C., Shan, B.: **A rat brain MRI template with digital stereotaxic atlas of fine anatomical delineations in Paxinos space and its automated application in voxel-wise analysis**, Hum. Brain. Mapp., 34. 1306–18, 2013.

Nitzsche, B., Boltze, J., Ludewig, E., Flegel, T., Schmidt, M.J., Seeger, J., Barthel, H., Brooks, O.W., Gounis, M.J., Stoffel, M.H., Schulze, S.: **A stereotaxic breed-averaged, symmetric T2w canine brain atlas including detailed morphological and volumetrical data sets**, Neuroimage, 2018.

Nitzsche, B., Frey, S., Collins, L.D., Seeger, J., Lobsien, D., Dreyer, A., Kirsten, H., Stoffel, M.H., Fonov, V.S., Boltze, J.: **A stereotaxic, population-averaged T1w ovine brain atlas including cerebral morphology and tissue volumes**, Front. Neuroanat., 9. 2015.

Offele, D., Harbeck, M., Dobberstein, R.C., von Wurmb-Schwark, N., Ritz-Timme, S.: **Soft tissue removal by maceration and feeding of Dermestes sp.: impact on morphological and biomolecular analyses of dental tissues in forensic medicine**, Int. J. Legal Med., 121. 341–8, 2007.

Palazzi, X.: **The Beagle brain in stereotaxic coordinates**, 1st ed., New York, NY: Springer New York, 2011.

Park, H.S., Shin, D.S., Cho, D.H., Jung, Y.W., Park, J.S.: **Improved sectioned images and surface models of the whole dog body**, Ann. Anat., 196. 352–9, 2014.

Park, J.S.: **Cross-sectional atlas of the human head: with 0.1-mm pixel size color images**, 1st ed., Singapore: Springer, 2017.

Park, J.S., Chung, M.S., Hwang, S.B., Lee, Y.S., Har, D.-H., Park, H.S.: **Visible Korean human: Improved serially sectioned images of the entire body**, IEEE T. Med. Imaging, 24. 352–60, 2005.

Petneházy, Ö., Czeibert, K., Donkó, T., Csóka, Á., Nagy, S.A., Lassó, A., Biksi, I., Zádori, P., Garamvölgyi, R., Bajzik, G., Vajda, Z., Falk, G., Repa, I.: **Application of the cross sectional diagnostic imaging methods (CT and MR) in anatomical 3D reconstructions. Part 2. Soft tissue and bone reconstruction. CT and MR fusion modeling of the equine stifle joint**, Magy. Állatorvosok, 140. 223–31, 2018a. (in Hungarian with English abstract)

Petneházy, Ö., Czeibert, K., Nagy, S.A., Donkó, T., Csóka, Á., Lassó, A., Nemes, C., Biksi, I., Garamvölgyi, R., Bajzik, G., Falk, G., Repa, I.: **Application of the cross sectional diagnostic imaging methods (CT and MR) in anatomical 3D reconstructions. Part 1.: CT based modelling of the air containing parts**, Magy. Állatorvosok, 140. 157–68, 2018b. (in Hungarian with English abstract)

Poo, M.-M., Du, J.-L., Ip, N.Y., Xiong, Z.-Q., Xu, B., Tan, T.: **China Brain Project: basic neuroscience, brain diseases, and brain-inspired computing**, Neuron, 92. 591–6, 2016.

Raffan, H., Guevar, J., Poyade, M., Rea, P.M.: **Canine neuroanatomy: development of a 3D reconstruction and interactive application for undergraduate veterinary education**, PLOS ONE, 12. e0168911, 2017.

Ratiu, P., Talos, I.-F.: **Cross–sectional atlas of the human brain**, 1st ed., Cambridge, Massachusetts: Harvard University Press, 2006.

Rauschning, W.: **Computed tomography and cryomicrotomy of lumbar spine specimens: A new technique for multiplanar anatomic correlation**, Spine, 8. 170–80, 1983.

Reveley, C., Gruslys, A., Ye, F.Q., Glen, D., Samaha, J., E. Russ, B., Saad, Z., K. Seth, A., Leopold, D.A., Saleem, K.S.: **Three-dimensional digital template atlas of the Macaque brain**, Cereb. Cortex, 27. 4463–77, 2017.

Riederer, B.M.: **Plastination and its importance in teaching anatomy. Critical points for long-term preservation of human tissue**, J. Anat., 224. 309–15, 2014.

Roe, A.W., editor.: **Imaging the brain with optical methods**, 1st ed., New York: Springer New York, 2010.

Rohlfing, T., Kroenke, C.D., Sullivan, E.V., Dubach, M.F., Bowden, D.M., Grant, K., Pfefferbaum, A.: **The INIA19 template and NeuroMaps atlas for primate brain image parcellation and spatial normalization**, Front. Neuroinform., 6. 2012.

Roy, D., Steyer, G.J., Gargesha, M., Stone, M.E., Wilson, D.L.: **3D cryo-imaging: a very high–resolution view of the whole mouse**, Anat. Rec., 292. 342–51, 2009.

Samadbeik, M., Yaaghobi, D., Bastani, P., Abhari, S., Rezaee, R., Garavand, A.: **The applications of virtual reality technology in medical groups teaching**, J. Adv. Med. Educ. Prof., 6. 123–9, 2018.

Sandhu, G.S., Solorio, L., Broome, A.-M., Salem, N., Kolthammer, J., Shah, T., Flask, C., Duerk, J.L.: **Whole animal imaging**, Wiley Interdiscip. Rev. Syst. Biol. Med., 2. 398–421, 2010.

Santi, P.A.: **Light sheet fluorescence microscopy**, J. Histochem. Cytochem., 59. 129–38, 2011.

Schmidt, M.J., Kramer, M.: **MRT-Atlas ZNS-Befunde bei Hund und Katze**, 1st ed., Stuttgart: Enke, 2015.

Schwarz, A.J., Danckaert, A., Reese, T., Gozzi, A., Paxinos, G., Watson, C., Merlo-Pich, E.V., Bifone, A.: **A stereotaxic MRI template set for the rat brain with tissue class distribution maps and co-registered anatomical atlas: Application to pharmacological MRI**, NeuroImage, 32. 538–50, 2006.

Seidlitz, J., Sponheim, C., Glen, D., Ye, F.Q., Saleem, K.S., Leopold, D.A., Ungerleider, L., Messinger, A.: **A population MRI brain template and analysis tools for the macaque**, NeuroImage, 170. 121–31, 2018.

Shen, E.H., Overly, C.C., Jones, A.R.: **The Allen Human Brain Atlas: Comprehensive gene expression mapping of the human brain**, Trends Neurosci., 35. 711–4, 2012.

Simonsen, K.P., Rasmussen, A.R., Mathisen, P., Petersen, H., Borup, F.: **A fast preparation of skeletal materials using enzyme maceration**, J. Forensic Sci., 56. 480–4, 2011.

Singer, M.: **The brain of the dog in section**, 1st ed., Philadelphia: Saunders, 1962.

Singh, B., editor.: **Dyce, Sack, and Wensing's textbook of veterinary anatomy**, 5th ed., St. Louis, Missouri: Elsevier, 2018.

Sora, M.C., von Horst, C., López-Albors, O., Latorre, R.: **Ultra-thin sectioning and grinding of epoxy plastinated tissue**, Anat. Histol. Embryol., 2019.

Spitzer, V., Ackerman, M.J., Scherzinger, A.L., Whitlock, D.: **The visible human male: a technical report**, J. Am. Med. Inform. Assoc., 3. 118–30, 1996.

Su, M., Head, E., Brooks, W.M., Wang, Z., Muggenburg, B.A., Adam, G.E., Sutherland, R., Cotman, C.W., Nalcioglu, O.: **Magnetic resonance imaging of anatomic and vascular characteristics in a canine model of human aging**, Neurobiol. Aging, 19. 479–85, 1998.

Szabó, D., Czeibert, K., Kettinger, Á., Gácsi, M., Andics, A., Miklósi, Á., Kubinyi, E.: **Resting-state fMRI data of awake dogs (*Canis familiaris*) via group-level independent component analysis reveal multiple, spatially distributed resting-state networks**, Sci. Rep., 9. 1–25, 2019.

Szabó, D., Gábor, A., Gácsi, M., Faragó, T., Kubinyi, E., Miklósi, Á., Andics, A.: **On the face of it: no differential sensitivity to internal facial features in the dog brain**, Front. Behav. Neurosci. 14. 2020.

Tang, L., Chung, M.S., Liu, Q., Shin, D.S.: **Advanced features of whole body sectioned images: Virtual Chinese Human**, Clin. Anat., 23. 523–9, 2010.

Tapp, P.D., Head, K., Head, E., Milgram, N.W., Muggenburg, B.A., Su, M.Y.: **Application of an automated voxel-based morphometry technique to assess regional gray and white matter brain atrophy in a canine model of aging**, Neuroimage, 29. 234–44, 2006.

Thompkins, A.M., Deshpande, G., Waggoner, P., Katz, J.S.: **Functional magnetic resonance imaging of the domestic dog: research, methodology, and conceptual issues**, Comp. Cogn. Behav. Rev., 11. 63–82, 2016.

Thomson, C.E., Hahn, C.: **Veterinary neuroanatomy: a clinical approach**, 1st ed., Edinburgh; Philadelphia: Saunders W.B., 2012.

Thrall, D.E.: **Textbook of veterinary diagnostic radiology**, 6th ed., St. Louis, Missouri: Saunders, 2012.

Toga, A.W., Santori, E.M., Hazani, R., Ambach, K.: **A 3D digital map of rat brain**, Brain Res. Bull., 38. 77–85, 1995.

Tóth, L., Gácsi, M., Miklósi, Á., Bogner, P., Repa, I.: **Awake dog brain magnetic resonance imaging**, J. Vet. Behav., 4. 50, 2009.

Uemura, E.E.: **Fundamentals of canine neuroanatomy and neurophysiology**, 1st ed., Ames, Iowa: Wiley-Blackwell, 2015.

Ulmer, S., Jansen, O., editors.: **fMRI: basics and clinical applications**, 2nd ed., New York: Springer, 2013.

Verli, F.D., Rossi-Schneider, T.R., Schneider, F.L., Yurgel, L.S., de Souza, M.A.L.: **Vascular corrosion casting technique steps**, Scanning, 29. 128–32, 2007.

Vibulchan, P., Cheunsuang, O.: **Comparison of Mulligan's, Alston's and Prussian blue reaction's methods for staining dog brain slices prior to plastination**, Thai J. Vet. Med., 44. 547–51, 2014.

Weiglein, A.H.: **Plastination in the neurosciences. Keynote lecture**, Acta Anat., 158. 6–9, 1997.

Wisner, E., Zwingenberger, A.: **Atlas of small animal CT and MRI**, 1st ed., Ames, Iowa: John Wiley & Sons, 2015.

Zhang, S.-X., Heng, P.-A., Liu, Z.-J., Tan, L.-W., Qiu, M.-G., Li, Q.-Y. et al.: **Creation of the Chinese Visible Human data set**, Anat. Rec. Part B, 275. 190–5, 2003.

9. Scientific publications

9.1. Publications in peer-reviewed journals related to the thesis

- Czeibert, K., Baksa, G., Grimm, A., Nagy, Sz. A., Kubinyi, E., Petneházy, Ö.: **MRI, CT and high resolution macro-anatomical images with cryosectioning of a Beagle brain: Creating the base of a multimodal imaging atlas**, PLOS ONE, 14. e0213458, 2019.

- Czeibert, K., Andics, A., Petneházy, Ö., Kubinyi, E.: **A detailed canine brain label map for neuroimaging analysis**, Biol. Fut., 70. 112–20, 2019.

- Czeibert, K., Baksa, G., Kozma, I., Pomsár, M., Rácz, B., Petneházy, Ö.: **Comparative 3-dimensional visualization of the equine petrosal bone**, Magy. Állatorvosok, 140. 737–44, 2018. (in Hungarian with English abstract)

- Szabó, D., Czeibert, K., Kettinger, Á., Gácsi, M., Andics, A., Miklósi, Á., Kubinyi, E.: **Resting-state fMRI data of awake dogs (*Canis familiaris*) via group-level independent component analysis reveal multiple, spatially distributed resting-state networks**, Sci. Rep., 9. 1–25, 2019.

- Petneházy, Ö., Czeibert, K., Nagy, Sz. A., Donkó, T., Csóka, Á., Lassó, A., Nemes, Cs., Biksi, I., Garamvölgyi, R., Bajzik, G., Falk, Gy., Repa, I.: **Application of the cross sectional diagnostic imaging methods (CT and MR) in anatomical 3D reconstructions. Part 1.: CT based modeling of the air containing parts**, Magy. Állatorvosok, 140. 157–68, 2018. (in Hungarian with English abstract)

- Petneházy, Ö., Czeibert, K., Donkó, T., Csóka, Á., Nagy, Sz. A., Lassó, A., Biksi, I., Zádori, P., Garamvölgyi, R., Bajzik, G., Vajda, Zs., Falk, Gy., Repa I.: **Application of the cross sectional diagnostic imaging methods (CT and MR) in anatomical 3D reconstructions. Part 2. Soft tissue and bone reconstruction. CT and MR fusion modeling of the equine stifle joint**, Magy. Állatorvosok, 140. 223–31, 2018. (in Hungarian with English abstract)

- Lehner, L., Czeibert, K., Koltai, Zs., Jakab, Cs.: **Removal of frontal meningioma by bilateral transfrontal approach in dog. Case study**, Magy. Állatorvosok, 141. 533–45, 2019. (in Hungarian with English abstract)

- Lehner, L., Czeibert, K., Csöndes, J., Balogh, N., Kerekes, Z., Jakab, Cs.: **Endoscope-guided transsphenoidal removal of a hypophyseal tumour in a dog. Case study**, Magy. Állatorvosok, 140. 535–50, 2018. (in Hungarian with English abstract)

- Lehner, L., Jakab, Cs., Czeibert, K.: **Surgical management of central Cushing-disease: successful endoscope-assisted removal of a hypophyseal microadenoma in a Boxer. Case study**, Magy. Állatorvosok, 141. 289–300, 2019. (in Hungarian with English abstract)

- Lehner, L., Nagy, G., Jakab, Cs., Czeibert, K.: **Ventriculoscopy in a dog: fenestration of a parieto-occipital cyst into the lateral ventricle with an endoscope**, Magy. Állatorvosok, 141. 145–56, 2019. (in Hungarian with English abstract)

- Lehner, L., Garamvölgyi, R., Jakab, Cs., Kerekes, Z., Czeibert, K.: **A recurrent suprapituitary ependymal cyst managed by endoscopy-assisted transsphenoidal surgery in a canine: a case report**, Front. Vet. Sci., 6. 2019.

- Bálint, A., Andics, A., Gácsi, M., Gábor, A., Czeibert, K., Luce, C.M., Miklósi, Á., Kröger, R.H.H.: **Dogs can sense weak thermal radiation**, Sci. Rep., 10. 1–9, 2020.

9.2. Publications in peer-reviewed journals not related to the thesis

- Czeibert, K., Pápa, K., Jakab, Cs., Kiss, G., Balogh, L., Balka, Gy.: **Epileptic fits in a Labrador retriever caused by ependymoma and acquired liver deficiency. Case report**, Magy. Állatorvosok, 137. 103–13, 2015. (in Hungarian with English abstract)

- Czeibert, K., Pintér, Á., Ivády, A., Samu, K.: **Relationship between meteorological factors and epileptic fits in a Jack Russell terrier. Case study**, Magy. Állatorvosok, 136. 461–71, 2014. (in Hungarian with English abstract)

- Czeibert, K., Pintér, Á., Ivády, A., Samu, K.: **Effect of the meteorological factors on the fits of an epileptic dog. Case study**, Magy. Állatorvosok, 136. 149–56, 2014. (in Hungarian with English abstract)

9.3. Books, book chapters

- Authorship: Czeibert, K., Baksa, G., Grimm, A., Nagy, Sz. A., Horák, D., Petneházy, Ö.: **FlipCat: Cat's head seen on MRI and cryosections**, Budapest: Műszaki Könyvkiadó Kft., 2015.

- Co-authorship (figure contributor): in Singh, B. (editor): **Dyce, Sack, and Wensing's textbook of veterinary anatomy**, 5th edition. St. Louis, Missouri: Elsevier, 2018.

- Co-authorship (figure contributor): **Main anatomical features regarding the orbital region (Appendix No. II)** in: Fenyves, I., Szentpétery, Zs.: **Questions and answers in small animal ophthalmology**, Budapest: MÁOK Kft., 2018.

- Co-authorship (figure contributor) in: Petneházy, Ö., Garamvölgyi, R., Horn, P. (editors): **Cross-sectional, CT and MR anatomy atlas of the domestic turkey**, Kaposvár: University of Kaposvár, 2015.

9.4. Conference presentations

9.4.1 Conference presentations related to the thesis

- Czeibert, K., Baksa, G., Grimm, A., Nagy, Sz. A., Kubinyi, E., Petneházy, Ö.: **A Beagle brain's multimodal imaging with MRI, CT, cryosectioning and 3-dimensional modeling**. *32nd Annual Symposium of the European Society of Veterinary Neurology (ESVN) and the European College of Veterinary Neurology (ECVN).* Wroclaw, 13-14 September 2019.

- Czeibert, K., Baksa, G., Grimm, A., Nagy, Sz. A., Kubinyi, E., Petneházy, Ö.: **Comparative imaging anatomy of the canine brain with MRI, CT, cryosectioning and 3D-modeling**. *65th Meeting of the American Association of Veterinary Anatomists (AAVA).* Anatomia, Histologia, Embryologia 48:(Suppl.1). Banff, 26-29 July 2019.

- Czeibert, K., Petneházy, Ö., Csörgő, T., Kubinyi, E.: **Comparing brains from different dog breeds based on 3D-endocast modeling**. *12th International Congress of Vertebrate Morphology (ICVM).* Journal of Morphology 280:(Suppl.1). Prague, 21-25 July 2019.

- Czeibert, K., Baksa, G., Lehner, L., Petneházy, Ö.: **Anatomical visualisation possibilities and surgical approach of the middle cranial fossa in dogs (*Canis familiaris*)**. *32th Conference of the European Association of Veterinary Anatomists (EAVA).* Anatomia, Histologia, Embryologia 47:(Suppl.1). Hannover, 25-28 July 2018.

- Czeibert, K., Piotti, P., Kubinyi, E., Petneházy, Ö.: **Review of the terminology of dogs' (*Canis familiaris*) main cortical structures**. *32th Conference of the European Association of Veterinary Anatomists (EAVA).* Anatomia, Histologia, Embryologia 47:(Suppl.1). Hannover, 25-28 July 2018.

- Czeibert, K., Sándor, S., Egerer, A., Kubinyi, E.: **A Canine Brain and Tissue Bank**. *6th Canine Science Forum (CSF).* Budapest, 3-6 July 2018.

- Czeibert, K., Gunde, E., Piotti, P., Kubinyi, E.: **Longitudinal assessment of ventriculomegaly in dogs trained for fMRI studies**. *6th Canine Science Forum (CSF).* Budapest, 3-6 July 2018.

- Czeibert, K., Baksa, G., Grimm, A., Kozma, I., Fekete, I., Falk, Gy., Nyíri, G., Sótonyi, P., Rácz, B., Petneházy, Ö.: **Understanding equine petrosal bone: 3D-reconstruction and virtual endoscopy of the middle and inner ear**. *31th Conference of the European Association of Veterinary Anatomists (EAVA).* Anatomia, Histologia, Embryologia 45:(Suppl.1). Vienna, 27-31 July 2016.

- Czeibert, K., Baksa, G., Grimm, A., Szabó, P., Nagy, Sz. A., Bogner, P., Balogh, L., Sótonyi, P., Rácz, B., Petneházy, Ö.: **Assessment of the canine eye's blood supply using conventional preparation technique, corrosion casting, cryomacrotomisation and 3D-modeling**. *31th Conference of the European Association of Veterinary Anatomists (EAVA).* Anatomia, Histologia, Embryologia 45:(Suppl.1). Vienna, 27-31 July 2016.

- Czeibert, K., Baksa, G., Grimm, A., Rácz, B., Petneházy, Ö.: **Advances of the cryosectioning technique in developing the field of human and veterinary medical cross-section anatomy**. *Joint Conference of the Hungarian Pharmacology, Anatomy, Microcirculation and Physiological Societies (FAME).* Pécs, 1-4 June 2016. (in Hungarian)

- Czeibert, K., Baksa, G., Szabó, P., Grimm, A., Nagy, Sz. A., Bogner, P., Sótonyi, P., Rácz, B., Petneházy, Ö.: **Cryomacrotomisation as an anatomical imaging technique: comparing human and veterinary medical studies**. *Academic Report organized by the Veterinary Science Committee of the Hungarian Academy of Science and the Doctoral School of the Faculty of Veterinary Sciences, Szent István University*. Budapest, 25-28 January 2016. (in Hungarian)

- Czeibert, K., Baksa, G., Kozma, I., Grimm, A., Fekete, I., Handschuh, S., Falk, Gy., Petneházy, Ö.: **Experiences in 3D-modeling and printing of a French bulldog skull's composite anatomical structures**. *19th Conference of the Hungarian Anatomical Society.* Szeged, 11-13 June 2015. (in Hungarian)

- Czeibert, K., Baksa, G., Szabó, P., Grimm, A., Patonay, L., Nagy, Sz. A., Bogner, P., Handschuh, S., Rácz, B., Petneházy, Ö.: **From cryosectioning to 3D-modeling: complex visualization of a feline head with milling, diagnostic imaging (CT, MRI) and volume rendering methods**. *19th Conference of the Hungarian Anatomical Society.* Szeged, 11-13 June 2015. (in Hungarian)

- Czeibert, K., Baksa, G., Szabó, P., Grimm, A., Patonay, L., Nagy, Sz. A., Bogner, P., Handschuh, S., Sótonyi, P., Rácz, B., Petneházy, Ö.: **Prospects in the combined application of the diagnostic imaging methods (CT, MRI), cryosectioning and 3-dimensional modeling**. *Academic Report organized by the Veterinary Science Committee of the Hungarian Academy of Science and the Doctoral School of the Faculty of Veterinary Sciences*. Budapest, 26-29 January 2015. (in Hungarian)

- Czeibert, K., Baksa, G., Szabó, P., Sótonyi, P., Rácz, B., Petneházy, Ö.: **Blood supply of the canine brain: a multiway approach with conventional technique, corrosion casting and cryosectioning**. *30th Conference of the European Association of Veterinary Anatomists (EAVA).* Anatomia, Histologia, Embryologia 43:(Suppl.1). Cluj-Napoca, 23-26 July 2014.

- Czeibert, K., Petneházy, Ö., Rácz, B., Sótonyi, P.: **Imaging with cryosectioning: basics of the cryomacrotomisation technique**. *Academic Report organized by the Veterinary Science Committee of the Hungarian Academy of Science and the Doctoral School of the Faculty of Veterinary Sciences, Szent István University*. Budapest, 27-30 January 2014. (in Hungarian)

- Petneházy, Ö., Donkó, T., Czeibert, K., Lassó, A., Csóka, Á., Petrási, Zs., Körösi, D., Garamvölgyi, R.: **Anatomical, CT and MRI cross-sectional atlas of the Pannon Minipig**. *65th Meeting of the American Association of Veterinary Anatomists (AAVA).* Anatomia, Histologia, Embryologia 48:(Suppl.1). Banff, 26-29 July 2019.

- Petneházy, Ö., Vinczen, E., Repa, K., Seregi, R., Donkó, T., Csóka, Á., Fajtai, D., Czeibert, K., Lassó, A.: **3D-reconstruction of the equine carpal and tarsal joints based on CT and MR image fusion**. *65th Meeting of the American Association of Veterinary Anatomists (AAVA).* Anatomia, Histologia, Embryologia 48:(Suppl.1). Banff, 26-29 July 2019.

- Lehner, L., Kerekes, Z., Garamvölgyi, R., Jakab, Cs., Czeibert, K.: **Pre- and postoperative MRI characteristics and case reports of three pituitary-related disorders in dogs**. *15th European Veterinary MR User Meeting (MR imaging of the head).* Vienna, 3-4 May 2019.

- Gunde, E., Czeibert, K., Piotti, P., Arany-Tóth, A., Kubinyi, E.: **Ventriculomegaly in dogs trained for fMRI studies: findings and future objectives**. *31th Annual Symposium of the European Society of Veterinary Neurology (ESVN) and European College of Veterinary Neurology (ECVN).* Copenhagen, 20-22 September 2018.

- Baksa, G., Czeibert, K., Gyebnár, J., Petneházy, Ö., Bálint, P.: **Arterial blood supply of the metacarpophalangeal joints with regard of diagnostic ultrasonographic approach in special rheumatological cases**. *21th Conference of the Hungarian Anatomical Society.* Debrecen, 15-16 June 2018. (in Hungarian)

- Petneházy, Ö., Czeibert, K., Donkó, T., Csóka, Á., Petrási, Zs., Lassó, A., Garamvölgyi, R.: **Cardiac CT examinations and reconstructions in different domestic animals and genotypes**. *32th Conference of the European Association of Veterinary Anatomists (EAVA).* Anatomia, Histologia, Embryologia 47:(Suppl.1). Hannover, 25-28 July 2018.

- Petneházy, Ö., Czeibert, K., Donkó, T., Csóka, Á., Lassó, A., Kozma, I.: **CT based 3D reconstruction and analysis of the paranasal sinuses in horses, dogs and pigs**. *32th Conference of the European Association of Veterinary Anatomists (EAVA).* Anatomia, Histologia, Embryologia 47:(Suppl.1). Hannover, 25-28 July 2018.

- Kubinyi, E., Szabó, D., Wallis, L., Iotchev, I., Sándor, S., Czeibert, K., Egerer, A., Bognár, Zs., Tátrai, K., Turcsán, B., Piotti, P..: **Senior Family Dog Project: studying cognitive ageing in dogs using an interdisciplinary approach**. *6th Canine Science Forum (CSF).* Budapest, 3-6 July 2018.

- Szabó, D., Czeibert, K., Kettinger, Á., Gácsi, M., Andics, A., Miklósi, Á., Kubinyi, E.: **Human-analogue resting-state networks in the dog brain**. *6th Canine Science Forum (CSF).* Budapest, 3-6 July 2018.

- Petneházy, Ö., Tokaji, R., Czeibert, K.: **Blood supply of the male genital tract in dogs based on conventional preparation, corrosion casting and 3D modeling**. *31th Conference of the European Association of Veterinary Anatomists (EAVA).* Anatomia, Histologia, Embryologia 45:(Suppl.1). Vienna, 27-31 July 2016.

- Petneházy, Ö., Czeibert, K., Baksa, G., Bajzik, G., Garamvölgyi, R., Repa, I.: **3D reconstruction of the structures of the equine stifle joint based on CT and MR images**. *31th Conference of the European Association of Veterinary Anatomists (EAVA).* Anatomia, Histologia, Embryologia 45:(Suppl.1). Vienna, 27-31 July 2016.

- Petneházy, Ö., Donkó, T., Garamvölgyi, R., Takács, I., Czeibert, K., Repa, I.: **From cross section to 3D anatomy: problems and solutions**. *4th Annual Conference on Body and Carcass Evaluation, Meat Quality, Software and Traceability (FAIM).* Edinburgh, 22-23 September 2015.

- Baksa, G., Czeibert, K., Grimm, A., Szabó, P., Gyebnár, J., Handschuh, S., Petneházy, Ö., Bálint, P.: **Investigation of the small arterial vessels of the metacarpophalangeal joints using cryomacrotomisation**. *19th Conference of the Hungarian Anatomical Society.* Szeged, 11-13 June 2015. (in Hungarian)

- Grimm, A., Baksa, G., Czeibert, K., Szabó, P., Handschuh, S., Petneházy, Ö., Tamás, L.: **Clinical anatomy of Eustachian tube from the aspect of ventilation disorders**. *19th Conference of the Hungarian Anatomical Society.* Szeged, 11-13 June 2015. (in Hungarian)

- Petneházy, Ö., Bajzik, G., Zádori, P., Vajda, Zs., Garamvölgyi, R., Czeibert, K., Repa, I.: **3D-modeling of a horse stifle joint based on fusioned CT and MR images**. *19th Conference of the Hungarian Anatomical Society.* Szeged, 11-13 June 2015. (in Hungarian)

- Petneházy, Ö., Czeibert, K., Baksa, G., Patonay, L.: **Practical aspects of the corrosion casting technique**. *30th Conference of the European Association of Veterinary Anatomists (EAVA).* Anatomia, Histologia, Embryologia 43:(Suppl.1). Cluj-Napoca, 23-26 July 2014.

9.4.2 Conference presentations not related to the thesis

- Czeibert, K., Abonyi-Tóth, Zs., Fülöp, A.: **Seizure provoking role of the environmental effects in epileptic animals**. *3rd Conference of Medical Meteorology.* Budapest, 28-29 May 2015. (in Hungarian)

- Czeibert, K., Pintér, Á., Ivády, A., Pintér, F., Samu, K..: **Studying the meteorological effects in animals**. *3rd Conference of Medical Meteorology.* Budapest, 28-29 May 2015. (in Hungarian)

- Samu, K., Pintér, Á., Czeibert, K.: **Technological considerations during developing an equipment which is capable for measuring weather-sensitivity of animals with epilepsy**. *23th International Mechanical Engineering Meeting (OGÉT).* Csíksomlyó, 23-26 April 2015. (in Hungarian)

Acknowledgements

I would like to thank many people who supported me during these years:

- First and foremost, to my supervisor, colleague and friend, **dr. Örs Petneházy**, without whom this project could not be done. Our common interest and our shared intent in anatomical visualisation enabled us to achieve these results, made it possible to design and refine the cryosectioning technique, and then to accomplish this work.

- To my other supervisor, **dr. Bence Rácz**, and to the head of the Department of Anatomy and Histology at University of Veterinary Medicine, **dr. Péter Sótonyi**, for accepting my chosen idea for the topic of this PhD project.

- Special thanks to the members of the anatomy lab at Semmelweis University, who had a key role in the success of the cryosectioning studies: to **dr. Gábor Baksa**, **dr. András Grimm** and **dr. Lajos Patonay** for their extensive help during the studies, for the productive and good atmosphere, for the brainstorming sessions and for providing the space and equipment for the required preparations.

- To **Péter Szabó**, who helped with the photography throughout the entire project, regardless of where we had to go in the country or how long we had to work during a cryosectioning procedure, and who ensured with his equipment and expertise that the recorded images would have the best available quality.

- To those whose work supported the image recording and processing: to **dr. Szilvia Anett Nagy**, **dr. Péter Bogner**, **dr. Judit Benczik**, **dr. Lajos Balogh**, **István Kozma** and **Imre Fekete** for their help during the CT and MRI scanning procedures; to **Miklós Pomsár** for helping in the petrosal bone video animations; to Dániel Horák in making the flip-book; to **dr. Stephan Handschuh** and **Kathy Tinoco** for their aid in studying Amira; to **dr. Gábor Nyíri** for the opportunity to work in his research unit at the Institute of Experimental Medicine, Hungarian Academy of Sciences; and to the staff of the machine shops for their help and allowing us to conduct our cryosectioning studies by using their equipment and craftsmanship.

- I would like to specially thank **György Falk**, the director of Varinex Ltd, for his continuous and always kind support and useful advices regarding 3D printing, for printing the different models I created during the project, and for the possibilities he has given this field; thanks also to all the members of the company for their help.

- I show gratitude to **dr. László Lehner** and **dr. Gábor Nagy**, and to the members of the Felicavet veterinary clinic and hospital. Working with them, I had the opportunity to apply my knowledge gained from my clinical experience, from teaching veterinary anatomy and from this research project, to actively participate in neurosurgeries which aimed to help animals with different central nervous system disorders.

- My honest thanks to **dr. Enikő Kubinyi**, the leader of the ERC group at the Department of Ethology, Institute of Biology, Eötvös Loránd University, to the members of the ERC team and to the people of the Department of Ethology for providing a quality and friendly research environment where I could learn how scientific research works, where I could test my expertise and gain further insights into canine neuroanatomy, image visualisation and fMRI analysis under the framework of projects such as coordinating the Canine Brain and Tissue Bank.

- To **Zsolt Mihályfi** and **Olivér Vasvári,** and the members of the 360World company who imported the cryosectioned datasets into the Hololens system and with it provide a promising future for using mixed reality in the education, research and medical fields.

- Last, but not least, I owe thanks to my family and to all with whom I had contact throughout these years for their fruitful conversations, their friendship, and for all those moments both at home and abroad when I experienced peace and harmony.